Mixed Mode Cracking in Layered Materials

J. W. HUTCHINSON

Division of Applied Sciences
Harvard University
Cambridge, Massachusetts

and

Z. SUO

Mechanical Engineering Department
University of California
Santa Barbara, California

I. Introduction

The aim of this chapter is to pull together recent work on the fracture of layered materials. Many modern materials and material systems are layered. Interfaces are intrinsic to these materials, as are heterogeneities such as residual stresses and discontinuities in thermal and elastic properties. The structural performance of such materials and systems generally depends on just these features. The potential applications of fracture mechanics of layered materials ranges over a broad spectrum of problem areas. Included are: protective coatings, multilayer capacitors, thin film/substrate systems for electronic packages, layered structural composites of many varieties, reaction product layers, and adhesive joints.

Attention is confined in this chapter to elastic fracture phenomena in which the extent of the inelastic processes is small compared with the relevant geometric length scales, such as layer thickness. For the most part, the separate sections are designed so that they can be read independently. The main exceptions are Section II, which presents the theory of mixed mode interfacial fracture underlying many of the applications, and Section III, which catalogues a number of basic elasticity solutions for layered systems referred to throughout this chapter. Then follow sections on test specimens for determining interfacial toughness, fracture modes in thin films under either tension or compression, blister tests, and, lastly, failure modes of adhesive joints. We believe that most of the important fracture concepts for layered systems emerge in the analysis of these examples. One concept, in particular, that plays a central role is the idea of steady-state cracking. In almost every application considered here, a steady-state analysis provides a simplified solution that is directly relevant to design against fracture.

This chapter builds on earlier work by many researchers, but specifically the contributions to the elasticity theory of cracks in layered materials of Erdogan and coworkers in the 1970s, which comprised most of the available solutions until recently. Special mention must also be made of the article on thin films and coatings by Gille (1985), which gives a comprehensive treatment of fracture modes without the insights from the recent developments in interfacial fracture. It is especially these recent developments that have transformed the subject. We have been fortunate to have been involved with one of the groups (that centered at the University of California, Santa Barbara) that have been concerned with the extension of both experimental and theoretical aspects of fracture mechanics to interfaces. This involvement is reflected in our approach as well as the topics that have been chosen for presentation.

Structural reliability of multilayers is a fast growing field. An article written at this point is most likely transitory work, although we have tried to put various aspects into perspective, and we believe some of them are of permanent nature. Like most review articles of this kind, subject matter with various degrees of novelty that has not been published previously is incorporated. Some fill gaps, others are ready extensions, and still others are simply speculations. The writers sincerely urge the practitioners in the related disciplines to use the article critically, so that the results can be validated, expanded, or modified. A more consolidated version of the article could then emerge on a later occasion.

II. Mixed Mode Fracture: Crack Tip Fields and Propagation Criteria

There is ample experimental evidence that cracks in brittle, isotropic, homogeneous materials propagate such that pure mode I conditions are maintained at the crack tip. This appears to be true for fatigue crack growth and stress corrosion cracking as well as crack advance under monotonic loading. An unloaded crack subsequently subject to a combination of modes I and II will initiate growth by kinking in a direction such that the advancing tip is in mode I. A crack in a material with strongly orthotropic fracture properties, or a crack in an interface with a fracture toughness that is distinct from the materials joined across it, can experience either kinking or straight-ahead propagation under mixed mode loading depending on a number of factors, including the relative toughnesses associated with the competing directions of advance. This section gives results from studies of

crack tip fields for specifying criteria for straight-ahead propagation or kinking under mixed mode loading. An assessment of the competition between different directions of advance can also be made. Homogeneous materials are considered first, starting with the isotropic case and going on to orthotropic symmetry. Cracks on interfaces between dissimilar isotropic elastic solids are dealt with last.

A. ISOTROPIC ELASTIC SOLIDS

The stress fields at the tip of a crack in plane stress or plane strain for a homogeneous, isotropic elastic solid have the well-known general form

$$\sigma_{ij} = K_I(2\pi r)^{-1/2}\sigma_{ij}^I(\theta) + K_{II}(2\pi r)^{-1/2}\sigma_{ij}^{II}(\theta) + T\delta_{i1}\delta_{j1}, \qquad (2.1)$$

where δ_{ij} is the Kronecker delta and r and θ are polar coordinates centered at the tip as shown in Fig. 1. The θ-variations are given in many texts on fracture. They are the same for plane stress and plane strain, except σ_{33}, which vanishes in plane stress and is given by $v(\sigma_{11} + \sigma_{22})$ in plane strain, where v is Poisson's ratio. Mode I fields are symmetric with respect to the crack line with $\sigma_{22}^I = 1$ and $\sigma_{12}^I = 0$ on $\theta = 0$, while the mode II fields are antisymmetric with $\sigma_{12}^{II} = 1$ and $\sigma_{22}^{II} = 0$ on $\theta = 0$. The higher order contributions not included in (2.1) all vanish as $r \to 0$. The T-stress, $\sigma_{11} = T$, arises in discussions of crack stability and kinking. Thus, the singular tractions on the line ahead of the crack tip ($\theta = 0$) have the mode I and II stress intensity factors as amplitudes according to

$$\sigma_{22} = K_I(2\pi r)^{-1/2}, \qquad \sigma_{12} = K_{II}(2\pi r)^{-1/2}. \qquad (2.2)$$

The relative displacements of the crack faces behind the tip,

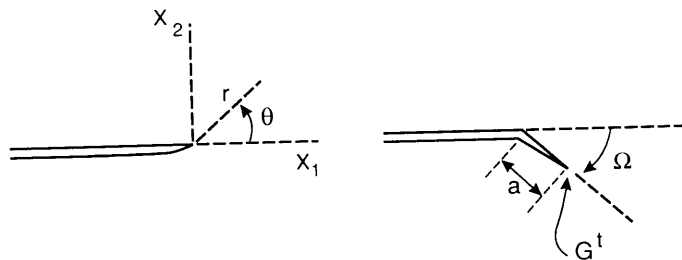$$\delta_i = u_i(r, \theta = \pi) - u_i(r, \theta = -\pi),$$

FIG. 1. Conventions at a crack tip and the geometry of a kinked crack.

in the region dominated by the singular fields are given by

$$(\delta_2, \delta_1) = (K_I, K_{II})(8/\bar{E})[r/(2\pi)]^{1/2}, \qquad (2.3)$$

where

$$\bar{E} = E/(1 - v^2) \qquad \text{(plane strain)}$$

$$= E \qquad \text{(plane stress)} \qquad (2.4)$$

and E is Young's modulus. Irwin's relation between the energy release rate G for straight-ahead quasi-static crack advance and the stress intensity factors is

$$G = (K_I^2 + K_{II}^2)/\bar{E}. \qquad (2.5)$$

Next, consider a putative crack segment of length a kinking out the plane of the crack at an angle Ω with the sense shown in Fig. 1. When a is sufficiently small compared with all in-plane geometric lengths, including the crack length itself, there exists a relation between the stress intensity factors K_I^t and K_{II}^t at the tip of the putative crack and the stress intensity factors K_I and K_{II} and the T-stress acting on the parent crack tip when $a = 0$. The relation has the form

$$K_I^t = c_{11}K_I + c_{12}K_{II} + b_1 Ta^{1/2},$$
$$K_{II}^t = c_{21}K_I + c_{22}K_{II} + b_2 Ta^{1/2}. \qquad (2.6)$$

The Ω-dependences of the c's are given by Hayashi and Nemat-Nasser (1981) and by He and Hutchinson (1989b), while the Ω-dependence of the b's is given by He *et al.* (1991).

The ratio of the energy release rate of the parent crack when it advances straight-ahead to that of the kinked crack, $G^t = (K_I^{t2} + K_{II}^{t2})/\bar{E}$, is of the form

$$G/G^t = F(\Omega, \psi, \eta), \qquad (2.7)$$

where F depends on the coefficients in (2.6). In addition, ψ is the measure of mode II to mode I loading acting on the parent crack defined by

$$\psi = \tan^{-1}(K_{II}/K_I) \qquad (2.8)$$

and

$$\eta = T[a/(\bar{E}G)]^{1/2}. \qquad (2.9)$$

The ratio (2.7) applies to both plane strain and planes stress.

With G_{max}^t denoting the value of G^t maximized with respect to Ω for a given ψ, the ratio G/G_{max}^t is plotted as a function of ψ for various values of η in Fig. 2, which was taken from He *et al.* (1991). The kinking angle $\hat{\Omega}$ at
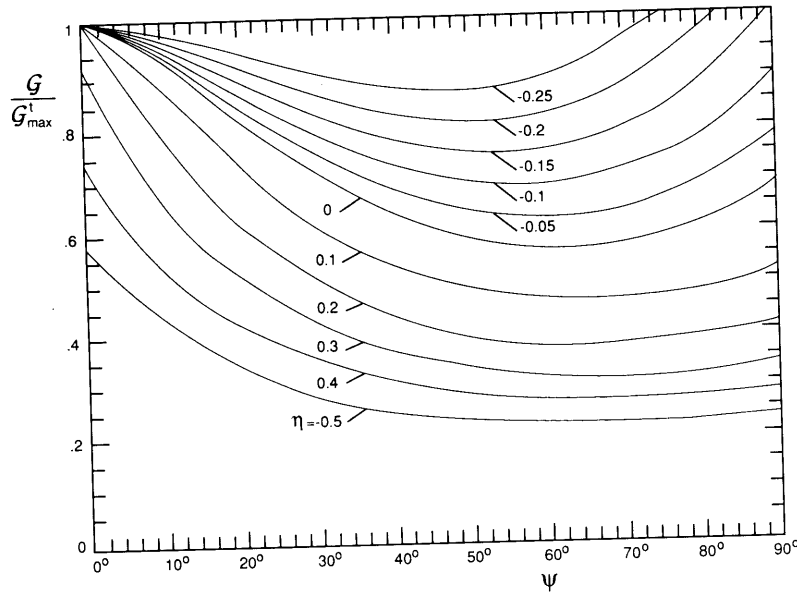
FIG. 2. Ratio of energy release rate for straight-ahead advance to maximum energy release rate for a kinked crack as a function of $\psi = \tan^{-1}(K_{II}/K_I)$. Reproduced from He *et al.* (1991).

which G^t is maximized is plotted as a function of ψ in Fig. 3 for the limit $\eta = 0$. The ratio in Fig. 2 corresponds to $\hat{F}(\psi, \eta) \equiv F(\hat{\Omega}, \psi, \eta)$. The kinking angle that maximizes G^t is nearly coincident with the kinking angle for which $K_{II}^t = 0$, as can be seen in Fig. 3. Only for ψ greater than about 50° is the difference more than one degree, and the difference between the energy release rates for the two directions is numerically insignificant. Thus,
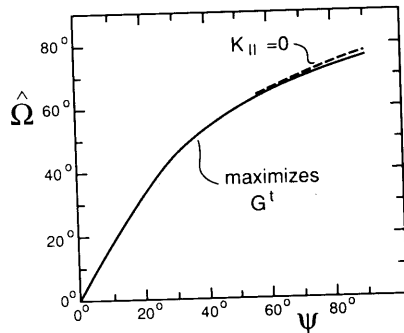

FIG. 3. Kink angle as predicted by two criteria.

for all practical purposes, there is no distinction between a criterion for kinking based on maximizing G^t or one based on propagation in the direction in which $K_{II} = 0$. With $\Gamma = K_{Ic}^2/\bar{E}$ denoting the mode I toughness, kinking will initiate at a crack tip in a brittle material subject to monotonic mixed mode loading when

$$G = \hat{F}(\psi, \eta = 0)\Gamma, \qquad (2.10)$$

where $\hat{F}$ is the ratio in Fig. 2. Once initiated, the advancing tip will be influenced by the T-stress through the η-dependence of $\hat{F}$.

B. HOMOGENEOUS, ORTHOTROPIC ELASTIC SOLIDS

Consideration will be restricted to plane cracks aligned with the principal axes of orthotropy and crack advance that is either straight-ahead or kinked at 90° parallel to the second in-plane orthotropy axis. With reference to Fig. 1, let the orthotropy axes coincide with the x_i-axes and take the plane of the crack to be $x_2 = 0$ with its edge along the x_3-axis. Introduce elastic compliances of the solid in a standard way according to

$$\varepsilon_i = \sum_{j=1}^{6} s_{ij}\sigma_j, \qquad i = 1 \text{ to } 6, \qquad (2.11)$$

where

$$\{\varepsilon_i\} = \{\varepsilon_{11}, \varepsilon_{22}, \varepsilon_{33}, 2\varepsilon_{23}, 2\varepsilon_{13}, 2\varepsilon_{12}\},$$

$$\{\sigma_i\} = \{\sigma_{11}, \sigma_{22}, \sigma_{33}, \sigma_{23}, \sigma_{13}, \sigma_{12}\}.$$

For the orthotropy assumed here, deformations in the (1, 2) plane satisfy (Lekhnitskii, 1981)

$$\varepsilon_i = \sum_{i=1,2,6} b_{ij}\sigma_j, \qquad i = 1, 2, 6, \qquad (2.12)$$

where, for $i, j = 1, 2, 6$,

$$b_{ij} = \begin{cases} s_{ij}, & \text{(plane stress)} \\ s_{ij} - s_{i3}s_{j3}/s_{33}, & \text{(plane strain)} \end{cases} \qquad (2.13)$$

with only four independent elastic constants: b_{11}, $b_{12} = b_{21}$, b_{22}, and b_{66} ($b_{16} = b_{26} = 0$).

For simply connected domains with traction boundary conditions, Suo (1990c) has shown that the stresses depend on only the following two

(rather than three) nondimensional elastic parameters:

$$\lambda = b_{11}/b_{22}, \qquad \rho = (b_{12} + \tfrac{1}{2}b_{66})/(b_{11}b_{22})^{1/2}. \qquad (2.14)$$

This particular choice of parameters is particularly useful for reasons that will emerge shortly. When $\lambda = \rho = 1$, the in-plane behavior is isotropic (i.e., the material is transversely isotropic with respect to the x_3-axis), and when just $\lambda = 1$, the material has cubic in-plane symmetry. Positive definiteness of the strain energy density requires $\lambda > 0$ and $-1 < \rho < \infty$.

The singular crack tip fields are contained in the work of Sih $et\ al.$ (1965). Here, mode I and II stress intensity factors are defined such that (2.1) and (2.2) remain in effect, where the functions $\bar{\sigma}_{ij}^{I}$ and $\bar{\sigma}_{ij}^{II}$ now depend on λ and ρ as well as θ. The displacements of the crack faces behind the tip are

$$(\delta_2, \delta_1) = (\lambda^{-3/4}K_I, \lambda^{-1/4}K_{II})8nb_{11}[r/(2\pi)]^{1/2}, \qquad (2.15)$$

where $n = [(1 + \rho)/2]^{1/2}$. The energy release rate for straight-ahead crack advance is

$$G = b_{11}n(\lambda^{-3/4}K_I^2 + \lambda^{-1/4}K_{II}^2) \qquad (2.16a)$$

or, equivalently, in a notation used in the composites literature, as $G = G_I + G_{II}$, where

$$G_I = b_{11}n\lambda^{-3/4}K_I^2, \qquad G_{II} = b_{11}n\lambda^{-1/4}K_{II}^2. \qquad (2.16b)$$

A crack kinking analysis as extensive as that described for the isotropic material has not been performed for orthotropic materials. Many such materials have strongly orthotropic fracture properties, wood and laminated composites being well-known examples. When kinking occurs, it often does so at a right angle to the plane of the crack (ie., $\Omega = 90°$ in Fig. 1) along the plane of the grain or a laminate. Suo $et\ al.$ (1990b) have shown that for $\Omega = 90°$ the generalization of (2.6) is (neglecting T)

$$K_{II}^t = c_{11}\lambda^{-3/8}K_I + c_{12}\lambda^{-1/8}K_{II}, \qquad (2.17)$$

$$K_{II}^t = c_{21}\lambda^{-1/8}K_I + c_{22}\lambda^{1/8}K_{II}.$$

The c's depend on ρ, but this dependence is rather weak.

The energy release rate of the kinked crack tip, G^t, is related to K_I^t and K_{II}^t by an expression similar to (2.16), i.e.,

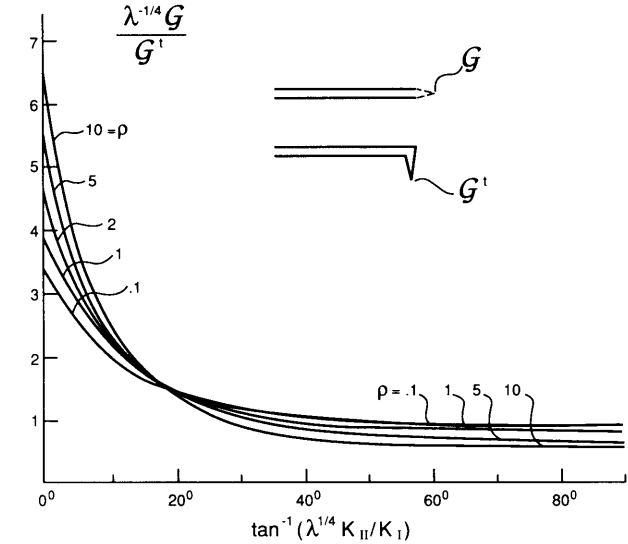$$G^t = b_{22}n(\lambda^{3/4}K_I^{t2} + \lambda^{1/4}K_{II}^{t2}), \qquad (2.18)$$

FIG. 4.   Normalized ratio of energy release rates for orthotropic material.

where λ, n, and ρ remain defined as before. Thus, the ratio of the energy release rates for the competing trajectories can be obtained from (2.16)–(2.18) as

$$\frac{G}{G^t} = \lambda^{1/4}\left[\frac{1 + \zeta^2}{(c_{11}^2 + c_{21}^2) + 2(c_{11}c_{12} + c_{21}c_{22})\zeta + (c_{12}^2 + c_{22}^2)\zeta^2}\right], \qquad (2.19)$$

where $\zeta = \lambda^{1/4}K_{II}/K_I$. This ratio is plotted in Fig. 4. Note that it depends on the relative proportion of K_{II} to K_I but not on their magnitudes.

Suppose the main crack tip is subject to a mode I loading ($K_I > 0$, $K_{II} = 0$). Let Γ_0 be the material toughness associated with straight-ahead crack advance, and Γ_{90} be that associated with crack advance by kinking with $\Omega = 90°$. (Note from (2.17) that the tip of the kinked crack is subject to mixed mode with $K_{II}^t/K_I^t = \lambda^{1/4}c_{21}/c_{11}$. Thus Γ_{90} must represent the mixed mode toughness for cracking parallel to the x_2-plane.) If

$$\frac{G}{G^t} > \frac{\Gamma_0}{\Gamma_{90}},$$

the crack will advance straight ahead since the condition $G = \Gamma_0$ will be reached before $G^t = \Gamma_{90}$. The crack will advance by kinking at 90° if the inequality is reversed. From Fig. 4, it can be seen that the condition on the

toughness ratio for kinking is

$$\frac{\Gamma_{90}}{\Gamma_0} < f(\rho)\lambda^{1/4}, \tag{2.20}$$

where $f(1) = 0.26$, $f(1/10) = 0.29$, and $f(10) = 0.16$.

C. INTERFACE CRACKS

The emphasis of much of this chapter is on the mechanics of interfacial fracture and applications. This section introduces some of the basic results on the characterization of crack tip fields and on specification of interface toughness. If an interface is a low-toughness fracture path through joined solids, then one must be concerned with mixed mode crack propagation since the crack is not free to evolve with pure mode 1 stressing at its tip, as it would in an isotropic brittle solid. The asymmetry in the moduli with respect to the interface, as well as possible nonsymmetric loading and geometry, induces a mode 2 component. The competition between crack advance within the interface and kinking out of the interface depends on the relative toughness of the interface to that of the adjoining material. This competition will be addressed at the end of this section, but first it is necessary to consider how mixed mode conditions affect crack propagation in the interface. The article will focus on isotropic materials. Extensions to anisotropic materials are reviewed in Suo (1990a) and Wang *et al.* (1990).

1. Crack Tip Fields

Consider two isotropic elastic solids joined along the x_1-axis as indicated in Fig. 5 with material 1 above the interface and material 2 below. Let μ_i, E_i, and ν_i ($i = 1, 2$) be the shear modulus, Young's modulus, and Poisson's ratio of the respective materials, and let $\kappa_i = 3 - 4\nu_i$ for plane strain and $\kappa_i = (3 - \nu_i)/(1 + \nu_i)$ for plane stress.

Dundurs (1969) has observed that wide class of plane problems of elasticity for bimaterials depend on only two (rather than three) nondimensional combinations of the elastic moduli. With the convention set in Fig. 5, the Dundurs' elastic mismatch parameters are

$$\alpha = \frac{\mu_1(\kappa_2 + 1) - \mu_2(\kappa_1 + 1)}{\mu_1(\kappa_2 + 1) + \mu_2(\kappa_1 + 1)} \quad \text{and} \quad \beta = \frac{\mu_1(\kappa_2 - 1) - \mu_2(\kappa_1 - 1)}{\mu_1(\kappa_2 + 1) + \mu_2(\kappa_1 + 1)}. \tag{2.21}$$
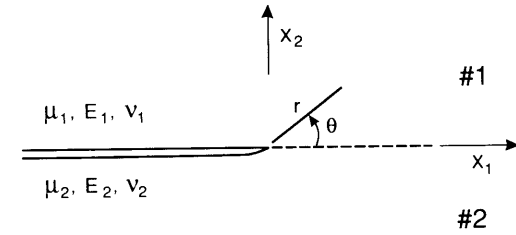
FIG. 5.   Geometry and conventions for an interface crack.

A more revealing expression for α is

$$\alpha = (\bar{E}_1 - \bar{E}_2)/(\bar{E}_1 + \bar{E}_2), \tag{2.22}$$

where $\bar{E}_i \equiv E_i/(1 - \nu_i^2)$ in plane strain and $\bar{E}_i \equiv E_i$ in plane stress. Thus, α measures the mismatch in the plane tensile modulus across the interface. It approaches $+1$ when material 1 is extremely stiff compared to material 2, and approaches -1 when material 1 is extremely compliant. Both α and β vanish when there is no mismatch, and both change signs when the materials are switched.

The parameter β is a measure of the mismatch in the in-plane bulk modulus. In plane strain,

$$\beta = \frac{1}{2} \frac{\mu_1(1 - 2\nu_2) - \mu_2(1 - 2\nu_1)}{\mu_1(1 - \nu_2) + \mu_2(1 - \nu_1)}. \tag{2.23}$$

Thus, in plane strain, β vanishes when both materials are incompressible ($\nu_1 = \nu_2 = 1/2$), and $\beta = \alpha/4$ when $\nu_1 = \nu_2 = 1/3$. In plane stress, $\beta = \alpha/3$ when $\nu_1 = \nu_2 = 1/3$. When $\nu_1 = \nu_2$, α is the same in plane strain and plane stress.

In plane strain, the physical admissible values of α and β are restricted to lie within a parallelogram enclosed by $\alpha = \pm 1$ and $\alpha - 4\beta = \pm 1$ in the (α, β) plane, assuming nonnegative Poisson's ratios. The range of α and β in plane stress is somewhat more restricted. Representative material combinations are plotted for plane strain in Fig. 6, in every case with the stiffer material as material 1 so that α is positive. This plot is similar to one given by Suga *et al.* (1988). Note that most of the (α, β) combinations in Fig. 6 fall between $\beta = 0$ and $\beta = \alpha/4$. Combinations that satisfy $\beta = 0$ give rise to simpler crack tip fields than combinations with $\beta \neq 0$, and special attention will be paid to this restricted family of bimaterials in a separate section following this one.
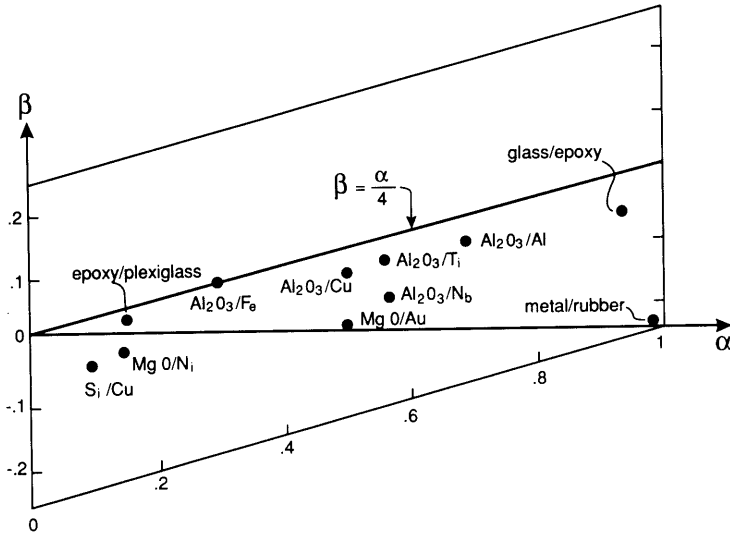
FIG. 6.   Values of Dundurs' parameters in plane strain for selected combinations of materials.

Solutions to bimaterial interface crack problems were presented in the earliest papers on the subject by Cherepanov (1962), England (1965), Erdogan (1965), and Rice and Sih (1965). Williams (1959) investigated the singular crack tip fields. Here, the notations and definitions of Rice (1988) for the crack tip fields will be adopted since these reduce to the conventional notation when the mismatch vanishes. Take the origin at the crack tip, as in Fig 5, with the crack flanks lying along the negative x_1-axis. The dominant stress singularity for any plane problem in which zero tractions are prescribed on a portion of the negative x_1-axis ending at the origin is of the form

$$\sigma_{\alpha\beta} = \text{Re}[Kr^{i\varepsilon}](2\pi r)^{-1/2}\sigma_{\alpha\beta}^{\text{I}}(\theta, \varepsilon) + \text{Im}[Kr^{i\varepsilon}](2\pi r)^{-1/2}\sigma_{\alpha\beta}^{\text{II}}(\theta, \varepsilon), \quad (2.24)$$

where $i = \sqrt{-1}$, r and θ are defined in Fig. 5, and

$$\varepsilon = \frac{1}{2\pi}\ln\left(\frac{1-\beta}{1+\beta}\right). \quad (2.25)$$

The *complex interface stress intensity* factor $K = K_1 + iK_2$ has real and imaginary parts K_1 and K_2, respectively, which play similar roles to the conventional mode I and Mode II intensity factors. The quantities $\sigma_{\alpha\beta}^{\text{I}}$ and $\sigma_{\alpha\beta}^{\text{II}}$ are given by Rice *et al.* (1990); they reduce to the corresponding quantities in (2.1) when $\varepsilon = 0$.

The singular fields are normalized so that the tractions on the interface directly ahead of the tip are given by

$$\sigma_{22} + i\sigma_{12} = (K_1 + iK_2)(2\pi r)^{-1/2}r^{i\varepsilon} \quad (2.26a)$$

or

$$\sigma_{22} = \text{Re}[Kr^{i\varepsilon}](2\pi r)^{-1/2}, \qquad \sigma_{12} = \text{Im}[Kr^{i\varepsilon}](2\pi r)^{-1/2} \quad (2.26b)$$

where $r^{i\varepsilon} = \cos(\varepsilon \ln r) + i \sin(\varepsilon \ln r)$. This is a so-called oscillatory singularity, which brings in some complications that are not present in the elastic fracture mechanics of homogeneous solids, as will be discussed in detail later. The associated crack flank displacements a distance r behind the tip, $\delta_i = u_i(r, \theta = \pi) - u_i(r, \theta = -\pi)$, are given by

$$\delta_2 + i\delta_1 = \frac{8}{(1 + 2i\varepsilon)\cosh(\pi\varepsilon)}\frac{(K_1 + iK_2)}{E_*}\left(\frac{r}{2\pi}\right)^{1/2}r^{i\varepsilon}, \quad (2.27)$$

where

$$\frac{1}{E_*} = \frac{1}{2}\left(\frac{1}{\bar{E}_1} + \frac{1}{\bar{E}_2}\right) \quad (2.28)$$

The energy release rate for crack advance in the interface is (Malyshev and Salganik, 1965)

$$G = \frac{(1 - \beta^2)}{E_*}(K_1^2 + K_2^2), \quad (2.29)$$

which reduces to (2.5) in the absence of mismatch. Equations (2.27) and (2.29) can be re-expressed using the connection $1 - \beta^2 = 1/\cosh^2(\pi\varepsilon)$.

To help motivate the application of the crack tip fields to characterize interface toughness, it is useful to give two examples of stress intensity factors for solved problems. The problem of the isolated crack of length $2a$ lying on the interface between two remotely stressed semi-infinite blocks (see Fig. 7a) was solved in the early papers cited previously. For the right hand tip of the crack,

$$K_1 + iK_2 = (\sigma_{22}^{\infty} + i\sigma_{12}^{\infty})(1 + 2i\varepsilon)(\pi a)^{1/2}(2a)^{-i\varepsilon}. \quad (2.30)$$

This particular set of intensity factors depends on the elastic mismatch only through ε and, by (2.25), is independent of α. The problem of the infinite double cantilever beam (see Fig 7b) loaded with equal and opposite moments (per unit thickness perpendicular to the (1, 2) plane) was solved by Suo and Hutchinson (1990) as the special case of a more general solution
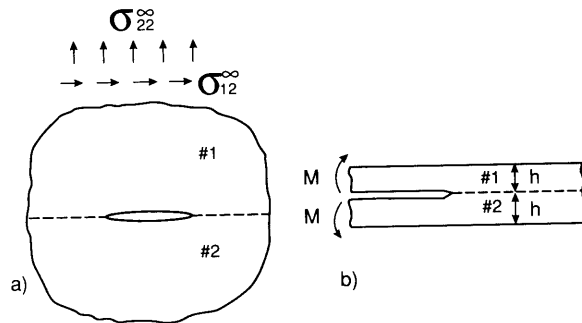
FIG. 7.   Two basic interface crack problems.

FIG. 8.   Phase factor ω^* for the problem of Fig. 7b.

presented in Section III. The solution is

$$K_1 + iK_2 = 2\sqrt{3}\,Mh^{-3/2-i\varepsilon}(1 - \beta^2)^{-1/2}e^{i\omega^*(\alpha,\beta)}, \qquad (2.31)$$

where the function $\omega^*(\alpha, \beta)$ is displayed in Fig. 8.

2. Crack Tip Fields and Interface Toughness with $\beta = 0$

When $\beta = 0$ (and thus $\varepsilon = 0$ by (2.25)), (2.26) becomes

$$(\sigma_{22}, \sigma_{12}) = (K_1, K_2)(2\pi r)^{-1/2}, \qquad (2.32)$$

and (2.27) reduces to

$$(\delta_2, \delta_1) = (8/E_*)(K_1, K_2)[r/(2\pi)]^{1/2}. \qquad (2.33)$$

The interface stress intensity factors K_1 and K_2 play precisely the same role as their counterparts in elastic fracture mechanics for homogeneous, isotropic solids. The mode 1 component K_1 is the amplitude of the singularity of the normal stresses ahead of the tip and the associated normal separation of the crack flanks, while the mode 2 component K_2 governs the shear stress on the interface and the relative shearing displacement of the flanks.

When $\beta \neq 0$, the decoupling of the normal and shear components of stress on the interface and associated displacements behind the tip within the zone dominated by the singularity does not occur. When $\beta \neq 0$, the notions of mode 1 and mode 2 require some modification. In addition, the traction-free line crack solution for the displacements (2.27) implies that the crack faces interpenetrate at some point behind the tip. Both of these features have caused conceptual difficulties in the development of a mechanics of interfaces. For this reason, we have chosen to introduce the elastic fracture mechanics for bimaterial systems with $\beta = 0$, either exactly
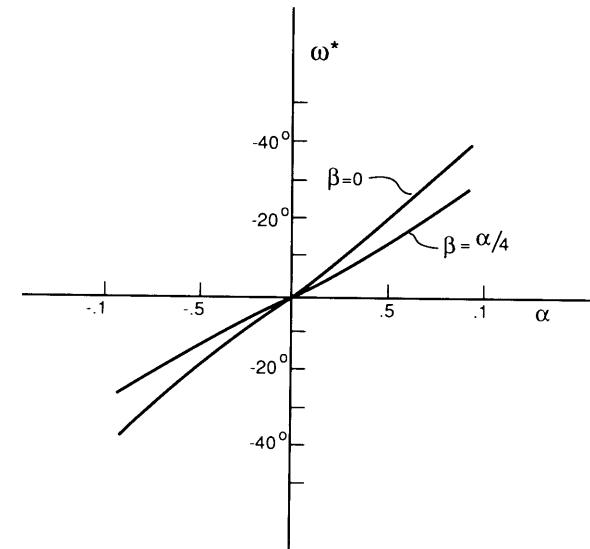
or as an approximation. The extension for systems with $\beta \neq 0$ will be given in the following section, where it will also be argued that the effect of nonzero β is often of secondary consequence.

When $\beta = 0$, take the measure of the relative amount of mode 2 to mode 1 at the crack tip to be

$$\psi = \tan^{-1}(K_2/K_1). \qquad (2.34)$$

The finite crack in the infinite plane, (2.30), gives

$$\psi = \tan^{-1}(\sigma_{12}^\infty/\sigma_{22}^\infty), \qquad (2.35)$$

while the double cantilever beam loaded by equal and opposite moments, (2.31), has

$$\psi = \omega^*(\alpha, 0). \qquad (2.36)$$

The double cantilever has symmetric geometry and loading; the asymmetry is due entirely to the elastic mismatch. Note from Fig. 8 that the specimen is in mode 1 when $\alpha = 0$, as it must by symmetry, but develops a substantial mode 2 component when the elastic mismatch becomes significant.

Efforts to measure interfacial toughness under mixed mode conditions go back some years (e.g., Trantina, 1972, and Anderson et al., 1974), as reviewed by Liechti and Hanson (1988). Parallel efforts have also been

underway to develop mixed mode fracture specimens designed to measure the delamination toughness associated with ply separation in polymer-matrix composites (e.g., Kinloch, 1987). A series of recent experiments (Cao and Evans, 1989; Wang and Suo, 1990; and Liechti and Chai, 1990a) have focussed on the interface between epoxy and glasses, metals and plastics. Thouless (1990b) has carried out mixed mode toughness experiments for crack propagation in the interface between a brittle wax and glass. In all these systems, the interface toughness is not a single material parameter, rather it is a *function* of the relative amount of mode 2 to mode 1 acting on the interface.

The criterion for initiation of crack advance in the interface when the crack tip is loaded in mixed mode characterized by ψ is

$$G = \Gamma(\psi). \qquad (2.37)$$

The toughness of the interface, $\Gamma(\psi)$, can be thought of as an effective surface energy that depends on the mode of loading. Condition (2.37) is also assumed to hold for quasi-static crack advance when crack growth resistance effects can be disregarded.

Data from Wang and Suo (1990) for a crack in a plexiglass/epoxy interface is shown in Fig. 9. This data was obtained using a layer of epoxy sandwiched between two halves of a Brazil nut specimen. The specimen, which will be considered later in Section IV.C.2, enables the experimentalist to vary the mix of loading from pure mode 1 to pure mode 2 by varying the
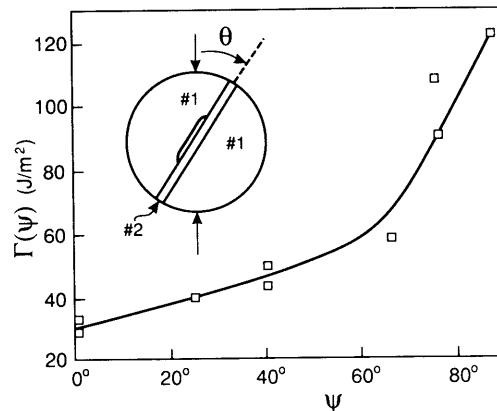

FIG. 9. Interface toughness function for a plexiglass (#1)/epoxy(#2) interface. Obtained using a Brazil nut specimen by Wang and Suo (1990).

angle θ of the compression axis (see the insert in Fig. 9). For the plexiglass (#1)/epoxy(#2) interface in plane strain,

$$\alpha = -0.15, \qquad \beta = -0.029, \qquad \varepsilon = 0.009. \qquad (2.38)$$

The error in taking $\beta = 0$ is negligible for this system as will be clear in the next section. Note, for example, that the error in G in (2.29) from this approximation is less than 0.1%.

3. *Phenomenological Characterization of Interface Toughness*

A micromechanics of interface toughness is not far advanced. An overview of various mechanisms responsible for the strong dependence of interfaced toughness on mode mixity is given by Evans et al. (1990). Two primary mechanisms are asperity contact and plasticity. Asperities on the fracture surfaces will tend to make contact for some distance behind the tip when mode 2 is present along with mode 1. A micromechanics model of shielding of the tip due to asperity interaction was presented by Evans and Hutchinson (1989). That model led to a prediction of $\Gamma(\psi)$ in terms of a nondimensional measure of fracture surface roughness. Crack tip plasticity also depends on ψ, with the plastic zone in plane strain increasing in size as $|\psi|$ increases, with G held fixed (Shih and Asaro, 1988). When an interface between a bimaterial system is actually a very thin layer of a third phase, the details of the cracking morphology in the thin interface layer can also play a role in determining the mixed mode toughness. Some aspects of cracking at the scale of the interface layer itself will be discussed in the final section of this chapter. The approach for the time being is that the interface has zero thickness and is modeled by the toughness function $\Gamma(\psi)$ which, in general, must be determined by experiment.

A simple, one parameter family of mixed mode fraction criteria that captures the trend illustrated by the data in Fig. 9 is

$$E_*^{-1}(K_1^2 + \lambda K_2^2) = G_1^c. \qquad (2.39)$$

The parameter λ adjusts the influence of the mode 2 contribution in the criterion. The limit $\lambda = 1$ is the "ideally brittle" interface with initiation occurring when $G = G_1^c$ for all mode combinations. This limit coincides with the classical surface energy criterion. When $\lambda = 0$, crack advance only depends on the mode 1 component. For any value of λ, G_1^c is the pure mode 1 toughness. The criterion can be cast in the form (2.37) where the mixed mode toughness function is

$$\Gamma(\psi) = G_1^c[1 + (\lambda - 1) \sin^2 \psi]^{-1}. \qquad (2.40)$$
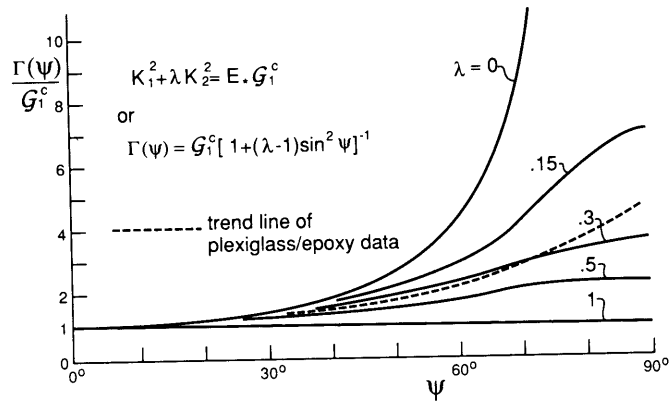
FIG. 10. A family of interface toughness functions and comparison with data for a plexiglass/epoxy interface (represented by the broken line).

The toughness is plotted as a function of ψ in Fig. 10 for various values of λ. Included in this figure is the data for the plexiglass/epoxy interface, which is approximately represented by the choice $\lambda = 0.3$. This particular interface displays a toughness that is far removed from ideally brittle behavior.

The family of criteria (2.39) was extended to include a mode 3 contribution by Jensen *et al.* (1990). In a slightly different form, this family of criteria has been used for some time to characterize interlaminar failure in fiber reinforced composites (*cf.* Kinloch, 1987). When $\beta = 0$, one can introduce "components" of G according to

$$(G_1, G_2) = E_*^{-1}(K_1^2, K_2^2), \qquad (2.41)$$

such that $G = G_1 + G_2$.[†] Alternatively, for a crack in a homogeneous orthotropic material, G_1 and G_2 can be defined using (2.16). The criterion (2.39) can be rewritten as

$$(G_1/G_1^c) + (G_2/G_2^c) = 1, \qquad (2.42)$$

where $G_2^c \equiv G_1^c/\lambda$ has the interpretation as the pure mode 2 toughness.

Other phenomenological criteria have been proposed to characterize mixed mode toughness data for interlaminate fracture (e.g., Kinloch, 1987). Two alternatives to (2.40) are now given which have qualitative features

[†] The components can be regarded as the work of the normal and shear tractions on the interface through their respective crack face displacements as the crack advances. This decomposition does not exist when $\beta \neq 0$.
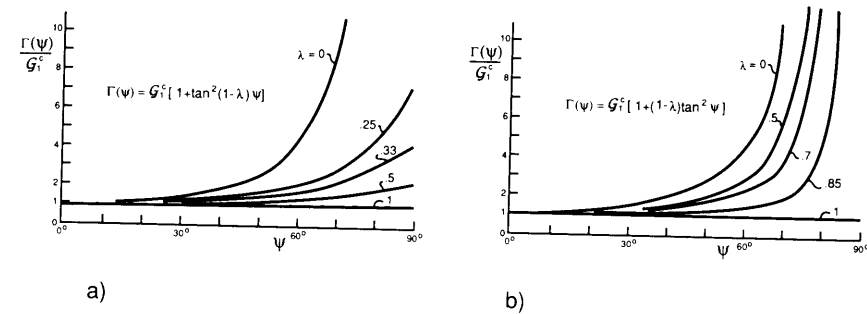
FIG. 11. Alternative families of interface toughness functions.

that may more realistically reproduce data trends for interfacial fracture:

$$\Gamma(\psi) = G_1^c\{1 + \tan^2[(1 - \lambda)\psi]\} \qquad (2.43)$$

and

$$\Gamma(\psi) = G_1^c[1 + (1 - \lambda)\tan^2\psi]. \qquad (2.44)$$

These are plotted in Fig. 11. Both coincide with (2.40) in the limit $\lambda = 0$, i.e., they reduce to a criterion based on a critical value of K_1, independent of K_2. Both are ideally brittle with $\lambda = 1$. According to (2.43), the toughness increases sharply as $\psi \to 90°$ (mode 2), as opposed to (2.40), which has the toughness leveling off as $\psi \to 90°$. Equation (2.44) models the toughness as unbounded as $\psi \to 90°$ for all $\lambda < 1$. While this feature should not be taken literally, it did emerge in the simple model of mixed mode interface toughness due to asperity contact of Evans and Hutchinson (1989). Of the three formulas for $\Gamma(\psi)$, (2.44) most accurately reflects the trends of that model.

All three of the interface toughness functions $\Gamma(\psi)$ are symmetric in ψ. In general, symmetry of interface toughness with respect to ψ should not be expected. Some evidence that $\Gamma(\psi)$ is asymmetric for an epoxy/glass interface will be presented in the next section.

4. Interface Toughness with $\beta \neq 0$

When $\beta \neq 0$, the notion of a mode 1 or a mode 2 crack tip field must be defined precisely, and the possibility of contact of the crack faces within the region dominated by the near tip K-fields must be considered. As noted by Rice (1988), a generalized interpretation of the mode measure is the most important complication raised by the oscillatory singularity, and the

approach recommended here follows largely along the lines of one of his proposals. First, a definition of a measure of the combination of modes is made that generalizes (2.34).

Let l be a reference length whose choice will be discussed later. Noting the stress distribution (2.26b) on the interface from the K-field, define ψ as

$$\psi = \tan^{-1}\left[\frac{\mathrm{Im}(Kl^{i\varepsilon})}{\mathrm{Re}(Kl^{i\varepsilon})}\right], \tag{2.45}$$

where $K = K_1 + iK_2$ is the complex stress intensity factor. For a choice of l within the zone of dominance of the K-field, (2.45) is equivalent to (cf. (2.26b))

$$\psi = \tan^{-1}\left[\left(\frac{\sigma_{12}}{\sigma_{22}}\right)_{r=l}\right]. \tag{2.46}$$

Moreover, the definition reduces to (2.34) when $\beta = 0$, since $l^{i\varepsilon} = 1$ when $\varepsilon = 0$. When $\varepsilon \neq 0$, a mode 1 crack is one with zero shear traction on the interface a distance l ahead of the tip, and a mode 2 crack has zero normal traction at that point. The measure of the proportion of ''mode 2'' to ''mode 1'' in the vicinity of the crack tip requires the specification of *some* length quantity since the ratio of the shear traction to normal traction varies (very slowly) with distance to the tip when $\beta \neq 0$.

The choice of reference length l is somewhat arbitrary, as will be made clear in the following. It is useful to distinguish between a choice based on an in-plane length L of the specimen geometry, such as crack length, and a choice based on a material length scale, such as the size of the fracture process zone or a plastic zone at fracture. The former is useful for discussing the mixed mode character of a bimaterial crack solution, independent of material fracture behavior, while the latter is advantageous in interpreting mixed mode fracture data, as will be discussed. When there is the need to keep the two types of choices clearly distinct, the notation (ψ, l) will be used for a choice based on the specimen geometry and $(\hat{\psi}, \hat{l})$ will be reserved for a material-based choice.

The solution for the complex stress intensity factor to any plane elasticity problem for an interface crack will necessarily have the form

$$K = (\text{applied stress}) \times FL^{1/2-i\varepsilon}, \tag{2.47}$$

where L is some in-plane length, such as crack length or uncracked ligament length, and F is a complex-valued, dimensionless function of dimensionless

groups of moduli, and in-plane length quantities. Equations (2.30) and (2.31) are two examples. The term $Kl^{i\varepsilon}$ in the definition of ψ will therefore always involve a dimensionless combination such as $(l/L)^{i\varepsilon} \equiv \exp[i\varepsilon \ln(l/L)]$. For example, the bimaterial double cantilever beam specimen (2.31) has

$$\psi = \omega^*(\alpha, \beta) + \varepsilon \ln(l/h), \tag{2.48}$$

which generalizes (2.36).

The freedom in the choice of l in the definition of ψ is a consequence of the simple transformation rule from one choice to another. Let ψ_1 be associated with l_1, and ψ_2 with l_2. From the definition in (2.45) one can readily show

$$\psi_2 = \psi_1 + \varepsilon \ln(l_2/l_1). \tag{2.49}$$

Thus, as noted by Rice (1988), it is a simple matter to transform from one choice to another. In particular, toughness data can readily be transformed, as will be discussed in the following.

Let $\hat{l}$ denote a length characterizing the size of the fracture process zone or, perhaps, the typical size of the plastic zone at fracture, and let $\hat{\psi}$ be associated through (2.45). Since small-scale yielding or a small-scale fracture process zone is assumed, $\hat{l}$ necessarily lies within the zone of dominance of the K-field. Given the choice $\hat{l}$, the criterion for interface cracking can again be stated as (2.37), i.e.,

$$G = \Gamma(\hat{\psi}, \hat{l}), \tag{2.50}$$

where the implicit dependence of the toughness function on $\hat{l}$ has been noted. In words, $\Gamma(\hat{\psi}, \hat{l})$ is the critical value of the energy release rate needed to advance the crack in the interface in the presence of a combination of tractions whose relative proportion is measured by $\hat{\psi}$. By (2.49), change in one choice of length in the definition of ψ to another only involves a shift of the ψ-origin of Γ according to

$$\Gamma(\psi_2, l_2) = \Gamma(\psi_1 + \varepsilon \ln(l_2/l_1), l_1), \tag{2.51}$$

as depicted in Fig. 12. When ε is small, the shift will generally be negligible even for changes of l of several orders of magnitude. This is the case for the plexiglass/epoxy interface (2.38). An illustration for which the ε-effect is not negligible in reporting interface toughness is discussed shortly.

In discussing the mixed mode character of a given elasticity solution, it is generally convenient to identify l with an in-plane length of the geometry, such as L in (2.47). For example, if for the double cantilever beam specimen
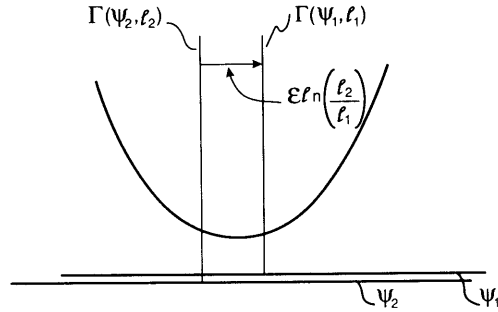
FIG. 12.   Procedure for shifting toughness function from one choice of reference length to another.

one picks $l = h$, then by (2.48),

$$\psi = \omega^*(\alpha, \beta), \qquad (2.52)$$

which is *independent* of the size of the specimen.[†] This is necessarily a feature of any choice of l that scales with an in-plane length. By contrast, for a choice $\hat{l}$ that is *fixed* at some microstructural length, $\hat{\psi}$ varies with specimen size, e.g., for the double cantilever specimen,

$$\hat{\psi} = \omega^*(\alpha, \beta) + \varepsilon \ln(\hat{l}/h). \qquad (2.53)$$

This reflects the fact that the ratio of σ_{12} to σ_{22} at a fixed distance $r = \hat{l}$ ahead of the tip varies as the specimen size changes. Standard arguments underlying the mechanics of fracture, based on Irwin's notion of autonomous crack tip behavior, require that $\Gamma(\hat{\psi}, \hat{l})$ be *independent* of specimen size (assuming, of course, that small scale processes are in effect), while $\Gamma(\psi, l)$ will depend on specimen size if $\varepsilon \neq 0$ when l scales with specimen size. This property, together with the interpretation of mixity in (2.45) in the vicinity of the fracture process zone, favors the choice of a material-based $\hat{l}$ for presenting toughness data.

Liechti and Chai (1990a, b) have developed a bimaterial interfacial fracture specimen that is capable of generating the interface toughness function Γ over essentially the full range of ψ. A schematic of their plane strain specimen is shown in the insert in Fig. 13. The in-plane length of the specimen is long compared to the thickness h of each layer. The bottom

[†] The fact that $l = h$ obviously lies outside the zone of dominance of the K-field is of no consequence. The essential point is that any choice of l is acceptable as long as it is recorded along with the result for ψ, and as long as one is cognizant of the transformation rule.
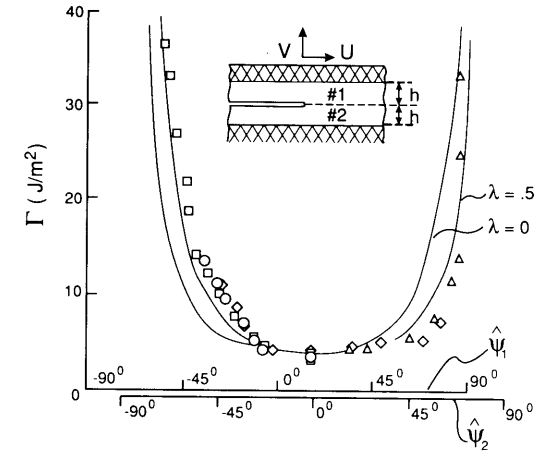
FIG. 13.   Data of Liechti and Chai (1990a) for an epoxy (#1)/glass(#2) interface: $\hat{\psi}_1$ is based on $\hat{l}_1 = 12.7$ mm and $\hat{\psi}_2$ on $\hat{l}_2 = 127 \mu$m. The solid curves are $\Gamma(\hat{\psi}_2)$, where Γ is given by (2.44).

surface is rigidly held and the upper surface is attached to a rigid grip that can impose a horizontal, U, and vertical, V, in-plane displacement. The solution to the problem when the layers are infinitely long and the interface crack is semi-infinite was used by Liechti and Chai to obtain the values of K_1 and K_2 (and G and ψ) associated with the measured combinations of U and V at which the crack propagated in the interface. For plane strain, the solution is (see Section III.C)

$$K_1 + iK_2 = \frac{\sqrt{2}\mu_1\mu_2 h^{-1/2-i\varepsilon}e^{i\omega}(cV + iU)}{(1 - \beta^2)^{1/2}(\mu_1 + \mu_2)^{1/2}[\mu_1(1 - v_2) + \mu_2(1 - v_1)]^{1/2}}, \qquad (2.54)$$

where ω is a real quantity that depends on μ_1/μ_2, v_1, and v_2 and

$$c = \left\{ \frac{2(\mu_1 + \mu_2)}{\mu_1[(1 - 2v_2)/(1 - v_2)] + \mu_2[(1 - 2v_1)/(1 - v_1)]} \right\}^{1/2}. \qquad (2.55)$$

Let γ measure the relative proportion of U to cV applied to the specimen, and define it by

$$\gamma = \tan^{-1}[U/(cV)]. \qquad (2.56)$$

Then, with l as the reference length, (2.45) gives

$$\psi = \gamma + \omega + \varepsilon \ln(l/h). \qquad (2.57)$$

The data for $\Gamma(\hat{\psi}, \hat{l})$ in Fig. 13 was measured by Liechti and Chai for an epoxy(#1)/glass(#2) interface with the following properties for the system: $E_1 = 2.07$ GPa, $E_2 = 68.9$ GPa, $\nu_1 = 0.37$, $\nu_2 = 0.20$, and $h = 12.7$ mm. The plane strain Dundurs' parameters and the oscillation index are

$$\alpha = -0.935, \qquad \beta = -0.188, \qquad \text{and} \qquad \varepsilon = 0.060. \qquad (2.58)$$

For this system $\omega = 16°$ (see Section III.C). Liechti and Chai took $\hat{l} = 12.7$ mm in their definition of ψ, coinciding with the thickness h of the layers.

Liechti and Chai recorded plastic zones in the epoxy to be approximately on the order of 1 μm when $\hat{\psi} \cong 0°$ and 140 μm when $\hat{\psi} \cong 90°$. If instead of $\hat{l} = 12.7$ mm, $\hat{l}$ is chosen to be two orders of magnitude smaller (i.e., $\hat{l} = 127\,\mu$m), the shift in the $\hat{\psi}$-origin from (2.49) or (2.51) is $-15.8°$. This choice seems somewhat more natural in terms of the interpretation given earlier since now $\hat{l}$ lies well within the zone of dominance of the K-field and has a microstructural identity. This choice also places the origin of the $\hat{\psi}$-axis (i.e., "mode 1" for this choice of l) at the approximate minimum of Γ and roughly centers the data, as can be seen in Fig. 13. Nevertheless, some asymmetry in Γ with respect to $\hat{\psi}$ still persists. Included in this figure is the toughness function $\Gamma(\psi)$ from (2.44) for two choices of λ, with G_1^c chosen to coincide with the measured value at $\hat{\psi}_2 = 0$. Apart from the asymmetry in the data, a λ-value between 0 and 0.5 would seem to give an approximate characterization of the data over the range of $\hat{\psi}$ shown. Other important aspects of the mixed mode fracture behavior of this system have been discussed by Liechti and Chai (1990a). These include possible correlation of the strong increase in toughness with mode 2 with either fracture surface roughness or plasticity, and the role of contact between crack faces when the loading becomes dominantly mode 2.

When interpenetration of the crack faces is predicted on the basis of the formulation for a traction-free line crack, the consequences of contact must be taken into account in any application of the solution to fracture. The bimaterial problem with $\beta \neq 0$ is unusual in that interpenetration of the faces always occurs according to (2.27). This feature of the interface crack problem was noted in the earliest papers on the subject, and solutions to specific problems posed with allowance for contact have been produced (Comninou, 1977, and Comninou and Schmueser, 1979). Fortunately, under most loadings likely to be of concern, the contact zone predicted by the elasticity solution is tiny compared with relevant near tip physical features such as the fracture process zone or the plastic zone. The larger the

proportion of mode 2, the more likely is contact of the crack faces to be an issue.[†]

To see this, a rough estimate of the size of the contact zone is obtained. The estimate is that of Rice (1988), as elaborated on by Wang and Suo (1990). Here, however, emphasis is placed on a definition of $\hat{\psi}$ in (2.45) based on a microstructural scale length $\hat{l}$. For $r < \hat{l}$, it will be assumed that the fracture process or other inelastic effects supercede linear elasticity. Using the definition of ψ in (2.45), one can readily show that the normal crack face displacement in the near tip region from (2.27) is

$$\delta_2 = |\delta_2 + i\delta_1| \cos[\hat{\psi} + \varepsilon \ln(r/\hat{l}) - \tan^{-1}(2\varepsilon)]. \qquad (2.59)$$

Consider the condition for the crack to be open ($\delta_2 > 0$) for $\hat{l} < r < L/10$. The factor 1/10 is arbitrary, but the near tip fields should not be expected to retain accuracy for r larger than some fraction of L. If contact occurs outside the preceding range, it must be assessed using the full solution. If $\varepsilon > 0$, the stated condition is met if

$$-\frac{\pi}{2} + 2\varepsilon < \hat{\psi} < \frac{\pi}{2} + 2\varepsilon - \varepsilon \ln\left(\frac{1}{10}\frac{L}{\hat{l}}\right), \qquad (2.60)$$

where $\tan^{-1}(2\varepsilon)$ has been approximated by 2ε since $|\varepsilon| \leq 0.175$. For $\varepsilon < 0$, there will be no contact over the specified region as long as

$$-\frac{\pi}{2} + 2\varepsilon - \varepsilon \ln\left(\frac{1}{10}\frac{L}{\hat{l}}\right) < \hat{\psi} < \frac{\pi}{2} + 2\varepsilon. \qquad (2.61)$$

The ε-dependence of the above constraints is inconsequential for many interface systems. For the epoxy/glass system (2.58), which has a relatively large ε-value, (2.60) becomes $-83.1° < \hat{\psi} < 89.0°$ for $L/\hat{l} = 100$ and $-83.1° < \hat{\psi} < 73.2°$ for $L/\hat{l} = 10^4$. The difference between the limits obtained above and those derived by Rice (1988) and Wang and Suo (1990) is due mainly to the use in the present work of the material-based definition of $\hat{\psi}$, rather than ψ defined in terms of a length L characterizing the specimen. The combination of the contact due to nonzero ε and the contact arising from fracture surface asperities has not been modeled. The interaction between these two effects acting in concert should be important for mixed mode loadings near the limits listed above.

[†]Now the contact is not due to asperity roughness on the crack faces generated by the fracture process that was discussed earlier. Here, the crack faces are imagined to be smooth and "just touching" in the unloaded state.
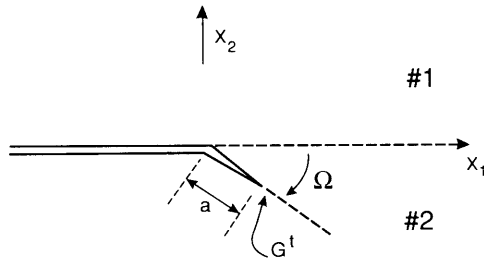
FIG. 14.   Conventions for a crack kinking out of an interface.

5. *Kinking Out of the Interface*

The analysis of kinking parallels that was discussed in Section A for the isotropic elastic solid, and the results presented in what follows are taken from He and Hutchinson (1989a) and He *et al.* (1991). As depicted in Fig. 14, a semi-infinite crack lies along the interface with its tip at the origin. Prior to kinking ($a = 0$), the parent crack is loaded with a complex interface stress intensity factor $K = K_1 + iK_2$ with mixity ψ defined by (2.45) relative to some reference length l. For definiteness, ψ will be taken to be positive with kinking down into material #2 as shown in Fig. 14. Negative ψ-loadings with upward kinking can be analyzed by exchanging the materials, i.e., switching the signs on α and β.

As in the analysis for the isotropic solid, the energy release rate G for straight-ahead advance in the interface is compared with the energy release rate G^t for a crack with a segment of length a kinking at an angle Ω to the interface. The energy release rate G for advance in the interface is given by (2.29). The conventional mode I and mode II stress intensity factors at the tip of the kinked crack tip are related to K by

$$K_{\mathrm{I}} + iK_{\mathrm{II}} = c(\Omega, \alpha, \beta)Ka^{i\varepsilon} + \bar{d}(\Omega, \alpha, \beta)\bar{K}a^{-i\varepsilon} + b(\Omega, \alpha, \beta)Ta^{1/2}, \quad (2.62)$$

where T is the nonsingular contribution to σ_{11} in material #2 at the parent crack tip prior to kinking. The T-stress may arise from remote applied load or it may be present as a residual stress. The functions c, d, and b are complex-valued; c and d are tabulated in He and Hutchinson (1989b), while b is given in He *et al.* (1991).

The energy release rate at the kinked crack tip, G^t, is given by (2.5), and the ratio of the two release rates has the form

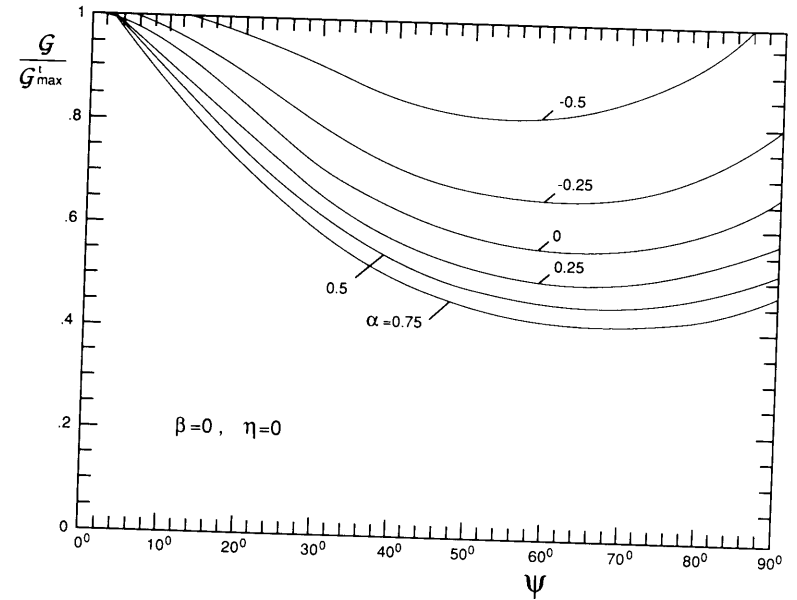$$G/G^t = F(\Omega, \tilde{\psi}, \eta, \alpha, \beta), \quad (2.63)$$

FIG. 15.   Ratio of energy release rate for advance in the interface to the maximum energy release rate for the kinked crack for various levels of elastic mismatch, all with $\beta = 0$.

where $\eta = T[a/(E_*G)]^{1/2}$ and

$$\tilde{\psi} = \psi + \varepsilon \ln(a/l). \quad (2.64)$$

The complete expression for F is given by He *et al.* (1991). The a-dependence of this ratio appears through η, and weakly through $\tilde{\psi}$.

The ratio $G/G^t_{\max}$ is plotted against ψ in Fig. 15 for various values of α, in each case for $\beta = 0$ and $\eta = 0$. Here, $G^t_{\max}$ is the maximum of G^t with respect to kink angle Ω for a given ψ. As in the case of the homogeneous isotropic kinking problem, there is very little difference between the kink angle that maximizes G^t and that which is associated with $K_{\mathrm{II}} = 0$. The only exception occurs when material 2 is very stiff compared with material 1 ($\alpha < -0.67$). Then, there exists a range of ψ for which the maximum G^t occurs at small kink angles while the kink angle associated with $K_{\mathrm{II}} = 0$ is near 45° (He and Hutchinson, 1989a). With $\Gamma(\psi)$ denoting the toughness function of the interface and Γ_c denoting the mode I toughness of material 2, kinking will be favored over continued interface cracking if

$$G/G^t_{\max} < \Gamma(\psi)/\Gamma_c, \quad (2.65)$$

and conversely. Thus, the curves of $G/G_{\max}^{t}$ in Fig. 15 also give the transition value of interface to substrate toughness, $\Gamma(\psi)/\Gamma_c$, separating the tendency for kinking over interface cracking.

The effect of β on the ratio in (2.63) is relatively weak, as discussed by He and Hutchinson (1989a). The dependence on a through $\tilde{\psi}$ in (2.63) can be interpreted as a shift in the phase of the mode of loading on the interface crack. The influence of η is given by He et al. (1991), and is qualitatively similar to that shown in Fig. 2 for the isotropic case.

III. Elasticity Solutions for Cracks in Multilayers

In studying cracks in multilayers, it is found that the crack driving force for many situations is essentially independent of the crack size. This steady-state concept and its implications are elucidated with two examples. Heuristic conclusions thus drawn allow emphasis to be placed on various steady-state problems. Several elasticity solutions for mixed mode cracks in multilayers are gathered in this chapter. The geometries can be found in the figures in this chapter. These solutions were obtained in recent years by analytical and numerical methods, and have been used to calibrate fracture specimens and assess technically representative structures. Details of applications will be given in the subsequent chapters. We will omit several classical exact solutions of interface crack problems obtained in 1965 by Erdogan, England, Rice and Sih. These solutions and some extensions have been reviewed by Suo (1989, 1990a).

A. CONCEPT OF STEADY-STATE CRACKING

For applications to be discussed in the following chapters, the concept of steady-state cracking results in a significant simplification. The purpose of this section is to discuss the concept and its implications using two examples: tunneling in adhesives and delamination in unidirectional composites. We try to convey that the steady-state solutions developed in later sections, although highly idealized, can be used to model real-world phenomena.

1. Tunneling in Adhesives

Consider residual stress cracks in adhesives as illustrated in Fig. 16. A thin, brittle adhesive layer is bonded between two substrates. Biaxial residual stresses usually develop in the adhesive layer during the bonding
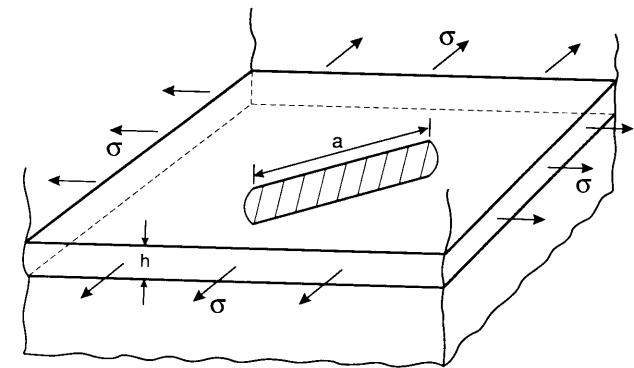
FIG. 16. A thin adhesive layer bonded between two substrates is under biaxial tensile stress. A crack is tunneling through the layer. The substrate on the top is removed for better visualization.

process. In glaze bonding, for example, the ceramic parts are coated with a glass; the parts are placed in contact and heated above the melting temperature of the glass, and then cooled down to the room temperature. For such inorganic adhesives, a major source of the residual stress is thermal expansion mismatch. The residual stress is tensile when the adhesive has larger thermal expansion coefficient than the substrates, which causes cracks to tunnel through the adhesive. Similar cracks are observed in hybrid laminates consisting of alternate tough and brittle sheets, and in coatings or reaction product layers between reinforcements and in matrices in brittle composites. Cracks may penetrate into substrates if the latter are brittle. Debonding is also possible at the intersection of the interfaces and cracks.

Illustrated in Fig. 16 is a crack, nucleated from a flaw, tunneling through the layer. Substrate penetration and interface debonding are assumed not to occur. Crack nucleation is a rather complicated process: A gas bubble would behave differently from a crack-like defect in activating a tunnel. However, as a crack grows long compared with layer thickness, the problem becomes much better defined. A *steady-state* is reached: The tunnel front maintains its shape as it advances, and the energy released per unit advance no longer depends on the tunnel length, nor on the initial flaw geometry. The steady-state problem is still three-dimensional in nature, since the shape of the front should be determined so that the same mode I stress intensity factor is reached at every point along the front. However, this stress intensity factor itself can be calculated without knowing the shape of the front by using a two-dimensional elasticity solution. This attractive possibility

follows from the fact that the energy released per unit length of tunneling equals the energy released to form a plane strain crack traversing the layer, per unit width of crack For adhesive and substrates with identical elastic constants, the solution (Suo 1990b)

$$K_I = \frac{\sqrt{\pi}}{2} \sigma \sqrt{h} \approx 0.89 \sigma \sqrt{h} \qquad (a/h \to \infty). \qquad (3.1)$$

As indicated, the result is valid for the steady-state, that is, when the tunnel is long compared with the thickness of the adhesive layer.

Another limiting case with readily available exact solution is a penny-shaped crack of diameter h. The stress intensity factor along the entire circular front is the same (so it may be thought of as an incipient tunnel), having the value (Tada *et al.* 1985)

$$K_I = \sqrt{2/\pi} \, \sigma \sqrt{h} \approx 0.80 \sigma \sqrt{h} \qquad (a/h = 1). \qquad (3.2)$$

Observe that the two results just cited are not very different, suggesting only a mild dependence on a/h. The steady state is practically attained after the tunnel length exceeds a few times adhesive thickness. If the penny-shaped crack is representative of initial flaws, the critical stress needed for the steady-state propagation is only about 10% below the stress to initiate unstable growth from the flaw.

Several implications follow. The tunneling, once activated, would never arrest until it meets another crack or other obstacles. Consequently, under a biaxial stress, a connected tunnel network would emerge, surrounding islands of intact adhesive materials; see Zdaniewski *et al.* (1987) for micrographs. Another implication is that the transient dependence on a/h, which can only be obtained from a complicated three-dimensional analysis, would be unnecessary for most practical purposes. Instead, the steady-state solution provides a conservative, yet still quite tight, design limit. For example, given the substrate and adhesive materials (so the toughness and mismatch stress are fixed), (3.1) would predict the thickest adhesive that can be used with no tunneling cracks. More details of this problem are given in Section VIII.

2. *Delamination near a Surface Flaw*

As a second example, consider the delamination near a surface notch in a unidirectional composite; see the insert in Fig. 17. The incipient delamination is not well characterized for two reasons. First, the driving force
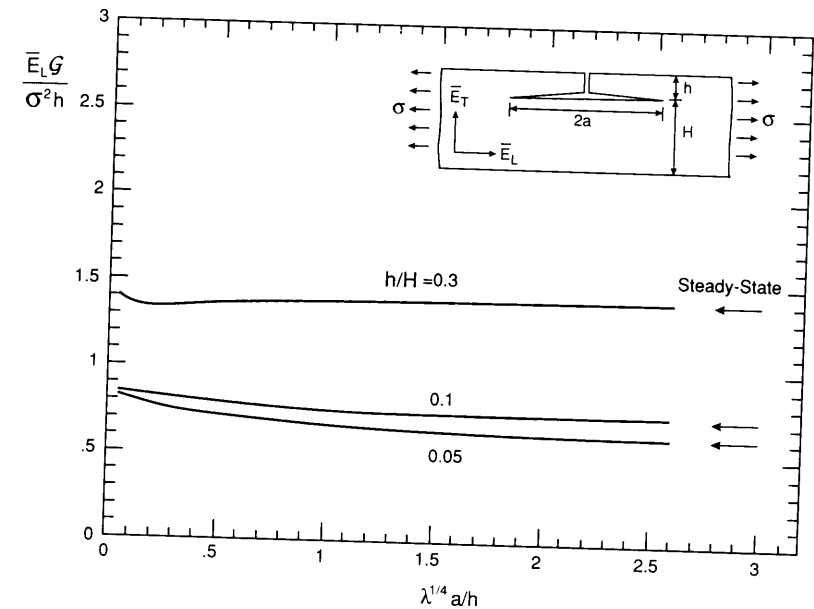
FIG. 17. The insert shows a delamination nucleated from a surface notch and driven by a longitudinal tension. The normalized energy release rate is plotted against the effective delamination length $\lambda^{1/4}a/h$ for several values of notch size h/H. The energy release rate attains the steady-state as soon as $\lambda^{1/4}a/h > 1.5$.

depends on the notch geometry. Secondly, composites usually exhibit R-curve behavior: Fracture resistance increases as the crack extends. This can be caused by bridging fibers or matrix ligaments in the wake. However, once the delamination is sufficiently long, a steady state should be reached: Both driving force and toughness become independent of the delamination length and initial flaw geometry. The following example establishes the transient zone size for the driving force. The R-curve behavior will be discussed in Section IV.D.

Figure 17 shows a delamination crack nucleated from a sharp notch and driven by an axial tension. Similar problems have been studied by several authors (e.g., O'Brien, 1984, Thouless *et al.*, 1989). The solution that follows is taken from Suo *et al.* (1990b). The delamination is mixed mode. The energy release rate takes the dimensionless form

$$\frac{\bar{E}_L G}{\sigma^2 h} = g\left(\lambda^{1/4} \frac{a}{h}, \frac{H}{h}, \rho \right) \qquad (3.3)$$

where $\bar{E}_L \equiv 1/b_{11}$ is the effective Young's modulus in the longitudinal direction, λ and ρ are orthotropy parameters, all defined in Section II.B. The dimensionless function g depends on the indicated variables. Notice that λ and a/h affect the final results only through the product $\lambda^{1/4}a/h$, as identified in the original paper using orthotropy rescaling. This detail turns out to be important in understanding the orthotropy effects, as will be seen shortly. Figure 17 plots the solution obtained by finite elements, with $\rho = 1$.

Observe that the energy release rate becomes independent of $\lambda^{1/4}a/h$ when the delamination is sufficiently long. An inspection of Fig. 17 suggests that the *transient-zone* size is given by $\lambda^{1/4}a/h \approx 1.5$, or

$$a/h \approx 1.5(\bar{E}_L/\bar{E}_T)^{1/4}, \qquad (3.4)$$

where $\bar{E}_T \equiv 1/b_{22}$ is the effective Young's modulus transverse to the fiber direction. For most polymer composites and woods, $(\bar{E}_L/\bar{E}_T)^{1/4} \approx 2$. Consequently, a split longer than about three times the notch depth is subject to a constant driving force. Equation (3.4) also reveals that elastic orthotropy tends to *prolong* the transient zone by a factor of $(\bar{E}_L/\bar{E}_T)^{1/4}$, as compared with the isotropic counterpart. Finite element calculations (not shown here) also indicate that the size of the transient zone is not significantly affected by ρ within the practical range, so that (3.4) remains valid for general orthotropic materials.

An accurate approximation for the steady-state mixed mode energy release rates at the delamination tip in Fig. 17 is (Suo 1990c)

$$[G_I, G_{II}] = \frac{\sigma^2 h}{2\bar{E}_L}(1 + 4\eta + 6\eta^2 + 3\eta^3)[\cos^2\omega, \sin^2\omega],$$

$$\omega = 52.1° - 3°\eta, \qquad \eta = h/H. \qquad (3.5)$$

This steady-state solution $G = G_I + G_{II}$, is indicated in Fig. 17.

In conclusion, the steady-state condition can usually be easily attained in practice. These steady-state solutions are of unique significance considering the variety of uncertainties associated with the transient state. Mathematically, the steady-state concept allows one to bypass some messy intermediate calculations. Although an accurate estimate of the transient-zone size may not be available for each steady-state solution described in the rest of the section, we feel that, in conjunction with some heuristic judgment, these solutions can be used to assess technical structures.
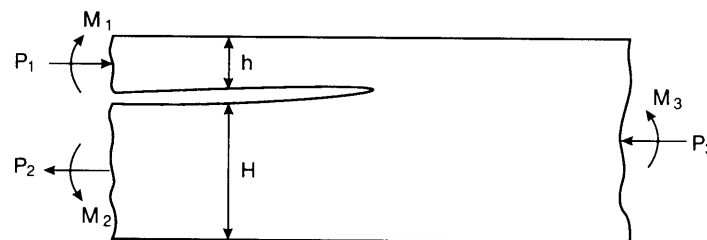
FIG. 18.   Cross-section of an infinite layer with a half-plane crack. Axial forces and moments, per unit width, are applied along the three edges.

B. CRACKS IN LAYERS LOADED ALONG EDGES

The problems to be disussed in this section are sketched in Fig. 18. The layer can be of one material or bimaterial, the material isotropic or orthotropic, the crack along the interface or in the substrate. The relation is sought between the applied loads and the mixed mode stress intensity factors.

1. *A Homogeneous, Isotropic Layer*

Depicted in Fig. 18 is the cross-section of an infinite layer containing a half-plane crack. The geometry is fully specified by h and H, the thicknesses of the two separated arms. The layer is isotropic, homogeneous and linearly elastic, and is subject, uniformly along the three edges, to axial forces and moments per unit width P_i and M_i. The problem at various levels of generality has been considered by several authors (Tada *et al.*, 1985; Williams, 1988; Suo and Hutchinson, 1989b; Schapery and Davidson, 1990). The results in the first two of these references contain conceptual errors. The complete solution presented below is taken from Suo (1990c).

a. *General Solution*

The near-tip stresses are consistent with the mixed mode crack tip field, with stress intensity factors K_I and K_{II} to be determined. Far from the tip, the three edges are characterized by the linear strain distributions for elementary beams. The energy release rate equals the difference of the strain energy per unit length per unit width stored in the edges far behind and far ahead of the crack tip. Thus,

$$G = \frac{1}{2\bar{E}}\left[\frac{P_1^2}{h} + 12\frac{M_1^2}{h^3} + \frac{P_2^2}{H} + 12\frac{M_2^2}{H^3} - \frac{P_3^2}{h+H} - 12\frac{M_3^2}{(h+H)^3}\right], \qquad (3.6)$$

where $\bar{E}$ is the effective Young's modulus defined in (2.4). This result may be derived alternatively by using the J-integral (Rice, 1968; Cherepanov, 1979).

The preceding energy accounting does not separate the opening and shearing components. The partition is simplified by *linearity* and *dimensionality*, coupled with the Irwin relation (2.5). Consequently, the stress intensity factors take the form

$$K_{\mathrm{I}} = \frac{P}{\sqrt{2hU}} \cos \omega + \frac{M}{\sqrt{2h^3 V}} \sin(\omega + \gamma),$$

$$K_{\mathrm{II}} = \frac{P}{\sqrt{2hU}} \sin \omega - \frac{M}{\sqrt{2h^3 V}} \cos(\omega + \gamma). \tag{3.7}$$

All the preceding quantities except ω are determined by elementary considerations. Specifically, P and M are linear combinations of the applied loads:

$$P = P_1 - C_1 P_3 - C_2 M_3/h, \qquad M = M_1 - C_3 M_3,$$

$$C_1 = \frac{1}{1/\eta + 1}, \quad C_2 = \frac{6/\eta}{(1/\eta + 1)^3}, \quad C_3 = \frac{1}{(1/\eta + 1)^3} \quad \eta = h/H; \tag{3.8}$$

and the geometric factors are functions of η:

$$\frac{1}{U} = 1 + 4\eta + 6\eta^2 + 3\eta^3, \quad \frac{1}{V} = 12(1 + \eta^3), \quad \frac{\sin \gamma}{\sqrt{UV}} = 6\eta^2(1 + \eta). \tag{3.9}$$

Accurate determination of ω, which depends only on η, is nontrivial. The elasticity problem was solved rigorously (with the help of numerical solutions of an integral equation). The extracted ω varies slowly with η in the entire range $0 \le \eta \le 1$, in accordance with an approximate formula

$$\omega = 52.1° - 3°\eta. \tag{3.10}$$

This is a linear fit of the numerical solution, and the error is believed to be within one percent.

b. A Mixed Mode Double Cantilever Beam

Several special cases are discussed here to illustrate the richness of the solution. First consider a double cantilever beam as in Fig. 19. The specimen is mode I if the crack lies on the mid-plane, but mixed mode if the crack is off the mid-plane. This has been used recently to study mixed mode
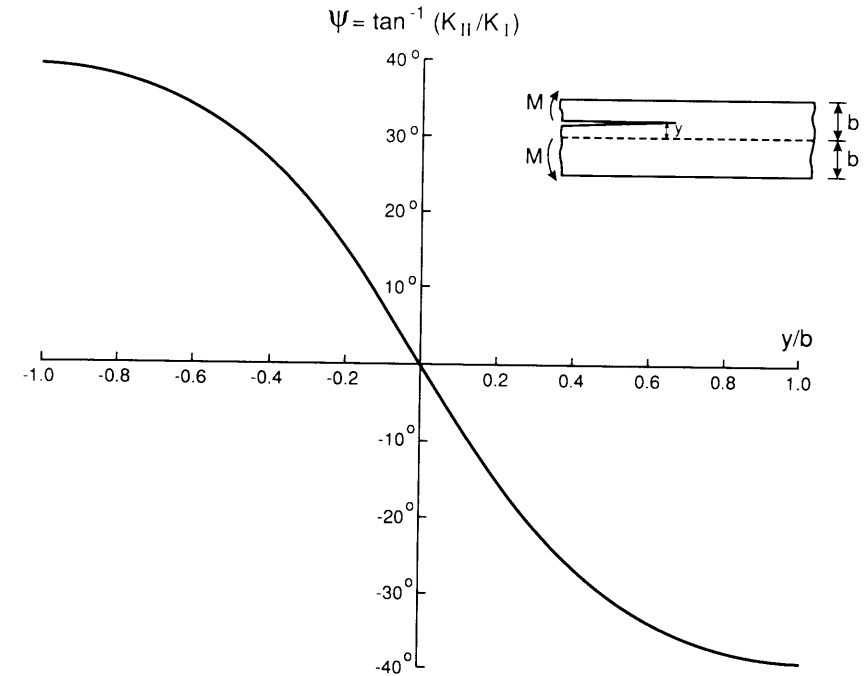
FIG. 19.   The insert shows a double cantiliver beam with a crack off the mid-plane. The mode mixity $\psi = \tan^{-1}(K_{\mathrm{II}}/K_{\mathrm{I}})$ is plotted against the offset y/b.

fracture of an adhesive layer by Thouless (1990b). On Fig. 19, the mode mixity, $\psi = \tan^{-1}(K_{\mathrm{II}}/K_{\mathrm{I}}) = \omega + \gamma - \pi/2$, is plotted against the offset y/b. Focus here is on the configurational stability of an homogeneous specimen when the crack is slightly off the mid-plane as positioned, for example, in the fabrication of the specimen. As indicated by the sign of K_{II} near $y/b = 0$, a crack off the mid-plane will be driven further away from the mid-plane. The mid-plane crack is thus configurationally unstable. Crack path stability will be further discussed in Section VIII.

c. Exact Solutions for the Case H = h

Next consider the crack on the mid-plane and subjected to the general edge loads. The crack path selection is seldom an issue in the composite testing since cracks are usually confined to run along the fiber direction. The *exact* solution for ω can be obtained for this case by considering a special loading $M_1 = M_2 = M$ and all others being zero. By symmetry,
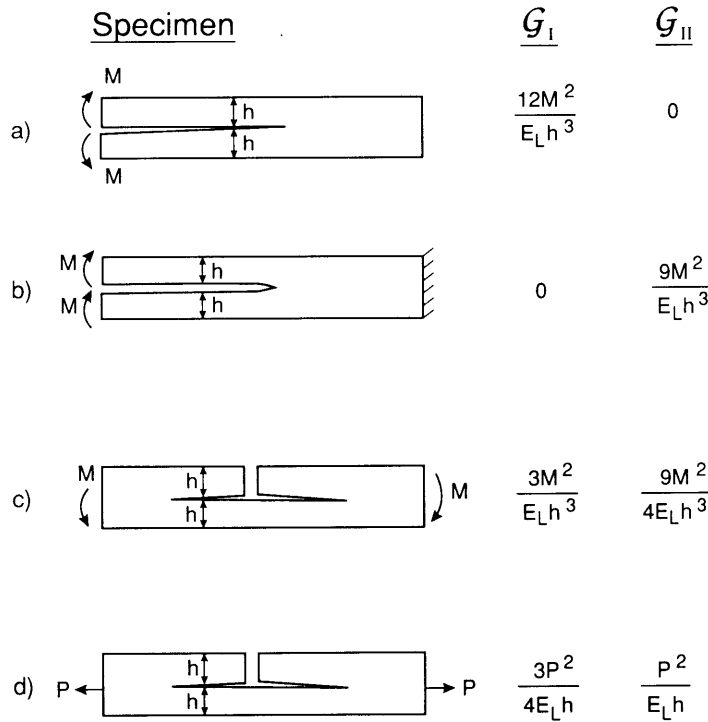
Specimen $\mathcal{G}_{\mathrm{I}}$ $\mathcal{G}_{\mathrm{II}}$

a) $\dfrac{12M^2}{E_L h^3}$ 0

b) 0 $\dfrac{9M^2}{E_L h^3}$

c) $\dfrac{3M^2}{E_L h^3}$ $\dfrac{9M^2}{4E_L h^3}$

d) $\dfrac{3P^2}{4E_L h}$ $\dfrac{P^2}{E_L h}$

FIG. 20. Several exact solutions: (a) a pure mode I specimen (double cantilever beam); (b) a pure mode II specimen (end-loaded split); (c) a mixed mode specimen (four-point bend); (d) a mixed mode specimen (crack-lap shear).

$K_{\mathrm{II}} = 0$, which, substituted into (3.7), gives $\omega = \cos^{-1}\sqrt{(3/7)} = 49.1°$. The full solution (3.7) can therefore be specialized to

$$K_{\mathrm{I}} = \sqrt{3}\,Ph^{-1/2} + 2\sqrt{3}\,Mh^{-3/2}, \qquad K_{\mathrm{II}} = 2Ph^{-1/2},$$

$$P = P_1 - \tfrac{1}{2}P_3 - \tfrac{3}{4}M_3/h, \qquad M = M_1 - \tfrac{1}{8}M_3. \tag{3.11}$$

Several useful edge loads are illustrated in Fig. 20. The mixed mode energy release rates listed are valid for an orthotropic material layer with a principal material axis coincident with the longitudinal direction. Geometries *a* and *b* are pure mode I and pure mode II, respectively. Geometries *c* and *d* are mixed mode.

d. Surface Layer Spalling

As the last example, consider a sub-surface crack in a semi-infinite plate ($\eta = 0$) as illustrated in Fig. 21. The problem was solved by Thouless *et al.*
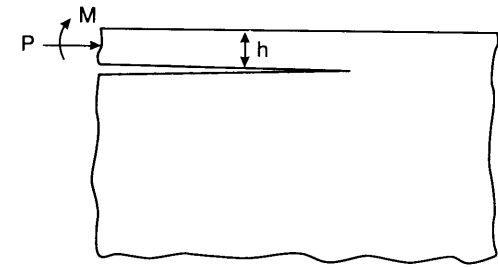
FIG. 21. Spalling of a surface layer due to edge loads.

(1987) in a study of impact spalling of ice sheets. The complete solution is

$$K_{\mathrm{I}} = \frac{1}{\sqrt{2}}[Ph^{-1/2}\cos\omega + 2\sqrt{3}\,Mh^{-3/2}\sin\omega],$$

$$K_{\mathrm{II}} = \frac{1}{\sqrt{2}}[Ph^{-1/2}\sin\omega - 2\sqrt{3}\,Mh^{-3/2}\cos\omega], \tag{3.12}$$

where $\omega = 52.07°$. Contrary to one's intuition, a significant amount of mode II component is caused by pure bending. The solution will be used in Section V to study decohesion of pre-tensioned films and thermal shock spalling.

2. A Homogeneous, Orthotropic Layer

The same geometry in Fig. 18 was also analyzed for orthotropic solids (Suo, 1990c). The layer lies in a principal material plane and the crack runs in principal axis-1 of the solid. The energy release rate expression (3.6) remains valid but the longitudinal tensile modulus $\bar{E}_L$ should be used, namely,

$$G_{\mathrm{I}} = \frac{1}{2\bar{E}_L}\left[\frac{P}{\sqrt{hU}}\cos\omega + \frac{M}{\sqrt{h^3 V}}\sin(\omega + \gamma)\right]^2, \tag{3.13a}$$

$$G_{\mathrm{II}} = \frac{1}{2\bar{E}_L}\left[\frac{P}{\sqrt{hU}}\sin\omega - \frac{M}{\sqrt{h^3 V}}\cos(\omega + \gamma)\right]^2, \tag{3.13b}$$

where P, M, U, V, and γ are given by (3.8) and (3.9). The quantity ω depends on η and ρ, but *not* λ. An integral equation method was used to determine ω, and the results indicate that the influence of ρ within its entire practical range is below one percent, so that (3.10) is an excellent approximation for orthotropic materials. When the stress intensity factors are

needed, the Irwin-type relation appropriate for orthotropic materials (2.16) must be used.

Notice that all the quantities in the brackets of (3.13) except for ω do not depend on material parameters. Further, ω may be approximated by (3.10), which is also independent of any material parameters. Consequently, the energy release rates of the two modes are essentially the same as their isotropic counterparts, except that the longitudinal tensile modulus should be used.

3. A Symmetric Tilt Strip

Imagine two identical layers cut from an orthotropic solid at an angle ϕ to principal material axis-1 (Fig. 22). The thickness of the two layers are equal, designated as h. The compliances s_{11}, s_{22}, s_{12}, and s_{66} are referred to the principal material axes. The two layers are bonded to form a symmetric tilt boundary, with a semi-infinite crack lying along the interface. The tilt angle is ϕ and the tilt axis, or the crack front, is one of the principal axes of the orthotropic solid. The general edge loads are applied.

The stress field around the crack tip is square root singular. The stress intensity factors are defined such that, asymptotically, traction on the grain boundary varies with the distance r from the crack tip according to

$$\sigma_y = (2\pi r)^{-1/2} K_{\mathrm{I}}, \qquad \tau_{xy} = (2\pi r)^{-1/2} K_{\mathrm{II}}. \qquad (3.14)$$

The Irwin-type relation for a crack on the symmetric tilt grain boundary is (Wang *et al.*, 1990)

$$G_{\mathrm{I}} = [b_{11}b_{22}(1 + \rho)/2]^{1/2}(\lambda^{-1/4}\cos^2\phi + \lambda^{1/4}\sin^2\phi)K_{\mathrm{I}}^2,$$
$$G_{\mathrm{II}} = [b_{11}b_{22}(1 + \rho)/2]^{1/2}(\lambda^{-1/4}\sin^2\phi + \lambda^{1/4}\cos^2\phi]K_{\mathrm{II}}^2, \qquad (3.15)$$

where the compliances are referred to the principal axes; see Section II.B.
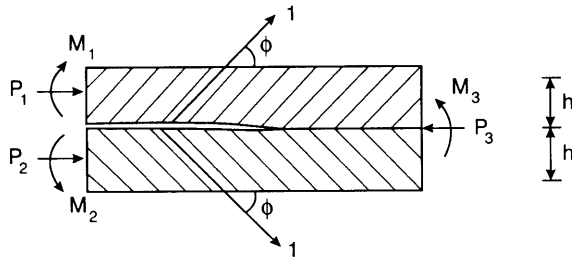

FIG. 22.   Two identical grains of an orthotropic crystal form a symmetric tilt boundary, with the principal crystal axis at an angle ϕ from the interface. The sample is under general edge loads.
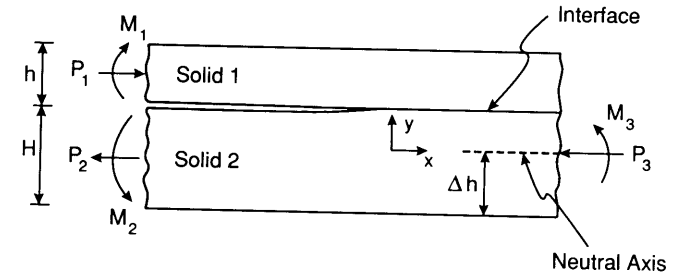
FIG. 23.   A bilayer with a half-plane interface crack. The neutral axis of the composite layer is indicated.

The analytical solution is found for the problem. Expressed in energy release rates, it is

$$G_{\mathrm{I}} = 3b_{11}^*(P + 2M/h)^2/h, \qquad G_{\mathrm{II}} = 4b_{11}^*P^2/h,$$
$$P = P_1 - \tfrac{1}{2}P_3 - \tfrac{3}{4}M_3/h, \qquad M = M_1 - \tfrac{1}{8}M_3. \qquad (3.16)$$

Here, b_{11}^* is the compliance in the x direction, which is related to the principal compliances by

$$b_{11}^* = (b_{11}b_{22})^{1/2}(\lambda^{1/2}\cos^4\phi + 2\rho\cos^2\phi\sin^2\phi + \lambda^{-1/2}\sin^4\phi). \qquad (3.17)$$

Notice that the energy release rates are identical to the corresponding homogeneous, isotropic results, except that the compliance must be reinterpreted.

4. An Interfacial Crack in a Bilayer

Figure 23 is a cross-section of an infinite bilayer with a half-plane crack on the interface. Each layer is taken to be homogeneous, isotropic, and linearly elastic. The uncracked interface is perfectly bonded with continuous displacements and tractions. The bilayer is loaded uniformly along the three edges with forces and moments per unit width. The problem has been studied by Suo and Hutchinson (1990), and the numerical solution has been presented in the entire parameter range. The generality of the edge loads allows the solution to be used to model a variety of delamination processes. A special loading case (a splitting cantilever bilayer) is discussed in Section II.C.4. The solution will be used to calibrate interfacial fracture specimens in Section IV.B.1, and to assess decohesion of pre-tensioned thin films in Section V.D. Focus here is on the presentation of the elasticity solution.

Far ahead of the crack tip the bilayer may be regarded as a composite beam. The neutral axis lies a distance $h\Delta$ above the bottom of the beam, with Δ being

$$\Delta = \frac{1 + 2\Sigma\eta + \Sigma\eta^2}{2\eta(1 + \Sigma\eta)}, \qquad (3.18)$$

where

$$\Sigma \equiv \frac{\bar{E}_1}{\bar{E}_2} = \frac{1 + \alpha}{1 - \alpha}, \qquad \eta = \frac{h}{H}. \qquad (3.19)$$

The composite layer is in a state of pure stretch combined with pure bending. The only nonzero in-plane stress component is σ_x. The corresponding strain is linear with the distance from the neutral axis, y, according to

$$\varepsilon_x = -\frac{1}{\bar{E}_2}\left(\frac{P_3}{hA} + \frac{M_3}{h^3 I}y\right). \qquad (3.20)$$

The dimensionless cross-section A and moment of inertia I are

$$A = \frac{1}{\eta} + \Sigma, \qquad I = \Sigma\left[\left(\Delta - \frac{1}{\eta}\right)^2 - \left(\Delta - \frac{1}{\eta}\right) + \frac{1}{3}\right] + \frac{\Delta}{\eta}\left(\Delta - \frac{1}{\eta}\right) + \frac{1}{3\eta^3}. \qquad (3.21)$$

The energy release rate can be calculated in close form:

$$G = \frac{1}{2\bar{E}_1}\left(\frac{P_1^2}{h} + 12\frac{M_1^2}{h^3}\right) + \frac{1}{2\bar{E}_2}\left(\frac{P_2^2}{H} + 12\frac{M_2^2}{H^3} - \frac{P_3^2}{Ah} - \frac{M_3^2}{Ih^3}\right). \qquad (3.22)$$

The energy release rate specifies the magnitude of the near-tip singularity but does not specify the mode mixity. The information is completed by the complex stress intensity factor K, which, to be consistent with linearity, dimensionality and the Irwin-type relation (2.29), takes the form

$$K = h^{-i\varepsilon}\left(\frac{1 - a}{1 - \beta^2}\right)^{1/2}\left(\frac{P}{\sqrt{2hU}} - ie^{i\gamma}\frac{M}{\sqrt{2h^3 V}}\right)e^{i\omega}, \qquad (3.23)$$

where $i = \sqrt{-1}$, and P and M are linear combinations of the edge loads:

$$P = P_1 - C_1 P_3 - C_2 M_3/h, \qquad M = M_1 - C_3 M_3. \qquad (3.24)$$

The geometric factors are given by

$$C_1 = \frac{\Sigma}{A}, \qquad C_2 = \frac{\Sigma}{I}\left(\frac{1}{\eta} + \frac{1}{2} - \Delta\right), \qquad C_3 = \frac{\Sigma}{12I}, \qquad (3.25)$$
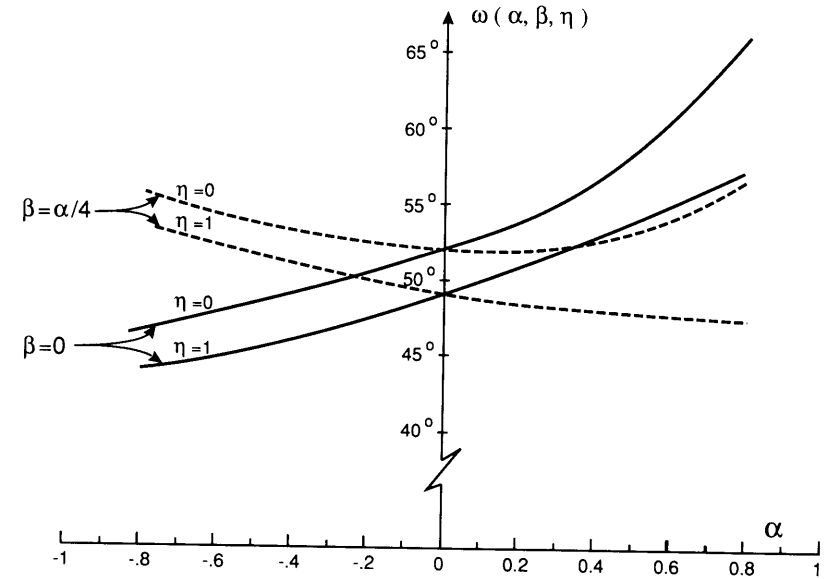
FIG. 24. Calculated values of the function $\omega(\alpha, \beta, \eta)$, which appeared in Eq. (3.23).

and by

$$\frac{1}{U} = 1 + \Sigma\eta(4 + 6\eta + 3\eta^2), \qquad \frac{1}{V} = 12(1 + \Sigma\eta^3), \qquad \frac{\sin\gamma}{\sqrt{UV}} = 6\Sigma\eta^2(1 + \eta). \qquad (3.26)$$

All these formulae are derived from the classical beam theory.

The angle ω is a function of the Dundurs' parameters α, β and relative height η. This function was determined by solving the elasticity problem numerically; the computed values are plotted in Fig. 24, and an extensive tabulation can be found in Suo and Hutchinson (1990).

5. A Substrate Crack in a Bilayer

Depicted in Fig. 25 is an infinite bilayer with a semi-infinite crack parallel to the interface. Each layer is isotropic and homogeneous. There are two length ratios: $\zeta_1 = H_1/h$ and $\zeta = H/h$. The problem was solved by Suo and Hutchinson (1989b) in the context of substrate spalling of a residual stressed thin film. The details of the application can be found in Section V.C.2, and here we will focus on the solution of the elasticity problem.

Of the three edges, one is a homogeneous beam and the other two are composite beams. The positions of neutral axes for the two composite
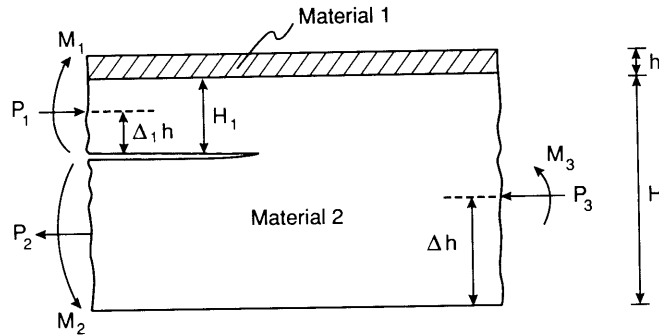
FIG. 25. A bilayer with a crack off the interface. The neutral axes for the two composite layers are indicated.

beams are given by

$$\Delta = \frac{\xi^2 + \Sigma\xi + \Sigma}{2(\xi + \Sigma)}, \qquad \Delta_1 = \frac{\xi_1^2 + \Sigma\xi_1 + \Sigma}{2(\xi_1 + \Sigma)}. \qquad (3.27)$$

The three beams may be described by a linear variation like (3.20). The effective cross-section and moment of inertia of the two composite beams are given by

$$A = \xi + \Sigma, \qquad I = \Sigma[(\Delta - \xi)^2 - (\Delta - \xi) + 1/3]$$
$$+ \Delta\xi(\Delta - \xi) + \xi^3/3,$$
$$A_1 = \xi_1 + \Sigma, \qquad I_1 = \Sigma[(\Delta_1 - \xi_1)^2 - (\Delta_1 - \xi_1) + 1/3]$$
$$+ \Delta_1\xi_1(\Delta_1 - \xi_1) + \xi_1^3/3. \qquad (3.28)$$

The energy release rate can be calculated in closed form:

$$G = \frac{1}{2\bar{E}_2}\left[\frac{P_1^2}{hA_1} + \frac{M_1^2}{h^3 I_1} + \frac{P_2^2}{h(\xi - \xi_1)} + \frac{12M_2^2}{h^3(\xi - \xi_1)^3} - \frac{P_3^2}{hA} - \frac{M_3^2}{h^3 I}\right]. \qquad (3.29)$$

The stress intensity factors are

$$K_I = \frac{P}{\sqrt{2hU}}\cos\omega + \frac{M}{\sqrt{2h^3 V}}\sin(\omega + \gamma),$$

$$K_{II} = \frac{P}{\sqrt{2hU}}\sin\omega - \frac{M}{\sqrt{2h^3 V}}\cos(\omega + \gamma), \qquad (3.30)$$

where P and M are linear combinations of edge loads:

$$P = P_1 - C_1 P_3 - C_2 M_3/h, \qquad M = M_1 - C_3 M_3,$$

$$C_1 = \frac{A_1}{A}, \qquad C_2 = \frac{A_1}{I}[(\xi - \Delta) - (\xi_1 - \Delta_1)], \qquad C_3 = \frac{I_1}{I}. \qquad (3.31)$$

and the geometric factors are

$$\frac{1}{U} = \frac{1}{A_1} + \frac{1}{\xi - \xi_1} + 12\frac{[\Delta_1 + (\xi - \xi_1)/2]^2}{(\xi - \xi_1)^3}, \qquad \frac{1}{V} = \frac{1}{I_1} + \frac{12}{(\xi - \xi_1)^3},$$

$$\frac{\sin\gamma}{\sqrt{UV}} = 12\frac{\Delta_1 + (\xi - \xi_1)/2}{(\xi - \xi_1)^3}. \qquad (3.32)$$

The angle ω as a function of α, β, ξ, and ξ_1 is extracted from a numerical solution, and is tabulated in Suo and Hutchinson (1989b).

C. A Bilayer Held between Rigid Grips

Figure 26 shows a bilayer with thickness h and H constrained between grips. Each layer is taken to be isotropic. The constraint is assumed to be perfectly rigid so that no separation nor sliding take place between the bilayer and grips. Both layers may be subject to residual stress in the layer direction, but it will not affect the singular field, and will therefore be ignored. An interface crack is driven by the relative *translation*, U and V, of the two grips. The problem of a homogeneous layer with a crack running on the mid-plane, i.e., $h = H$, has been solved analytically (Rice, 1968). A gripped epoxy/glass bilayer has recently been used by Liechti and Chai (1990b) to study mixed mode interfacial fracture resistance; see also Section II.C.4. The specimen calibration for a wide range of bimaterials are described in the following.

The debonded layers far behind the crack tip are stress-free, while the bonded layer far ahead is under a *uniform* strain state. An energetic accounting shows that

$$G = \frac{V^2}{2}\left(\frac{h}{\bar{E}_1} + \frac{H}{\bar{E}_2}\right)^{-1} + \frac{U^2}{2}\left(\frac{h}{\mu_1} + \frac{H}{\mu_2}\right)^{-1}, \qquad (3.33)$$

where $\bar{E} \equiv 2\mu(1 - v)/(1 - 2v)$ for plane strain, and $\bar{E} \equiv 2\mu/(1 - v)$ for plane stress.
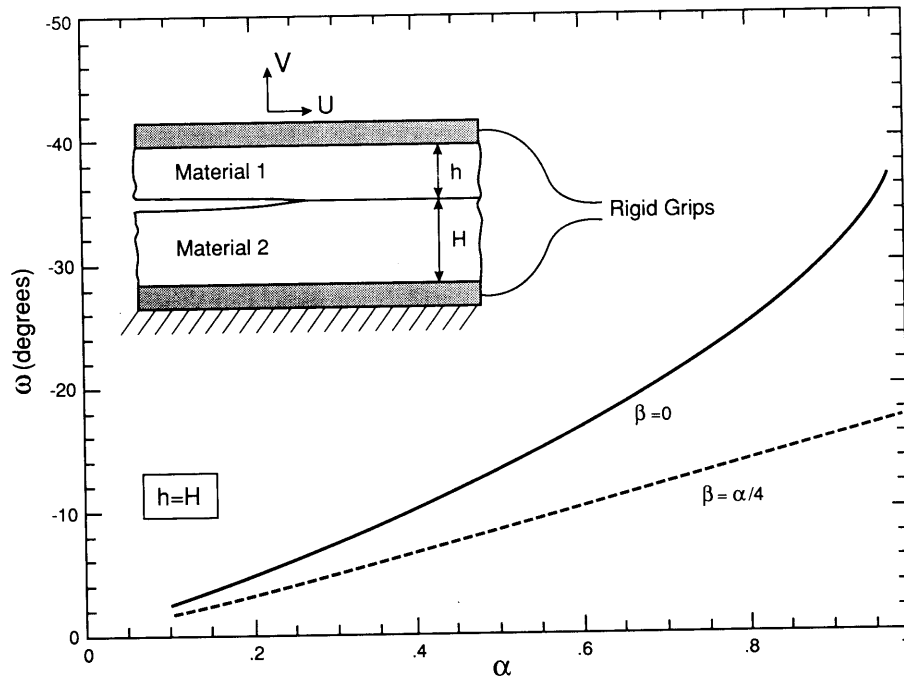
FIG. 26.   The insert shows a bilayer held between two rigid grips, and the crack is driven by the relative translation of the two grips. The numerical solution of the angle ω in Eq. (3.34) is plotted.

The mode mixity may be controlled by the relative proportion of the two grip translations. More precisely, the interfacial stress intensity factor is given by

$$K = h^{-i\varepsilon}e^{i\omega}\left(\frac{E_*}{1-\beta^2}\right)^{1/2}\left[\frac{V}{\sqrt{2}}\left(\frac{h}{\bar{E}_1}+\frac{H}{\bar{E}_2}\right)^{-1/2} + i\frac{U}{\sqrt{2}}\left(\frac{h}{\mu_1}+\frac{H}{\mu_2}\right)^{-1/2}\right].\quad (3.34)$$

This is derived using (3.33) and the Irwin-type relation (2.29). All quantities in the equation have been defined previously except for the angle ω, which is a function of μ_1/μ_2, ν_1, ν_2, and h/H. The problem contains displacement boundary conditions, so that in principle the two Dundurs' parameters are insufficient to characterize the bimaterial. However, it has been confirmed numerically (Beuth, 1991) that, once the Dundurs' parameters are fixed, the solution is almost independent of the third free variable. Finite element calculations are done for the case $H = h$ and the results are plotted in Fig. 26. Linear interpolation is recommended for values between $\beta = 0$ and $\beta = \alpha/4$.

D. SMALL-SCALE FEATURES

Scales play a fundamental role in the development of the fracture mechanics, as in any branch of continuum science. Classical examples are the notions of small-scale yielding, homogenization of composites or damage response. Here, we try to demonstrate, by a concrete example, how interface fracture mechanics may be applied at different scales. Consider two blocks of substrates joined by a thin adhesive layer. One is asked to study the toughness of the assembly. The problem may be tackled at two scales.

At a relatively macroscopic level, one may think of this as an interface fracture process between the two substrates, treating the adhesive as a small scale feature. At such a level, the two substrates explicitly enter the scheme of interface fracture, but the role of the adhesive, as well as damage processes in it, is contained in the macroscopically measured toughness. This evaluation process has been used in the adhesion community for years, except that the two substrates are usually identical, so that only the mixed mode fracture mechanics of homogeneous materials need be invoked. Obviously interface fracture mechanics is ideally suited to study the adhesion of different substrates.

At a more microscopic level, one may study the cracking along the interface between the adhesive and one of the substrates. Interface fracture mechanics can be used provided the crack stays along the interface and other damage processes are confined in a crack tip core region that is small compared with the thickness of the adhesive. These requirements can be realized if the interface is brittle enough. Mathematically, some well-defined small-scale features may be analyzed using a boundary layer approach. A few examples related to multilayers are collected in this section. Applications will be discussed in Section VIII.

1. *A Sub-interface Crack*

Consider a crack running near an interface (Fig. 27). The distance between the interface and crack, h, is small compared to all other in-plane lengths. The overall geometry, viewed at a scale much larger than h, can be regarded as an interface crack, so that the actual load and geometry can be represented by the complex stress intensity factor K appropriate for an interface crack. Near the crack tip, the stress field is that of a mixed mode crack in a homogeneous material, parameterized by K_I and K_{II}. Hutchinson *et al.* (1987) provided a connection between the two sets of the stress
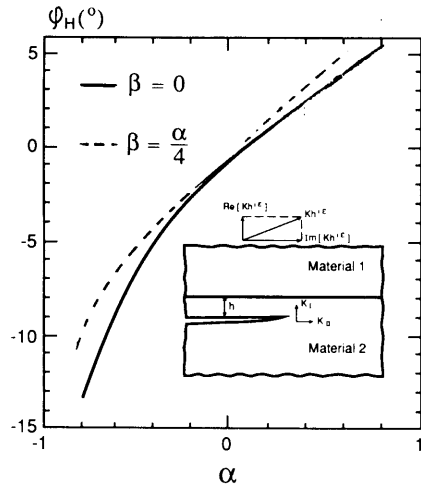
FIG. 27. A sub-interface crack. The spacing h is much smaller than the overall specimen dimension. The remote and local stress intensity factors are connected by Eq. (3.36), and the phase shift ϕ_H is plotted.

intensity factors, and used it to study the existence of mode I trajectory paralleling the interface.

The local and global energy release rates are identical, namely

$$G = \frac{1}{\bar{E}_2}(K_I^2 + K_{II}^2) = \frac{1 - \beta^2}{E_*}|K|^2. \qquad (3.35)$$

This relation gives the energy release rate at the crack tip, provided the remote K is known. Observe that the magnitudes of the two sets of stress intensity factors, $K_I + iK_{II}$ and K, are directly related by (3.35). They can differ only by a phase shift, designated as ϕ_H, so that

$$K_I + iK_{II} = \left(\frac{1 - \beta^2}{1 + \alpha}\right)^{1/2} Kh^{i\varepsilon}e^{i\phi_H}. \qquad (3.36)$$

The phase shift ϕ_H, ranging from $-15°$ to $5°$, is a function of the Dundurs' parameters. The numerical solution is plotted in Fig. 27, and a more extensive tabulation can be found in the original paper.

2. *An Interfacial Crack in a Sandwich*

Any homogeneous fracture specimen may be converted to measure interface toughness by sandwiching a *thin* layer of second material. The
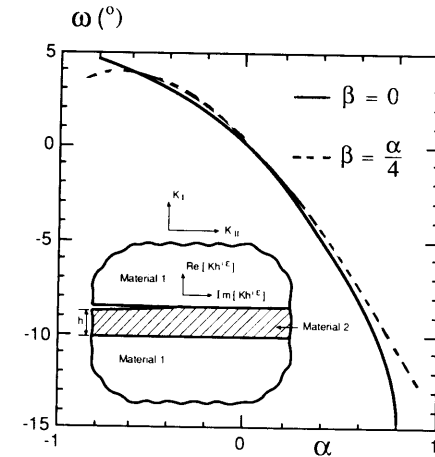
FIG. 28. An interface crack in a sandwich. The remote and local stress intensity factors are connected by Eq. (3.38), and the phase shift ω is plotted.

generic set-up is depicted in Fig. 28. An interlayer of material 2 is embedded in a homogeneous body of material 1, with a pre-existing crack lying along one of the interfaces (upper interface here). Each material is taken to be isotropic and linearly elastic. A solution described in the following, obtained by Suo and Hutchinson (1989a), provides the basis for a variety of sandwich specimens; an example, a Brazil-nut sandwich, will be discussed in Section IV.C.

The problem is asymptotic in that the reference homogeneous specimen is infinite and the crack is semi-infinite, as is appropriate when the layer thickness h is very small compared with all other in-plane length scales. The crack tip field of the homogeneous problem (without the layer) is prescribed as the far field in the asymptotic problem. Thus, the far field is characterized by K_I and K_{II}, induced by the loads on the reference homogeneous specimen. The interface crack tip field is characterized by the (complex) interfacial stress intensity factor K. A relation is developed in what follows that connects these two sets of stress intensity factors, allowing conversion of any homogeneous specimen to a sandwich without further calibration.

The global and local energy release rates are the same:

$$G = \frac{1}{\bar{E}_1}(K_I^2 + K_{II}^2) = \frac{1 - \beta^2}{E_*}|K|^2. \qquad (3.37)$$

Considerations similar to those of the previous subsection give

$$K = h^{-i\varepsilon}\left(\frac{1-\alpha}{1-\beta^2}\right)^{1/2}(K_\mathrm{I} + iK_\mathrm{II})e^{i\omega}. \qquad (3.38)$$

From numerical calculations, the angle shift ω, which is due exclusively to the moduli dissimilarity, ranges between $5°$ to $-15°$, depending on α and β. The solution is plotted in Fig. 28; other cases are tabulated in Suo and Hutchinson (1989a).

3. Parallel Debond

When a sandwich layer is under substantial residual compression, debond may take place along the *two* interfaces. The phenomenon was observed in preparing Al_2O_3—SiC—Al_2O_3 laminate (private communication with A. G. Evans). The laminate was diffusion bonded at an elevated temperature, but debonded into three layers in the cool-down. Parallel cracks under uniaxial loads have been observed in laminates with center notches or matrix cracks. The solution obtained by Suo (1990b) is given in the following.

It can be shown with the Eshelby cut-and-paste technique that, as far as the stress intensity is concerned, the residual compression is equivalent to a mechanical load of layer pull-out. Depicted in Fig. 29 is a slightly generalized situation in which an opening load represented by K_I^∞ is included, in addition to the pull-out stress σ. It is envisioned that the pull-out stress itself
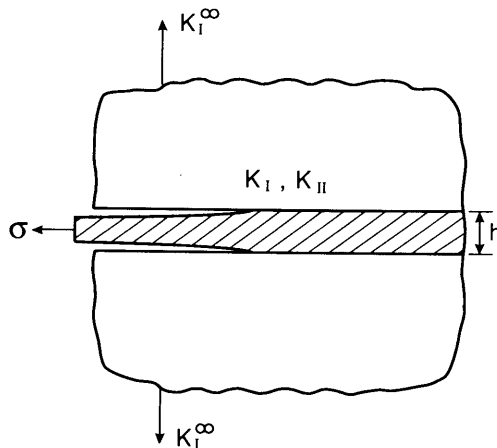
FIG. 29.   Parallel debond of a sandwich layer, driven by the pull-out stress σ and the remote opening load K_I^∞.

may not be high enough to trigger debonding, but the structure debonds with an additional remote mode-I load.

To gain insight into this setup, we ignore the moduli difference in this preliminary treatment. By an energetic argument, one obtains the energy release rate at each tip under combined loads σ and K_I^∞:

$$G = \frac{1}{\bar{E}}\left(\frac{K_\mathrm{I}^{\infty 2}}{2} + \frac{\sigma^2 h}{4}\right). \qquad (3.39)$$

Hence, the interfacial fracture energy can be inferred if one measures σ and the critical K_I^∞ that trigger the debond.

Recall the Irwin formula (2.5) is applicable for each crack tip. Comparing the two energy release-rate expressions, and keeping the linearity of the elasticity problem in mind, one obtains the local stress intensity factors

$$K_\mathrm{I} = \frac{1}{\sqrt{2}}K_\mathrm{I}^\infty \cos\phi + \frac{1}{2}\sigma\sqrt{h}\sin\phi,$$

$$K_\mathrm{II} = -\frac{1}{\sqrt{2}}K_\mathrm{I}^\infty \sin\phi + \frac{1}{2}\sigma\sqrt{h}\cos\phi. \qquad (3.40)$$

The angle ϕ has to be determined by solving the full elasticity problem. An integral equation approach was used and the solution was found to be $\phi \approx 17.5°$.

Consider the case when $K_\mathrm{I}^\infty = 0$. The above solution indicates that the pull-out stress induces a significant amount of crack face opening, along with the predominant sliding. By contrast, residual tension (equivalent to a push-in mechanical stress) induces a negative K_I, suggesting that debonding will be a pure mode-II sliding against friction. Therefore, parallel debonding will more likely take place for adhesives in residual compression than in tension, provided other conditions are the the same.

The solution can be generalized to orthotropic materials using the concept of orthotropy rescaling. Suppose the entire material is orthotropic and homogeneous. Two cracks run in the principal axis 1. Using orthotropy rescaling, (3.40) becomes

$$K_\mathrm{I} = \frac{1}{\sqrt{2}}K_\mathrm{I}^\infty \cos\phi + \frac{\lambda^{3/8}}{2\sqrt{n}}\sigma\sqrt{h}\sin\phi,$$

$$K_\mathrm{II} = -\frac{\lambda^{-1/4}}{\sqrt{2}}K_\mathrm{I}^\infty \sin\phi + \frac{\lambda^{1/8}}{2\sqrt{n}}\sigma\sqrt{h}\cos\phi, \qquad (3.41)$$

TABLE 1

$\phi(\rho)$ (in Degrees) for Parallel Debond

ρ	-0.5	-0.3	-0.1	0.1	0.3	0.5	0.7	0.9
ϕ	22.9	21.6	20.6	19.9	19.2	18.7	18.2	17.8
ρ	1	2	3	4	5	6	7	8
ϕ	17.5	15.9	14.9	14.1	13.4	12.9	12.5	12.1

where $n = [(1 + \rho)/2]^{1/2}$. Now the phase shift ϕ depends on ρ. An integral equation is solved numerically, and the results are listed in Table 1.

IV. Laminate Fracture Test

Interlaminar fracture resistance of multilayers is usually measured using beam-type specimens. Fracture mode mixity, ranging from opening, mixed mode, to shearing, can be controlled by the loading configuration. A catalog of such specimens is presented, for application to both orthotropic materials and bimaterials. Most of these specimens have been used by the composite community for decades. Yet rigorous, general calibrations are available only recently. Delamination resistance can be enhanced by a variety of bridging mechanisms. A prevailing issue is that the bridging-zone size is usually several times the lamina thickness, so that delamination resistance is no longer a material property independent of specimen size and geometry. The implications will be studied using the Dugdale model.

A. DELAMINATION BEAMS

Beam-type fracture specimens are most frequently used for composites, adhesive joints, and other laminated materials. Small scale features such as fiber/matrix inhomogeneity are typically not explicitly taken into account. For example, homogenized elastic constants are used for composites. The Irwin–Kies compliance calibration is still in use for lack of elasticity solutions. Empirical calibrations obtained this way should be valid only for the materials being tested, since they typically depend on elastic constants. Finite element calibration has been used by many authors, and previous literature on the subject may be found in a volume edited by Friedrich (1989). Guided by an orthotropy rescaling concept, Suo (1990c) and Bao *et al.* (1990)

have analyzed many commonly used specimens, using either integral equations or finite elements. Included were notched bars loaded in various configurations, delamination beams, and hybrid sandwiches. The work of Suo (1990c) has been summarized in Section III.B.2, which is applicable for unidirectional composites under steady-state loading configurations. Several other delamination beams analyzed by Bao *et al.* (1990) will be described in the following.

1. Double Cantiler Beams

Illustrated in Fig. 30 is a double cantilever beam made of a unidirectional composite with fibers along the beam axis. The specimen is pure mode I, and energy release rate is

$$G = 12 \frac{(Pa)^2}{h^3 \bar{E}_L} (1 + Y\lambda^{-1/4}h/a)^2, \qquad (4.1)$$

where P is force per unit width, $2h$ beam thickness, a crack length, $\bar{E}_L \equiv 1/b_{11}$ is the effective Young's modulus in fiber direction, and λ and ρ are dimensionless orthotropic parameters. These material constants are defined in Section II.B. The dimensionless factor Y is approximated by

$$Y(\rho) = 0.677 + 0.149(\rho - 1) - 0.013(\rho - 1)^2. \qquad (4.2)$$

These formulae are valid for both plane stress and plane strain, for generally orthotropic materials within the entire practical range, $\lambda^{1/4}a/h > 1$ and $0 < \rho < 5$, and the error is within 1%. In particular, the preceding result is valid for isotropic materials when $\rho = \lambda = 1$.

This calibration is obtained using finite elements, together with several analytic considerations. The first term in the bracket in (4.1) reproduces the exact elasticity asymptote as $a/h \to \infty$, which may be obtained from the

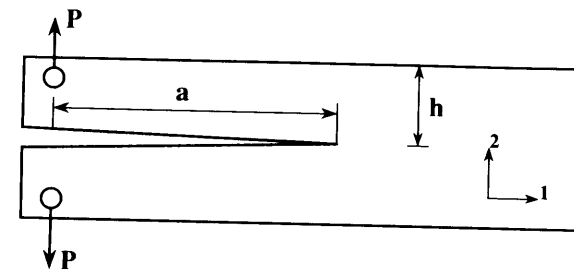Fig. 30.   A mode I delamination specimen (double cantilever beam (DCB)).

End-Loaded-Split (ELS)

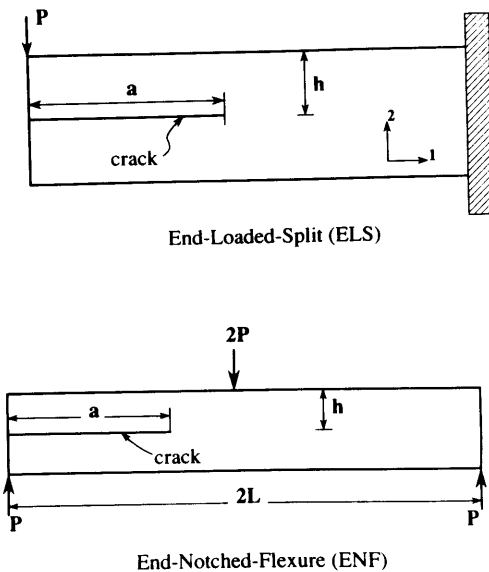
End-Notched-Flexure (ENF)

FIG. 31. Two mode II delamination beams: (a) end-loaded split (ELS); (b) end-notched flexure (ENF).

classical beam theory. The second term in the bracket is the first order correction in h/a. As a consequence of the orthotropy rescaling, the consistent correction, including the elastic constants λ and ρ, is of the form (4.1), where Y depends on ρ only; see Suo et al. (1990b).

2. End-Loaded Split and End-Notched Flexure

Figure 31 shows two designs of mode II specimens. The calibration for ELS is

$$G = \frac{9(Pa)^2}{4h^3\bar{E}_L}(1 + Y\lambda^{-1/4}h/a)^2, \tag{4.3}$$

$$Y(\rho) = 0.206 + 0.078(\rho - 1) - 0.008(\rho - 1)^2. \tag{4.4}$$

All comments in the last subsection are valid here. To a high accuracy, the calibration for ENF is identical to the preceding, as independently confirmed by He and Evans (1990b).

3. Steady-State Mixed Mode Specimens

It is relatively difficult to design a mixed mode fracture specimen having a fixed mode mixity as the crack grows. Two such specimens are depicted in

Fig. 20. As the crack length exceeds about three times the notch depth h, both the driving force and mode mixity become essentially independent of the delamination length. The calibrations are listed in the figure. It is not necessary to measure crack size in a fracture test with such steady-state specimens. Steady-state delamination beams of other edge load combinations and/or of dissimilar arm thicknesses can be specialized from the general solution in Section III.B.2.

4. Other Mixed Mode Delamination Beams

Recall that stress intensity factors are linearly additive. One may use the basic solutions presented in the preceding to obtain calibrations for other specimens. Two examples are illustrated in Figs. 32 and 33. The specimen in Fig. 32a is mixed mode, and can be solved by a superposition of DCB and ELS. Note that both the magnitude of G and the mode mixity change as the crack advances. The three-point bend in Fig. 33 is a superposition of the four-point flexure specimen and the specimen in Fig. 32a.
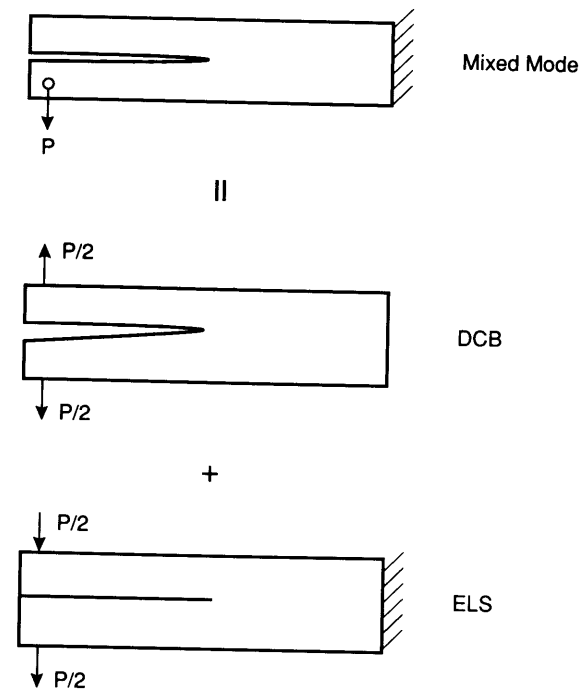

FIG. 32. The mixed mode end-notched split is the superposition of the DCB and ELS.
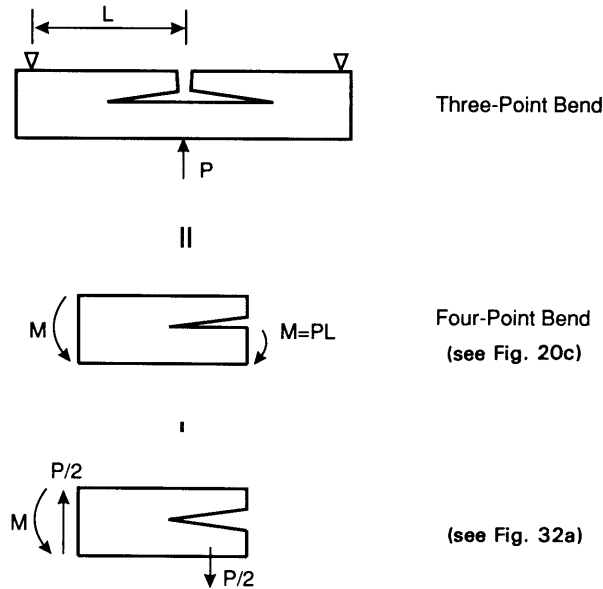
Three-Point Bend

$\parallel$

$M \Big($ ⬚ $\Big) M = PL$

Four-Point Bend

(see Fig. 20c)

$\mathbf{I}$

$M \Big($ ⬚ $\Big)$

(see Fig. 32a)

Fig. 33.   A superposition scheme for three-point shear.

B. INTERFACIAL FRACTURE SPECIMENS

As discussed in Section II.C, the fracture resistance of an interface generally depends on the mode mixity. Thus, a toughness curve, $\Gamma(\hat{\psi})$, must be determined experimentally to fully characterize a given interface. Two strategies have been used in practice to vary the mode mixity: multiloads or multispecimens. The bilayer held between rigid grips discussed in Section III.C.4 and Section III.C is an example of multiload specimens. In this section, several other specimens are described.

1. *Four-Point Flexure of a Bilayer*

Figure 34 shows a specimen consisting of roughly the same amount of opening and sliding. The specimen was first analyzed by Charalambides *et al.* (1989), and is a special edge load combination of the general problem in Section III.B.4. Evans and coworkers at the University of California, Santa Barbara have used this configuration to test bimaterial interfaces (Cao and Evans, 1989), ceramic composite laminates (Sbaizero *et al.*, 1990), metallic adhesive joints (Reimanis and Evans, 1990), and thin films (Hu and Evans,
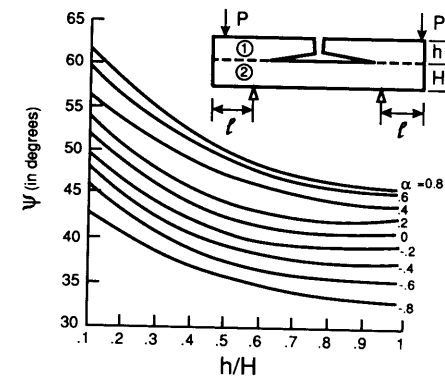
Fig. 34.   The insert shows the UCSB four-point flexure of a bilayer. The mode mixity is plotted.

1989). The setups have been collectively referred to as the UCSB four-point flexure specimens.

When the crack exceeds a few times the thickness of the notched layer, h, it can be considered as semi-infinite. The energy release rate is obtained in closed form:

$$G = \frac{M^2}{\bar{E}_2 h^3}\left(6\eta^3 - \frac{1}{2I}\right),\qquad(4.5)$$

where $M = Pl$ is the moment per unit width, and the dimensionless moment of inertia I is given in (3.21). The loading phase ψ is defined by (2.45) with h as the reference length, such that the stress intensity factor is

$$K = |K|h^{-i\varepsilon}\exp(i\psi).\qquad(4.6)$$

It is plotted in Fig. 34 with $\beta = 0$.

Charalambides *et al.* (1990) carried out a thorough analysis of several complexities of the four-point flexure. One complication concerns the residual stress in bilayers induced in fabrication, which would affect both energy release rate and loading phase. Observe that the complex stress intensity factors due to the bending moment and residual stress can be linearly superimposed, and both are the special cases of the general problem in Section III.B.4. The latter case will also be treated explicitly in Section V.D.

2. *Edge-Notched Bend*

A predominantly opening specimen is depicted in Fig. 35. Without loss of generality, one can choose material 1 to be relatively rigid, so that the
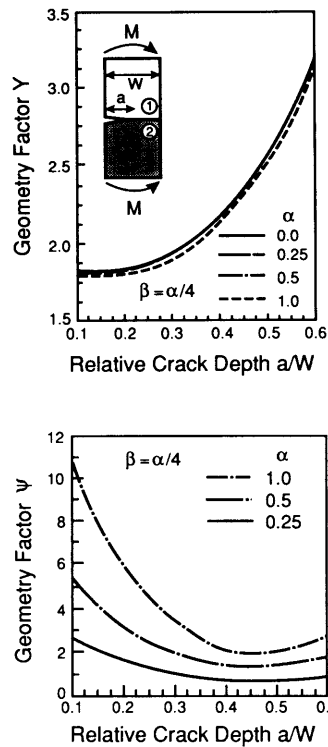
FIG. 35.   Calibration of the edge-notched bend of a bimaterial bar.

Dundurs parameter satisfies $\alpha > 0$. With ψ defined by (2.45) with $l = a$, the stress intensity factor is calibrated by

$$K = YT\sqrt{a}\,a^{-i\varepsilon}e^{i\psi}. \tag{4.7}$$

Here, T is the nominal bending stress, related to the moment per unit width M by

$$T = 6M/W^2, \tag{4.8}$$

and Y is the real, positive calibration factor.

Both Y and ψ are dimensionless functions of α, β, and a/W. The finite element results are plotted in Fig. 35 (O'Dowd *et al.*, 1990). Observe that the magnitude factor Y is nearly independent of elastic mismatch. The loading phase ψ varies between 0° to 10°, depending on the elastic mismatch.

3. *Edge-Notched Shear*

Calibration is also available for the specimen shown in Fig. 36 (O'Dowd *et al.*, 1990). The loading phase is controlled by the offset s/W. The stress intensity factor is

$$K = YT\sqrt{a}\,a^{-i\varepsilon}e^{i\psi}, \tag{4.9}$$

where ψ is again defined by (2.45) with $l = a$, and

$$T = \frac{(A - B)P}{(A + B)W}. \tag{4.10}$$

The dimensionless functions Y and ψ are plotted in Fig. 36.
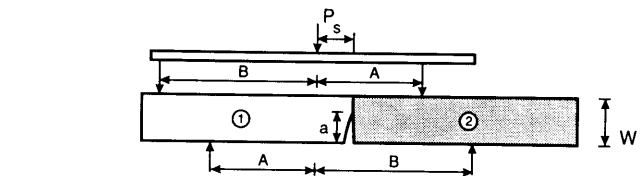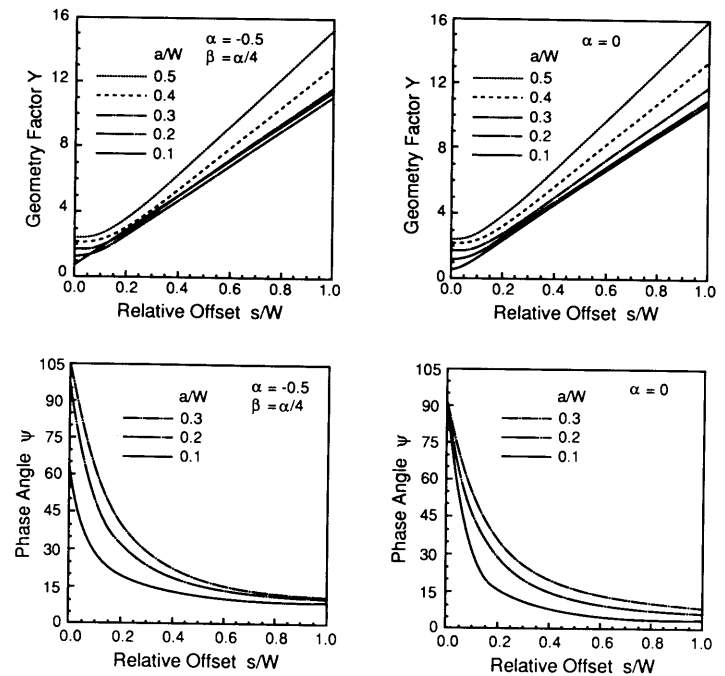

FIG. 36.   Calibration of the edge-notched shear of a bimaterial bar.

C. Brazil-Nut Sandwiches

Any homogeneous specimen can be converted to an interfacial specimen by sandwiching a thin layer of a second material between split halves of the specimen. The general setup is analyzed in Section III.D.2. As an example, here we sandwich the Brazil nut with a layer of second material, and a crack is left on one of the interfaces (Fig. 37). The specimen has been developed to determine interfacial toughness by Wang and Suo (1990).

A remarkable feature common to all thin-layer sandwiches is that the residual stress in the layer does *not* drive the crack, because the strain energy stored in the layer due to residual stress is not released in the process of cracking. Thus, one does not have to measure the residual stress to determine toughness. On the other hand, as discussed in Section VIII, excessive
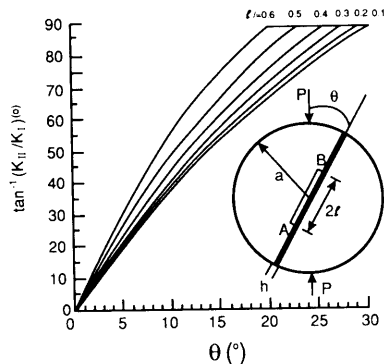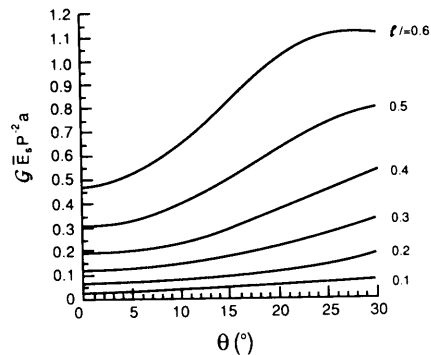

FIG. 37.   Driving force and mode mixity of the Brazil-nut sandwich.

residual stress may cause complications such as crack tunneling and kinking, so it should be avoided.

1. Homogeneous Brazil Nuts

A homogeneous Brazil nut is a disk of radius a, with a center crack of length $2l$ (as illustrated in Fig. 37 but without the interlayer), which has been used for mixed mode testing of brittle solids for years. The loading phase is controlled by the compression angle θ: It is mode I when $\theta = 0°$, and mode II when $\theta \approx 25°$. The stress intensity factors are

$$K_I = f_I P a^{-1/2}, \qquad K_{II} = \pm f_{II} P a^{-1/2}, \tag{4.11}$$

where the plus sign is for tip A, and minus for B. The nondimensional calibration factors f_I and f_{II} are functions of θ and l/a, and available in fitting polynomial forms in Atkinson *et al.* (1982).

Using the Irwin relation (2.5), the energy release rate is

$$G = (f_I^2 + f_{II}^2)P^2/a\bar{E}_S, \tag{4.12}$$

where $\bar{E}_S$ is plane strain tensile modulus for the substrate. The loading phases at tips A and B are

$$\tan^{-1}(K_{II}/K_I) = \pm\tan^{-1}(f_{II}/f_I), \tag{4.13}$$

respectively. Equations (4.12) and (4.13) are plotted in Fig. 37.

2. Sandwiched Brazil Nuts

A sandwich is made by bonding two halves with a thin layer of a second material. Nonsticking mask is supplied on the prospective crack surface prior to bonding. When the layer thickness h is much smaller than other in-plane macroscopic lengths, the energy release rate can still be calculated from (4.12). This is true because of the conservation of the J-integral, and because the perturbation due to the thin layer is vanishingly small in the far field.

The mode mixity $\hat{\psi}$, defined by (2.45) with $\hat{l}$ as the reference length, is shifted from that for the homogeneous specimen, in accordance with

$$\hat{\psi} = \pm\tan^{-1}(f_{II}/f_I) + \omega + \varepsilon \ln(\hat{l}/h). \tag{4.14}$$

Here, ω, plotted in Fig. 28, is the shift due to elastic mismatch (3.38), and the last term is the shift due to the oscillation index ε, (2.49).

D. DELAMINATION *R*-CURVES

1. *Large-Scale Bridging*

Over the last decade, it has become increasingly evident that the toughness of brittle materials can be enhanced by a variety of bridging mechanisms. The mechanics language that describes this is resistance curve behavior (*R*-curves): Toughness increases as crack grows. Attention here is focussed on the delamination of unidirectional or laminated composites, where cracks nominally propagate in planes parallel to fibers. A comparative literature study shows that for both polymer and ceramic matrix composites, bridging is usually due to intact fibers left behind the crack front, while the crack switches from one fiber–matrix interface to another as it propagates. Additional resistance for polymer matrix composites comes from damage in the form of voids, craze, or micro-cracks. Three-dimensional architecture of threading fibers may also give rise to substantial fracture resistance.

As the prerequisite for these bridging mechanisms, significant damage must accumulate ahead of the pre-cut tip as an additional energy dissipater. In laminates, for example, the length over which fibers bridge the crack is typically several times lamina thickness. The significance of an *R*-curve as a material property becomes ambiguous, since the *R*-curve now depends on specimen size and geometry. The intent of this section is to describe several generic features unique to delamination *R*-curves, as identified in Suo *et al.* (1990a); references on the subject can be found in the original paper.

2. *Essential Features of Delamination R-curves*

Consider a beam with a pre-cut, loaded at the edges by moments (Fig. 38). The damage zone size *L* can be comparable to or larger than beam thickness *h*, but the beam and pre-cut are much longer, so that the geometry is fully
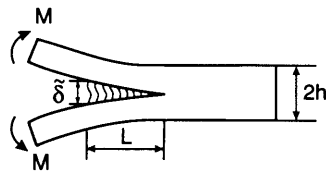
FIG. 38. A mode I delamination beam, with a damage zone as an additional energy dissipater. The geometry is specified by *L*/*h*.
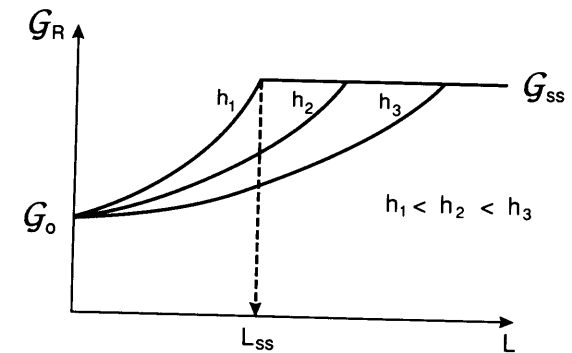
FIG. 39. Two generic features of delamination *R*-curves. The plateau G_{ss} is independent of the beam thickness *h*. The steady-state damage zone L_{ss} size increases with *h*.

characterized by the ratio *L*/*h*. The material is assumed to be elastically isotropic and homogeneous, and plane strain conditions prevail. The *nominal*, or *global*, energy release rate is defined as the *J*-integral over the external boundary as given by Rice (1968):

$$G = CM^2, \qquad C = 12(1 - v^2)/Eh^3. \qquad (4.15)$$

Here, *M* is the applied moment per unit width, *C* the beam compliance, 2*h* the thickness, *E* the Young's modulus, and *v* the Poisson's ratio. The specimen has a *steady-state calibration*: The global energy release rate does not depend on crack size, nor does it depend on any information of the damage zone (size, constitutive law, etc.).

Phenomenological delamination *R*-curve behaviors are shown schematically in Fig. 39. First, focus on a *R*-curve measured using a beam of a given thickness, say, h_1 in the figure. The specimen can sustain the increasing moment, without appreciable damage at the pre-cut front, up to a critical point corresponding to G_0. Subsequently, the damage zone size *L* increases with the applied moment, leading to an increasing curve of resistance G_R. The damage zone may attain a steady-state: It maintains a self-similar opening profile and a constant length L_{ss}, translating in the beam, leaving behind the crack faces free of traction. Correspondingly, a plateau G_{ss} would appear on the *R*-curve.

To proceed further, the Dugdale (1960) model is invoked, which, in its generalized form, simulates the homogenized damage reponse with an array of continuously distributed, nonlinear springs. Specifically, at each point in the damage strip, the closure traction σ depends locally on the separation δ

according to

$$\sigma = \sigma(\delta). \qquad (4.16)$$

The functional form is related to the nature of damage, but is assumed to be *identical* for every point in the damage strip, and *independent* of the specimen geometry. A maximum separation δ_0 is specified, beyond which the closure traction vanishes. The spring laws may be measured or modeled using simplified systems. They may also be inferred from experimental *R*-curves, as will be discussed.

For an arbitrary spring law, the following energy balance is due to the *J*-integral conservation (Rice, 1968):

$$G = G_0 + \int_0^{\tilde{\delta}} \sigma(\delta)\, d\delta, \qquad (4.17)$$

where $\tilde{\delta}$, referred to as the *end-opening* of the damage zone, is the separation at the pre-cut tip. Here and later, we will not distinguish the driving force G and the resistance G_R, as they can be judged from the context. The two energy release rates G and G_0 will be referred to as *global* and *local*, respectively. The global energy release rate represents the supplied energy, which is related to the applied moment via (4.15); the local one is the energy dissipated at the damage front. The difference given by (4.17) is the energy to create the damage.

The steady-state resistance G_{ss} is attained when the end-opening reaches the critical separation, $\tilde{\delta} = \delta_0$. Thus, from (4.17), G_{ss} equals the sum of G_0 and the area under the spring law. The physical significance is that the plateau G_{ss} does not depend on the beam thickness, and is therefore a property for a given composite laminate. However, it is not yet clear how long the damage strip will be before the steady state is attained. The steady-state damage-zone size L_{ss} indicates the "quality" of a bridging mechanism: Toughness gained from too long a damage zone may not be useful in practice. Qualitatively, a thicker, stiffer, beam is more constrained for deflection, and thus exhibits larger L_{ss}. These essential features of the delamination *R*-curves are indicated in Fig. 39.

Equation (4.17) suggests a way to determine the damage response. By continuously measuring the end-opening $\tilde{\delta}$, and by using the experimentally determined *R*-curve, the spring law can be inferred by differentiating (4.17):

$$\sigma(\tilde{\delta}) = \partial G_R / \partial \tilde{\delta}. \qquad (4.18)$$

The intrinsic resistance G_0 is assumed to be independent of the damage

accumulation. This simple method, which bypasses the complexities of large-scale bridging, is one of the advantages of specimens with steady-state calibrations. Large-scale bridging may be used as an experimental probe to study localized (planar) damage response such as polymer craze and interface separation, as uniform separation over a sample may be difficult to accomplish in reality because of the instabilities triggered by inhomogeneities or edge effects.

3. Rigid Plastic Damage Response

To gain some quantitative feel, consider a two-parameter damage response: The closure traction is σ_0 when $\delta < \delta_0$, and vanishes when $\delta > \delta_0$. The steady-state toughness is

$$G_{ss} = G_0 + \sigma_0 \delta_0. \qquad (4.19)$$

The end-opening and crack tip stress intensity factor are given by

$$\tilde{\delta} = aL^2 \sqrt{CG} - \frac{a^2}{4} L^4 C\sigma_0, \qquad (4.20a)$$

$$\sqrt{G} = \sqrt{G_0} + \frac{a}{2} \sqrt{C} L^2 \sigma_0, \qquad (4.20b)$$

where the dimensionless number a depends on L/h only, and the finite element results are listed in Table 2.

The *R*-curve defined by Eq. (4.20b) is plotted on Fig. 40 in a dimensionless form. The plateau G_{ss} in (4.19) should be a horizontal line independent of h and L (not shown in the figure). From material characterization point of view, an inverse problem is of much more interest: how to infer the model parameters from a given experimental *R*-curve. The quantities G_0, G_{ss}, and L_{ss} can usually be read off from the *R*-curve. Using these, the model parameters σ_0 and δ_0 can be inferred from (4.20).

A family of damage responses including softening and hardening have been analyzed in Suo *et al.* (1990a). The effect of mode mixity has also been discussed. A parallel experimental investigation has been carried out by

TABLE 2

$a(L/h)$

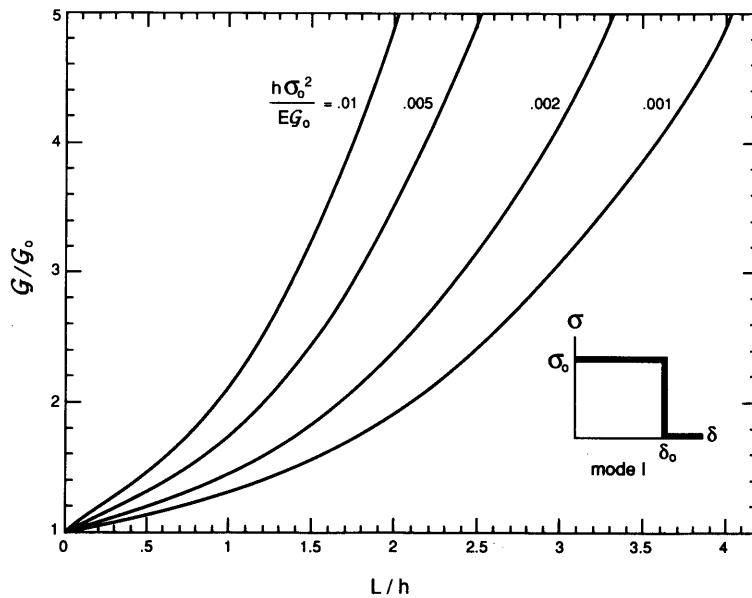| L/h	0.5	1.0	1.5	2.0	3.0	3.5	4.0	10.0	∞
a	4.89	2.60	2.01	1.74	1.58	1.48	1.35	1.14	1.00

FIG. 40. Dimensionless *R*-curves predicted using the rigid plastic damage response (mode I).

Spearing and Evans (1990) with a unidirectional ceramic composite. The experimental data and the model show very similar behavior, suggesting that the model incorporates the controlling features of the toughening mechanism.

V. Cracking of Pre-tensioned Films

Thin films of metals, ceramics and polymers, are typically subject to appreciable residual stress, which for ceramic systems can be on the order of a giga-pascal. Such stress can cause cracking of the films. Films under residual tension and compression will be considered in this and the next sections, respectively. In this section, commonly observed fracture patterns in pre-tensioned films are first reviewed, together with a discussion of the governing parameters. These crack patterns are then analyzed in subsequent subsections, with cracking in films, substrates, and along interfaces treated independently. The values of a nondimensional driving force *Z* will be documented to assist the practitioners of the field. The last subsection presents a speculative analysis of thermal shock spalling.
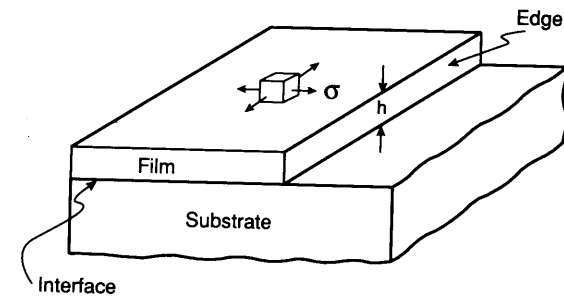

FIG. 41. A pre-tensioned film is deposited on a substrate.

A. CONTROLLING QUANTITIES AND FAILURE MODES

Illustrated in Fig. 41 is a film of thickness *h* on a substrate. Both materials are taken to be isotropic and linearly elastic, with elastic moduli and thermal expansion coefficients (E_f, ν_f, α_f) and (E_s, ν_s, α_s), respectively. Elasticity mismatch may be characterized by the two Dundurs parameters α and β defined in (2.21); $\alpha > 0$ when film is stiffer than substrate. A crack will grow as the driving force *G* attains the fracture resistances $\Gamma_f, \Gamma_s, \Gamma_i$, depending on whether the crack is propagating in the film, substrate, or along the interface. The mode I fracture resistance is usually appropriate for films and substrates, but mixed mode resistance must be used for interfaces.

1. *Driving Force Number and Critical Film Thickness*

To help visualize the cracking progression, the residual stress is assumed to be due entirely to thermal mismatch. However, with proper interpretation, most of our results would be valid for stress due to other sources. The film–substrate is stress-free at a high temperature T_0. Upon cooling to the room temperature T_r, the contraction strains in the film and substrate, were they unbonded, would differ by $(\alpha_f - \alpha_s)(T_0 - T_r)$. A biaxial *misfit stress* is defined accordingly:

$$\sigma = (\alpha_f - \alpha_s)(T_0 - T_r)E_f/(1 - \nu_f). \qquad (5.1)$$

Notice $\sigma > 0$ when $\alpha_f > \alpha_s$. This stress is large: Typically, $E\alpha \cong 1$ MPa/K for most materials. For example, the stress would be of order 1 GPa if the temperature drops 1000 K (this is common in processing ceramic systems).
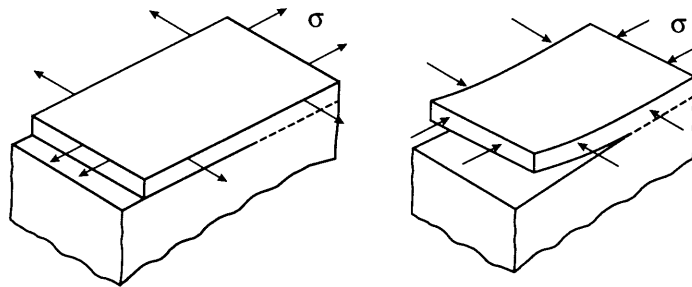
FIG. 42. An Eshelby-type superposition to treat a residually stressed film decohering from a substrate.

The thermal stress field can be evaluated by an Eshelby-type superposition. As an example, consider a thin film decohering from a substrate, driven by a biaxial misfit strain (Fig. 42). Problem (a) is trivial: the misfit strain is negated by a mechanical strain corresponding to the tensile stress σ; the film is under a uniform biaxial stress, and the substrate is stress-free. In problem (b), a pressure of magnitude σ is applied on the edge of the film, but no misfit strain is present. The superposition recovers the original problem, with misfit strain but without edge load. Since no stress singularity is present in (a), the crack driving force is entirely due to (b). The latter is a standard elasticity problem, which requires numerical analysis.

A unifying dimensionless number Z is defined such that the energy release rate for a crack is

$$G = Z\sigma^2 h/\bar{E}_f. \tag{5.2}$$

Note that the elastic strain energy stored in a unit area of the film is $(1 - \nu_f)\sigma^2 h/E_f$. The number Z is a dimensionless driving force, or order unity, depending on the cracking pattern and elastic mismatch. The practical significance of this dimensionless number was first documented by Evans *et al.* (1988). Common cracking patterns are sketched in Fig. 43, together with their Z-values, where the film–substrate system is taken to be elastically homogeneous, and the substrate semi-infinite.

Equation (5.2) provides a design limit. Given the mechanical properties and misfit stress, a specific cracking pattern is inhibited if the film is thinner than a *critical thickness*, given by

$$h_c = \Gamma\bar{E}_f/Z\sigma^2, \tag{5.3}$$

where Γ is the relevant fracture resistance. The following example illustrates a routine application using the information gathered in this section.

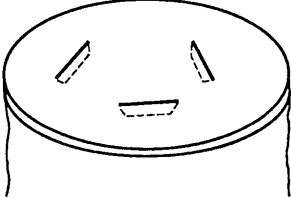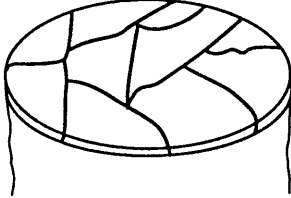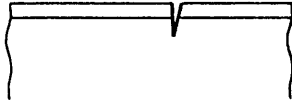| Cracking Patterns	$\mathcal{G} = Z\sigma^2 h/\bar{E}_f$

Surface Crack

Z = 3.951

Channeling

Z = 1.976

Substrate Damage

Z = 3.951

Spalling

Z = 0.343

Debond

$Z = \begin{cases} 1.028 \text{ (initiation)} \\ 0.5 \text{ (steady - state)} \end{cases}$

FIG. 43. Commonly observed cracking patterns. The dimensionless driving force for each pattern is listed, assuming that the film–substrate is elastically homogeneous, and the substrate is infinitely thick.

Consider channeling cracks in a glass film coated on a thick SiO_2 substrate. Suppose $\Gamma_f = 7$ J/m^2, $\bar{E}_f = 70$ GPa, $\sigma = 50$ MPa. One reads from Fig. 43 that $Z = 1.976$, which is appropriate since glass and SiO_2 have similar elastic moduli. The critical film thickness computed from (5.3) is $h_c \approx 100\,\mu$m. The channel network is *not* anticipated if the film is thinner than $100\,\mu$m.

2. *Cracking Patterns*

Let us go through Fig. 43 to define the various cracking modes. A *surface crack* is nucleated from a flaw, and arrested by the interface. Yet the stress is not high enough for the crack to channel through the film. Since flaws are necessarily isolated, one would see stabilized, unconnected slits. The driving force available for surface cracks is high, as indicated by the large value of Z. Isolated cracks are detrimental for some applications, such as corrosion protection coatings, but tolerable for others.

The *channeling* process is unstable: Once activated, it would never arrest until it encounters another channel or an edge. Consequently, a connected channel network would emerge, surrounding islands of the intact film. Such cracking may not be acceptable for most applications, but, for example, is common in glaze on fine pottery, and in pavement of roads.

Cracks in a film can propagate further to cause *substrate damage*. This Z-value is the largest on the list. Such a crack may be stabilized at a certain depth, since the misfit stress is localized in the film. However, the crack may divert to run parallel to the interface, leading to the next cracking pattern.

Substrate spalling is an intriguing phenomenon: The crack selects a path at a certain depth parallel to the interface, governed by $K_{II} = 0$. This is not a localized failure pattern in that extensive flakes can be spalled off. Fortunately, the Z-value for spalling is quite low. If a small amount of substrate damage is acceptable, one gains substantial flexibility in design.

Debonding may initiate from edge defects or channel bottoms. The latter can be stable: The driving force for initiation is higher than that for the long debond. This fact is exploited to introduce pre-cracks for certain types of fracture specimens, such as the UCSB four-point flexure specimen.

In the following sections, these failure modes will be examined in some detail. Emphasis is placed on the relevant elasticity problems that lead to estimates of the driving force number Z. Experimental efforts will be cited in passing. The writers hope this catalog will be used critically by experimentalists in various disciplines, thereby allowing the catalog to be validated or modified.

B. Cracking in Films

Imagine a process with increasing tensile stress in the film, for example, the cooling process. As illustrated in Fig. 43, a surface flaw is activated by the tensile stress, grows towards the interface, and then arrests if the substrate and interface are tough. With further stress increase, the crack may channel through the film. The two stages will be treated separately in the following.

1. *Surface Cracks*

We model the situation by a plane strain crack; see the insert in Fig. 45. This is appropriate for an initial surface flaw of length several times h, but may not be valid for an equiaxial flaw. The latter is studied by He and Evans (1990a) but is omitted here. The plane strain problem has been solved by Gecit (1979) and Beuth (1990). The following paragraph is a digression to a few mathematical considerations that capture the main features of the solution, and which may be skipped without discontinuity in the content.

The dimensionless stress intensity factor $K/\sigma\sqrt{h}$ depends only on the relative crack depth a/h and Dundurs' parameters α and β. For small a/h, regardless of the elastic mismatch, the stress intensity factor merges to that of an edge crack in a semi-infinite space, i.e., $K \to 1.1215\sqrt{\pi a}\,\sigma$ as $a/h \to 0$. Asymptotic behavior for another limiting case, $a/h \to 1$, can be obtained by invoking the Zak–Williams singularity: the stress singularity for a crack perpendicular to, and with the tip on, the interface. Instead of the square root singularity, the stresses near such a crack tip behave like $\sigma_{ij} \sim \tilde{K}r^{-s}f_{ij}(\theta)$, where (r, θ) is the polar coordinate centered at the tip, and the f_{ij} are dimensionless angular distributions. The scaling factor $\tilde{K}$ plays a part analogous to the regular stress intensity factor, but having different dimensions: [stress][length]^s. The singularity exponent s $(0 < s < 1)$ depends on elastic mismatch, and is the root to

$$\cos(s\pi) - 2\frac{\alpha - \beta}{1 - \beta}(1 - s)^2 + \frac{\alpha - \beta^2}{1 - \beta^2} = 0. \qquad (5.4)$$

The numerical solution of s is plotted in Fig. 44. For a crack that penetrates the film, $\tilde{K} \sim \sigma h^s$, with the pre-factor dependent on α and β only. As $a/h \to 1$ but with the crack tip still within the film, the stress field away from the small ligament $(h - a)$ would not feel such a detail, and behaves as if the crack tip were just on the interface, governed by $\tilde{K}$. Dimensional considerations require the stress intensity factor K to be related to the far
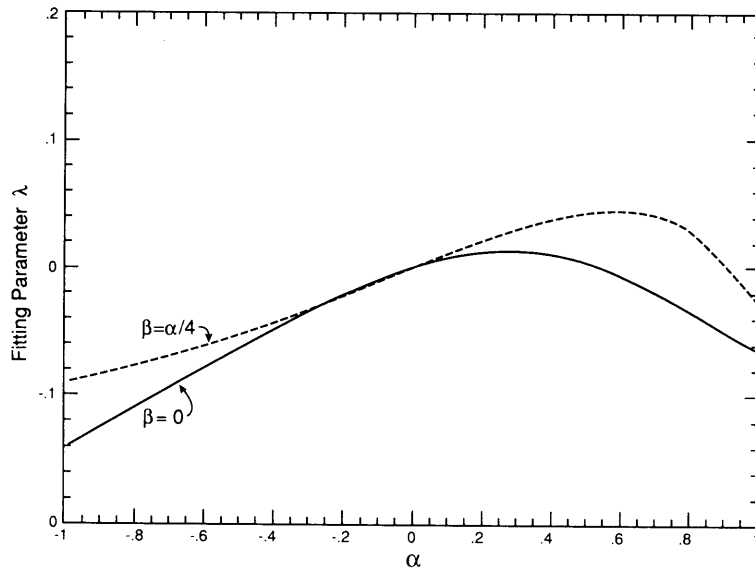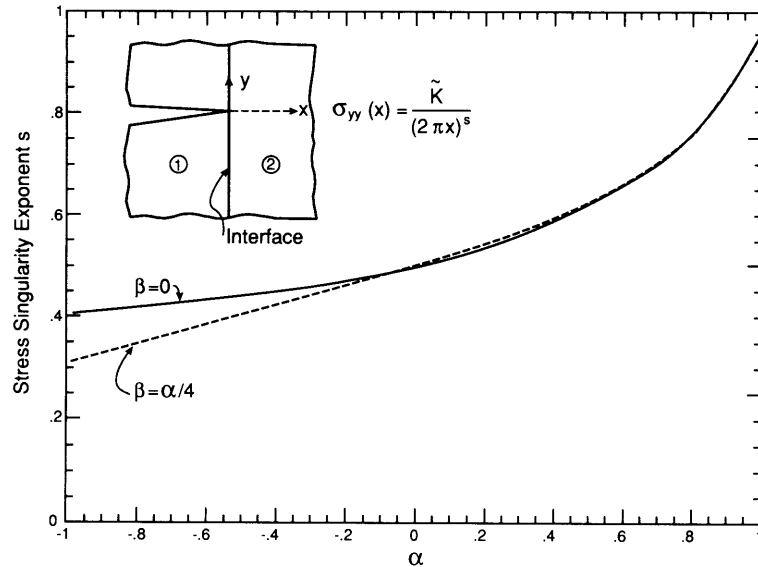
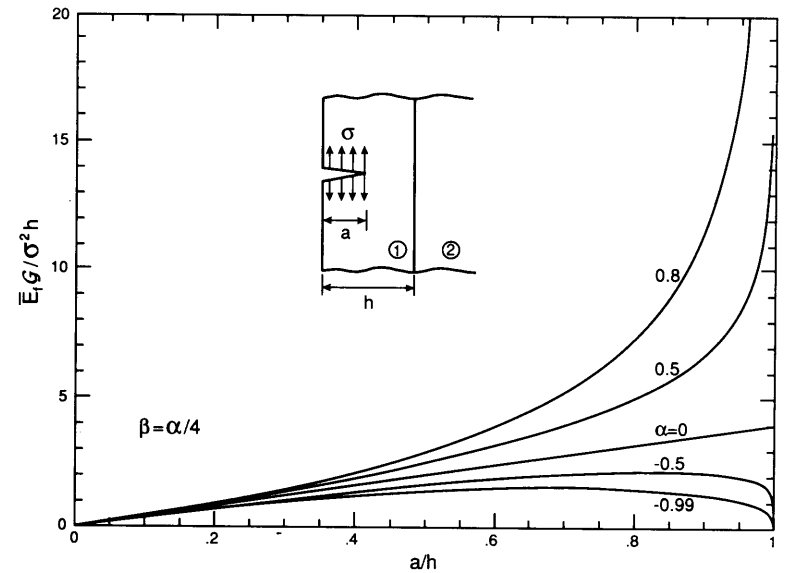FIG. 44. (a) Zak–Williams singularity. (b) A curve fitting parameter.

FIG. 45. Driving force available for an edge crack at various depths a/h.

field $\tilde{K}$ according to $K \sim \tilde{K}(h - a)^{1/2-s}$. Combination of the preceding gives $K/\sigma\sqrt{h} \sim (1 - a/h)^{1/2-s}$ as $a \to h$.

Motivated by these considerations, Beuth fitted his numerical solution with

$$K/\sigma\sqrt{h} = 1.1215\sqrt{\pi}(a/h)^{1/2}(1 - a/h)^{1/2-s}(1 + \lambda a/h), \qquad (5.5)$$

where λ is taken to be independent of a/h, and is chosen such that the formula agrees with the full numerical solution at $a/h = 0.98$; the results are plotted in Fig. 44b. The error of (5.5) is within a few percent for intermediate a/h. Equation (5.5) is plotted in Fig. 45 in terms of the dimensionless energy release rate. The energy release rate starts from zero for shallow flaws. As the crack approaches the interface, it drops to zero for relatively compliant films ($\alpha < 0$), but diverges to infinity for stiffer films ($\alpha > 0$).

One needs *a priori* knowledge of flaw size to predict a failure stress or the maximum tolerable film thickness. In practice, a plausible flaw depth may be assumed according to the "quality" of the film. Taking, say, $a/h = 0.8$, one can obtain the nondimensional driving force Z from Fig. 45 for a known elastic mismatch. The flaws will not be activated if the dimensionless fracture resistance satisfies $\Gamma_f \bar{E}_f/\sigma^2 h > Z$.

Observe that for relatively compliant films, the driving force attains a maximum at an intermediate depth. The practical significance is that no flaws, regardless of initial depth, can be activated, provided the dimensionless resistance $\Gamma_f \bar{E}_f / \sigma^2 h$ is greater than the maximum. Such a maximum, depending on the elastic mismatch α and β, provides a fail-safe bound for relatively compliant films.

2. Cracks Channeling through a Film

Figure 46 shows a crack channeling through the film. Complications such as substrate penetration, interface debond, and channel interaction are assumed not to occur for the time being. At each instant of the growth, the channel front self-adjusts to a curved shape, such that energy release rate at every point on the front is the same. The elasticity problem is three-dimensional in nature, and an accurate solution would require iteration of the front shape. After the length exceeds a few times the film thickness, the channel asymptotically approaches a steady-state: the entire front maintains its shape as it advances; so does $\delta(z)$, the cross-section profile in the wake, which attains the shape of a plane strain through-crack. The steady-state cracking is analogous to that discussed in Section III.A.1.
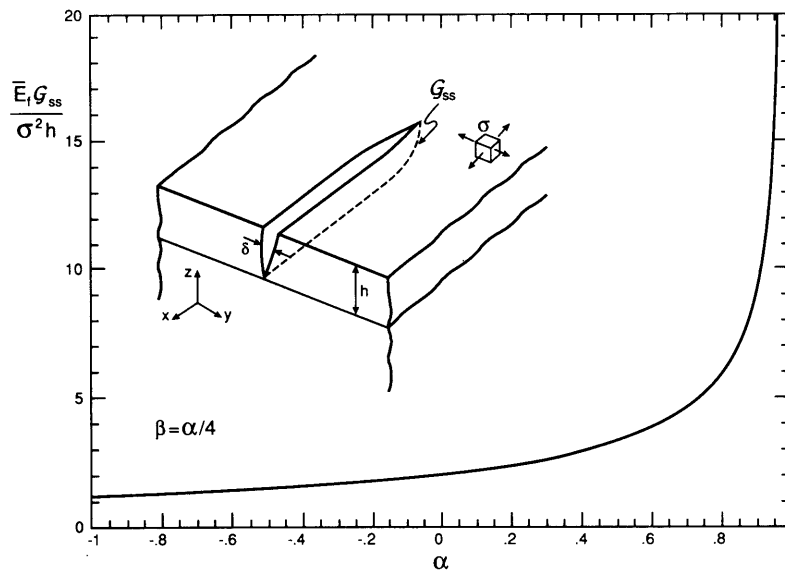

FIG. 46.   The insert shows a crack channeling across the film, driven by the tensile stress in the film. The available energy at the channel front is plotted for various elastic mismatch.

In the steady state, the energy release rate at the channel front can be evaluated using two *plane problems*—that is, by subtracting the strain energy stored in a unit slice far behind of the front, from that far ahead. The calculation does not require the knowledge of the front shape. Alternative formulae have been developed with this idea. One is

$$G_{ss} = \frac{1}{2h} \int_0^h \delta(z)\sigma(z)\,dz. \qquad (5.6)$$

Two plane problems are involved: the stress distribution on the prospective crack plane before cracking, $\delta(z)$, which, for the present situation, equals the uniform misfit stress σ, and the displacement profile for a plane strain crack, $\delta(z)$. This is particularly convenient for numerical computation.

A second formula is

$$G_{ss} = \frac{1}{h} \int_0^h G(a)\,da, \qquad (5.7)$$

where $G(a)$ is the energy release rate of a plane strain crack of depth a in Fig. 45. A mathematical interpretation is that G_{ss} is the average of energy release rates for through-cracks at various depths. Both formulae are valid for films and substrates with dissimilar elastic moduli.

As an example, suppose the film–substrate is elastically homogeneous, and the substrate occupies a semi-infinite space. The corresponding plane strain problem is an edge crack in a half plane, with energy release rate $G(a) = 3.952\sigma^2 a/\bar{E}$ (Tada *et al.*, 1985). The integral (5.7) gives $G_{ss} = 1.976\sigma^2 h/\bar{E}$. This pre-factor is listed in Fig. 43.

Beuth (1990) carried out an analysis of a thin film on a semi-infinite substrate with dissimilar elastic moduli. The result is reproduced in Fig. 46. If the dimensionless toughness $\Gamma_f \bar{E}_f / \sigma^2 h$ is below the curve, a channel network is expected. Observe that a compliant substrate ($\alpha > 0$) provides less constraint, inducing higher driving force for channeling.

The channeling cracks were studied analytically by Gille (1985) using the numerical solutions available at that time, and subsequently by Hu and Evans (1988) with a combination of calculations and experiments. The concept has been extended as a fail-safe bound for cracking in multilayers (Suo, 1990b; Ho and Suo, 1990; Ye and Suo, 1990; Beuth, 1990). Applications include thin films, reaction product layers, adhesive joints, and hybrid laminates.

3. Multiple Channeling

The preceding technique can be extended to study interaction among channels. Suppose the biaxial stress is biased so that parallel channels
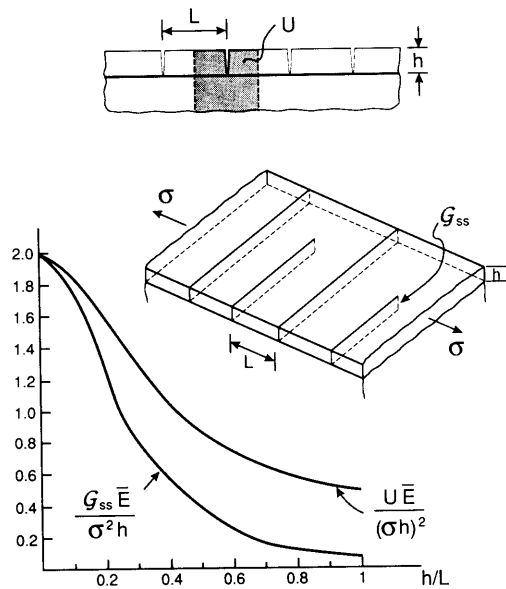
FIG. 47.   Interaction of multiple channels.

develop in one direction; see the inserts in Fig. 47. For simplicity, attention is restricted to an elastically homogeneous system with a semi-infinite substrate.

Consider a periodic set of edge cracks of depth a, spacing L, and subject to an opening stress σ. The energy release rate at each crack tip, $G(a)$, is found in Tada et al. (1985) in a graphic form, which is then fitted by a polynomial. Based on this information, energetic accounting gives the driving force for cracks channeling in the film.

The strain energy, per crack, gained in creating a set of cracks of depth h is

$$U = \int_0^h G(a)\, da = f\sigma^2 h^2/\bar{E}, \qquad (5.8)$$

where the dimensionless factor f depends on the crack density h/L. The results obtained by a numerical integration are plotted in Fig. 47. If these cracks are equally extended in the channeling direction, the energy release rate at each front is $G_{ss} = U/h = f\sigma^2 h/\bar{E}$. Thus, f is the dimensionless driving force for this situation. Thouless (1990a) has employed this solution in his discussion of crack spacing in thin films.

Next, consider the situation in Fig. 47 where, at a certain stage of loading, the cracks of spacing $2L$ have already channeled across the film, and the

tensile stress in the film has therefore been partially relieved. With further increase of the loading, a new set of cracks are nucleated and grow half-way between the existing channels. The energy release rate at the front of the growing cracks should be computed from

$$G_{ss} = (2U_L - U_{2L})/h = [2f(h/L) - f(h/2L)]\sigma^2 h/\bar{E}. \qquad (5.9)$$

This is derived from the strain energy difference far behind and far ahead of the channeling fronts.

The result is also plotted in Fig. 47. Given the mechanical properties and with the identification $G_{ss} = \Gamma_f$, the plot may be viewed as a relation between the stress level and the channel density. Notice we have assumed that new cracks can always be readily nucleated half-way between existing channels. This might overestimate the crack density for a given stress level. An analysis with aspects similar to the preceding has also been carried out independently by Delannay and Warren (1991).

C. SUBSTRATE CRACKING

Substrate damage may originate from edges or existing channel cracks in the film. The two substrate cracking patterns in Fig. 43 are studied in this section. Observe that the Z-values for the two patterns differ by an order of magnitude.

1. Substrate Damage Caused by Cracks in Films

Suppose the channel cracks in the film have developed at some stage during the cooling but have not yet grown into the substrate, either because the substrate is much tougher or because sufficiently large substrate surface defects are not readily available. The issue is whether these cracks would propagate into the substrate upon further cooling. The problem has been studied by Ye and Suo (1990), and the main results are summarized here.

The driving force for a plane strain crack into a substrate was analyzed using finite elements, and the results are plotted in Fig. 48. Observe that the driving force decays for deep cracks, implying stable propagation. For relative compliant films ($\alpha < 0$), the driving force starts from zero at the interface, and attains a maximum at very small depths. It is difficult for finite elements to resolve these details, so the trend is sketched by dashed lines.
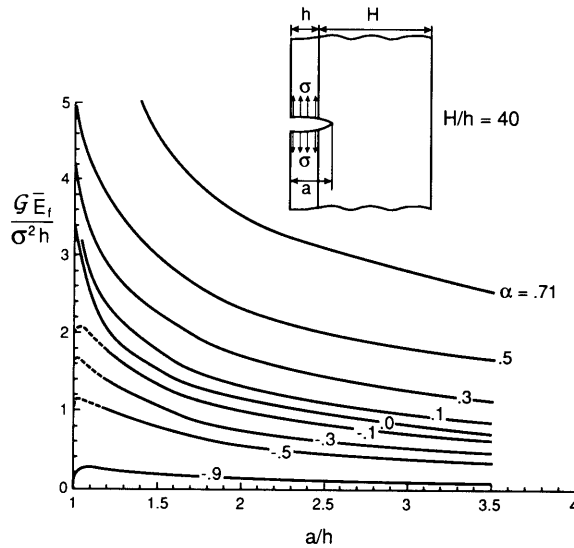
FIG. 48.   Energy release rate for a plane strain crack with the tip in the substrate.

The plane strain model is not quite correct, since cracks must be re-nucleated, in a three-dimensional fashion, from a surface flaw on substrate. The insert of Fig. 49 shows a crack growing laterally under an existing channel in the film. The crack arrests at a certain depth because of the decay of the available driving force. The energy release rate at the growing front
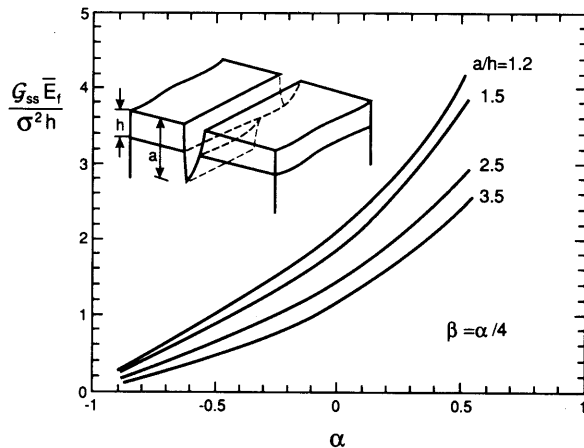

FIG. 49.   Energy release rate for a crack propagating under a channel in the film.

may be computed from

$$G_{ss} = \frac{1}{a - h} \int_h^a G(a')\, da'. \qquad (5.10)$$

Again, this is derived from energy accounting. The integral is evaluated using the preceding plane strain results, and the results are summarized in Fig. 49. The plot may be used as a damage tolerance map: Given a damage tolerance a/h, one can read the design number Z. Take the curve for $a/h = 1.2$ as an example. Provided the dimensionless substrate toughness $\Gamma_s \bar{E}_f / h\sigma^2$ is above the curve, no channel with depth $a/h > 1.2$ is anticipated. This holds true even if the initial flaws are deeper than 1.2, as long as they are not channels themselves. Observe that the elastic mismatch plays a significant role. A relatively compliant substrate would provide less constraint, leading to larger driving force.

The so-called T-stress in (2.1) has also been computed by Ye and Suo and is found to be positive, unless the film is much stiffer than the substrate and the crack depth is small. As shown by Cotterell and Rice (1980), a positive T-stress results in a tendency for a straight mode I crack to veer off to one side or the other. Further discussion of crack path stability in a related context is given in Section VIII.C. Here, we simply note that the substrate crack will have a strong tendency to branch into a path parallel to the interface, a cracking pattern to be discussed next.

2. Spalling of Substrates

Cracks, originating from either defects in the film or at the edge, have a strong tendency to divert into the substrate, should the latter be brittle, and follow a trajectory parallel to the interface; see Fig. 43. The key insight was provided by Thouless et al. (1987) in a coordinated experimental and theoretical investigation. Their initial intent was to model the impact of ice sheets on offshore structures. The experiments were conducted with PMMA and glass plates, loaded on the edges. Spalling cracks were found to follow a trajectory parallel to the surface, with depth governed by the criterion $K_{II} = 0$. (See also Thouless and Evans, 1990.)

These authors remarked to the effect that this mechanism would operate in the edge spalling of pre-tensioned films, previously observed by Cannon et al. (1986). As schematically shown in Fig. 43, the crack initiates at the edge, extends along the interface for typically about two times film thickness, then kinks into the substrate, and finally runs parallel to the

interface at a depth of a few times the film thickness. In this case, the under-lying mechanics is the same for giant ice sheets as for micro-electronic films.

Thorough investigations on pre-tensioned films have been conducted, experimentally and analytically, by Hu et al. (1988), Hu and Evans (1988), Drory et al. (1989), Suo and Hutchinson (1989b), and Chiao and Clarke (1990). Focus here is on the steady-state spalling, with the transient stage ignored, since the former provides a well-defined design limit. In the follow-ing, the essential mechanics will be elucidated using a simple system, and results will be cited for more general cases. The analysis is arranged separately for spalling originating from edges or channel cracks (planar geometry), and from holes.

a. Planar Geometry

Inserted in Fig. 50 is a long crack at a depth d in the substrate, driven by the residual tension in the film. Plane strain conditions are assumed. The film is attached to a semi-infinite substrate with the same elastic moduli. Results without these restrictions will be cited later. The equivalent edge force and moment due to σ are

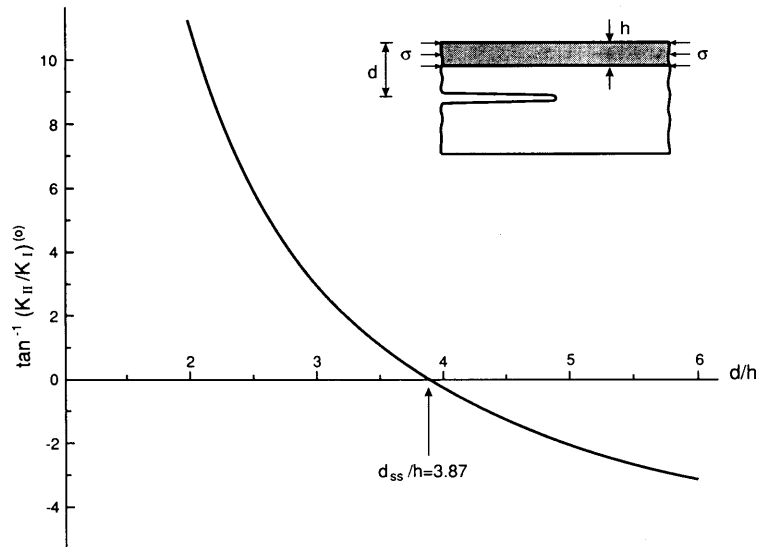$$P = \sigma h, \qquad M = \sigma h (d - h)/2. \qquad (5.11)$$

FIG. 50.   The insert shows a spalling crack. The plot is the mode mixity for crack at various depths.

Specialized from (3.12), the stress intensity factors are

$$K_{\text{I}}/\sigma\sqrt{h} = (h/2d)^{1/2}[\cos\omega + \sqrt{3}(1 - h/d)\sin\omega], \qquad (5.12)$$

$$K_{\text{II}}/\sigma\sqrt{h} = (h/2d)^{1/2}[\sin\omega - \sqrt{3}(1 - h/d)\cos\omega]. \qquad (5.13)$$

where $\omega = 52.07°$. The mode mixity $\psi = \tan^{-1}(K_{\text{II}}/K_{\text{I}})$ is plotted as a function of crack depth in Fig. 50. Notice $K_{\text{II}} > 0$ for small depth, but $K_{\text{II}} < 0$ for large depth and, consequently, a pure mode I trajectory exists at an intermediate depth.

This steady-state spalling depth d_{ss} is determined from (5.13) with $K_{\text{II}} = 0$. Thus,

$$d_{\text{ss}} = 3.86h. \qquad (5.14)$$

The steady-state, mode I energy release rate can now be readily evaluated from (5.12), which gives

$$G_{\text{ss}} = 0.343\sigma^2 h/\bar{E}. \qquad (5.15)$$

This pre-factor was cited in Fig. 43.

Suo and Hutchinson (1989b) carried out an extensive analysis to include elastic mismatch and finite thickness of the substrate. The general solution for arbitrary edge loads is summarized in Section III.B.5. The results for spalling cracks caused by the residual stress in the film are reproduced in Fig. 51. Observe that the spalling depth depends strongly on both elastic mismatch and substrate thickness. However, the dimensionless stress intensity factor is insensitive to the substrate thickness as long as $H/h > 10$.

There has been no formal proof that the spalling trajectory is configura-tionally stable. One heuristic explanation, as shown in Fig. 51, is that $K_{\text{II}} > 0$ when $d < d_{\text{ss}}$, implying that a crack above d_{ss} would be driven down. Analogously, a crack below d_{ss} would be driven up.

b. Spalling from Circular-Cut

Figure 52 shows an axial-section of a spalling crack emanating from the edge of a circular-cut in the film, driven by residual tensile stress in the film. In general, a hole in a pre-tensioned film acts like a stress raiser. However, it differs from an open hole in a plate in that, for the former, cracking is usually confined within a few times hole radius. Other cracking modes around holes include channel cracks in films and decohesion of interfaces. The latter will be treated in the next section.

As indicated in Fig. 52, the hole radius is b_0, and the crack extends to a radius b. For simplicity, the elastic moduli for the film and substrate are
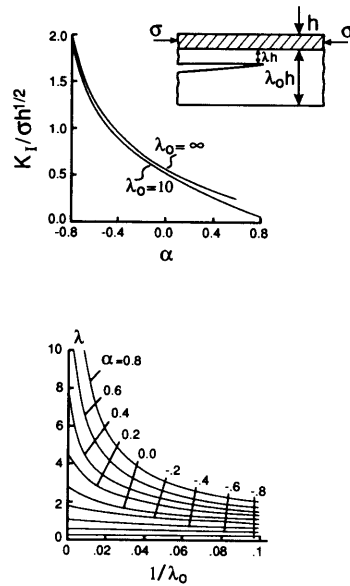
FIG. 51. Spalling results for film–substrate of dissimilar elastic constants and finite substrate. Both mode I stress intensity factor for the steady-state propagation and the depth of the crack path are given.
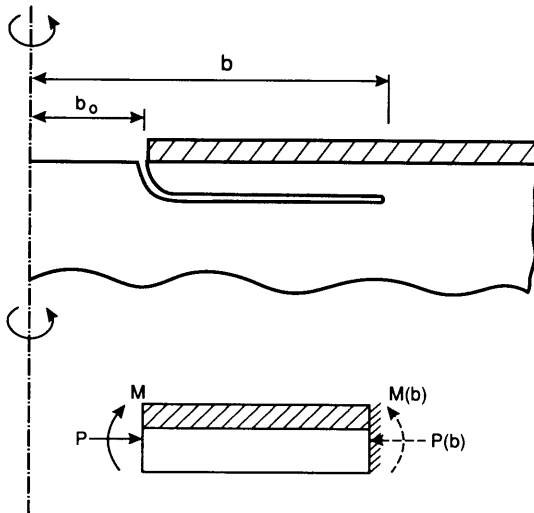

FIG. 52. An axial-section of spalling from the edge of a circular-cut.

taken to be the same, and the substrate semi-infinite. The equivalent edge force P and moment M, per unit length, are still given by (5.11). The stress state in the annulus between b_0 and b can be determined by the classical plate theory, with the outer boundary clamped. The analysis shows that the moment and force at the crack front are modified by a factor:

$$M(b) = M/k, \qquad P(b) = P/k, \tag{5.16}$$

where

$$k = \tfrac{1}{2}[(1 + \nu) + (1 - \nu)(b/b_0)^2]. \tag{5.17}$$

These loads are indicated in Fig. 52.

The results of Section III.B.1.d are applicable with moment and force $M(b)$ and $P(b)$ used. In particular, the energy release rate is modified by factor k^2, i.e.,

$$G = \frac{1}{2k^2}\left(\frac{M^2}{I} + \frac{P^2}{A}\right), \qquad I = \frac{1}{12}\bar{E}d^3, \qquad A = \bar{E}d. \tag{5.18}$$

This result can also be derived by an energetic accounting, i.e.,

$$G = (2\pi b)^{-1}\, \partial U/\partial b,$$

where U is the strain energy stored in the clamped circular plate. From this latter approach, it would be clear that the solution is the exact asymptote as $(b - b_0)/h \to \infty$.

The stress intensity factors (5.12) and (5.13) are modified accordingly by a factor of k. Thus, the steady-state depth d_{ss} is independent of b/b_0, and is identical to the plane strain result (5.14). The mode I driving force for spalling now becomes

$$G = \frac{0.343\sigma^2 h}{k^2 \bar{E}}. \tag{5.19}$$

Since k increases with b/b_0, the spalling crack from a circular-cut would usually arrest.

D. INTERFACE DEBOND

Pre-tensioned films are susceptible to decohesion or, more precisely, de-adhesion, from substrates. Flaw geometry plays an important role: Debonding emanating from an edge defect, a hole, or a through-cut would behave differently. Analytical results for the first two geometries will be summarized, and the third can be found in Jensen et al. (1990).
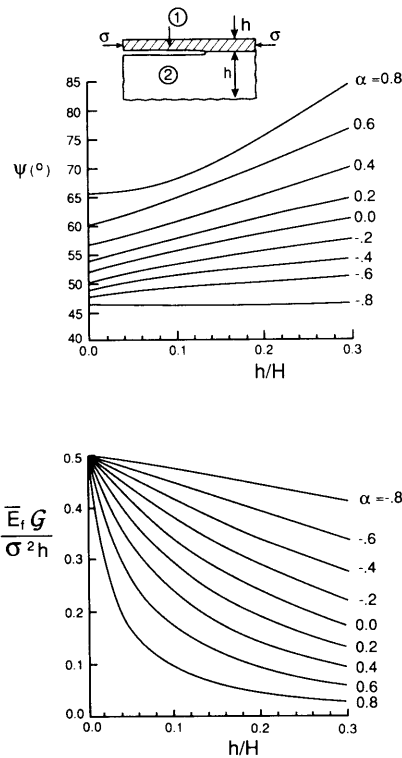
FIG. 53.   Mode mixity and energy release rate for a debonding crack.

1. *Decohesion from Edges or Channels*

Figure 53 illustrates a pre-tensioned film debonding from a substrate. The edge load is a special combination of that studied in Section III.B.4, and the notation there is followed. The misfit stress is equivalent to the mechanical loads (see Fig. 26):

$$P_1 = P_3 = \sigma h, \qquad M_3 = (1/2 + 1/\eta - \Delta)\sigma h^2, \qquad M_1 = 0. \quad (5.20)$$

Specialized from Eq. (3.22), the energy release rate is

$$G = \frac{\sigma^2 h}{2\bar{E}_f}\left[1 - \frac{\Sigma}{A} - \frac{\Sigma(1/2 + 1/\eta - \Delta)^2}{I}\right]. \quad (5.21)$$

The loading phase ψ is defined by $K = |K|h^{-i\varepsilon}\exp(i\psi)$, as is consistent with the convention in (2.45) with $l = h$. Both the driving force and mode mixity are plotted in Fig. 53. Observe that the decohesion process is inherently mixed mode, consisting of somewhat more sliding than opening.

The effect of the substrate thickness on the driving force is significant when the film is stiff.

Argon *et al.* (1989) have used the residual stress as a driving force to measure interface toughness. The result in this section can also be used to calibrate the residual stress effect on some interface fracture specimens, e.g., the UCSB four-point flexure specimen. The complex interfacial stress intensity factor is a superposition of the contribution from residual stress and that from mechanical load.

2. *Decohesion from a Hole*

Figure 54 illustrates a decohesion crack emanating from the edge of a hole in a pre-tensioned film. Results developed in Section C.2.b for substrate spalling are still valid here. In particular, the energy release rate is given by

$$G = \frac{h\sigma^2}{2\bar{E}_f k^2}, \quad (5.22)$$

where k is given by Eq. (5.17). The result is now valid for films and substrates with dissimilar elastic constants, but the substrate is still assumed to be much thicker than the film. The mode mixity is independent of b/b_0 when $(b - b_0)/h$ is sufficiently large, and is identical to the plane strain results (Fig. 53, $h/H = 0$).

Decohesion from a circular-cut is stable and has been used to determine interface toughness by Farris and Bauer (1988) and Jensen *et al.* (1990). This is particularly feasible when the film is transparent, so that the decohesion radius b can be readily measured.
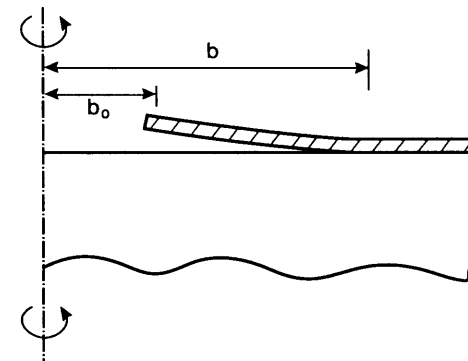

FIG. 54.   An axial-section of a decohesion annulus originated from an edge of a circular-cut.
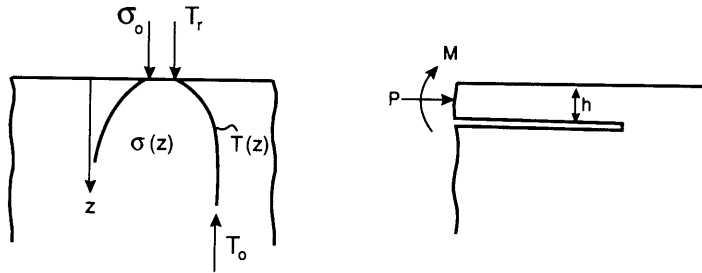
Fig. 55. A model for thermal shock spalling.

E. Thermal Shock Spalling

1. An Idealized Model

Consider a block of brittle material with a thin, pre-tensioned, surface layer. Spalling is possible if the residual stress has a negative gradient with depth. An example is depicted in Fig. 55. A semi-infinite body is initially immersed in a heat bath of temperature T_0, so that a uniform temperature is established in the body. Upon the removal of the block from the bath, the surface temperature is assumed to drop instantaneously to the room temperature T_r. A biaxial tensile residual stress thus develops in a surface layer, as shown schematically in Fig. 55. The equivalent edge force and moment are also indicated. The stress profile changes with the time, and so does the ratio M/P.

The problem features a dimensionless number

$$\xi = h/\sqrt{t\alpha_D}, \tag{5.23}$$

where h is the depth of the crack parallel to the surface, α_D the thermal diffusivity, and t the time elapsed after the removal of the heat source. At any given time, a mode I crack path parallel to the surface is available—that is, a number ξ_{ss} exists where $K_{II} = 0$. However, for small t, the depth h is correspondingly small, and therefore the strain energy stored in such a thin layer is insufficient to drive the spalling. Consequently, a certain time elapse is needed before spalling. The following is an attempt to quantify these considerations.

2. Spalling Depth and Time Elapse

Consider first the temperature and stress field prior to cracking. At a given time t after the removal from the heat bath, the temperature at a

---

depth z is

$$T(z, t) = T_0 + (T_r - T_0)\,\mathrm{erfc}(z/2\sqrt{t\alpha_D}). \tag{5.24}$$

The biaxial, tensile, thermal stress field varies with the depth and time, in accordance with

$$\sigma_x = \sigma_y = \sigma(z, t) = \sigma_0\,\mathrm{erfc}(z/2\sqrt{t\alpha_D}), \tag{5.25}$$

where

$$\sigma_0 = \alpha_E(T_0 - T_r)E/(1 - \nu), \tag{5.26}$$

and α_E is the thermal expansion coefficient. These are classical solutions, which may be extracted from standard textbooks.

Next consider the half space with a spalling crack (Fig. 55). The resultant force and moment can be expressed as

$$P = I\sigma_0 h, \qquad M = (\tfrac{1}{2}I - J)\sigma_0 h^2, \tag{5.27}$$

where

$$I(\xi) = \frac{1}{\xi}\int_0^\xi \mathrm{erfc}(u/2)\,du, \qquad J(\xi) = \frac{1}{\xi^2}\int_0^\xi u\,\mathrm{erfc}(u/2)\,du. \tag{5.28}$$

The stress intensity factors can be calculated from Section III.B.1.d.

The number ξ corresponding to a mode I trajectory is determined by enforcing $K_{II} = 0$. The problem involves a nonlinear algebraic equation, and the numerical solution gives

$$h_{ss} = 6.82\sqrt{t\alpha_D}. \tag{5.29}$$

The corresponding mode I stress intensity factor is

$$K_I = 0.190\sigma_0\sqrt{h_{ss}}. \tag{5.30}$$

Given the toughness and stress level, the depth h_{ss} may be predicted from (5.30), and the time elapse for spalling can then be estimated from (5.29). Observe that the spalling depth is independent of the thermal diffusivity, as a feature of this idealized model. As an example, consider a glass with $K_{Ic} = 0.7\,\mathrm{MPa\,m^{1/2}}$, $\sigma_0 = 100\,\mathrm{MPa}$, $\alpha_D = 0.7 \times 10^{-6}\,\mathrm{m^2/s}$. The predicted crack depth is $h_{ss} = 1.4\,\mathrm{mm}$, and the time to spalling is $t = 6 \times 10^{-2}\,\mathrm{s}$. This tiny time elapse is possibly an outcome of the idealized temperature boundary condition that has been adopted.

VI. Buckle-Driven Delamination of Thin Films

In many film/substrate systems, the film is in a state of biaxial compression. Residual compression has been observed in thin films that have been
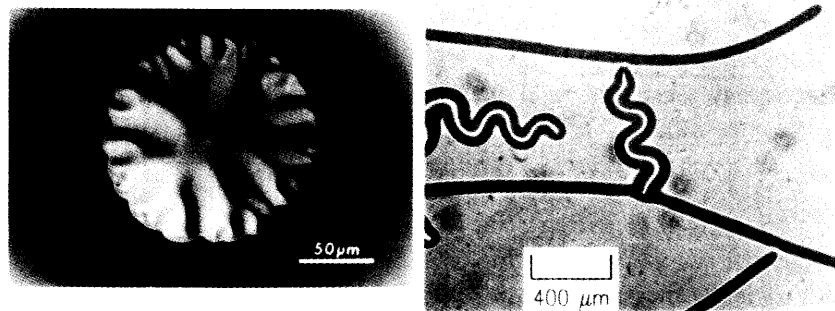
FIG. 56. The photograph on the left from Argon *et al.* (1989) shows a SiC film on a Si substrate delaminating as a wavy circular blister. On the right is a photograph supplied by M. D. Thouless, which shows examples of the straight-sided blister and the telephone cord blister occurring in a multilayered film delaminating from a glass substrate.

sputtered or vapor deposited and it can arise from thermal expansion mismatch. Some remarkable failure modes of such systems have been observed, examples of which are shown in Fig. 56. These pictures reveal regions where the film has been buckled away from the substrate. Various shapes of the buckled regions evolve, including long straight-sided blisters, circular blisters with and without wavy edges, and the so-called telephone cord blister, which is perhaps the most common morphology. The failure entails the film first buckling away from the substrate in some small region where adhesion was poor or nonexistent. Buckling then loads the edge of the interface crack between the film and the substrate, causing it to spread. The failure phenomenon couples buckling and interfacial crack propagation. The straight-sided blister grows at one of its ends. The telephone cord blister grows at its end as if a worm were tunneling beneath the film.

This section presents an analysis of the straight-sided and circular blisters and concludes with some speculation about the origin of the telephone cord morphology. It will be seen that a key aspect of the phenomena is the mixed mode fracture behavior of the interface, wherein $\Gamma(\psi)$ increases sharply with increasing mode 2.

Formulas relating the energy release rate of the interface crack to the buckling parameters were derived for one-dimensional ply buckles on the surface of laminated composites by Chai *et al.* (1981). Essentially identical results were obtained by Evans and Hutchinson (1984) and Gille (1985) for the thin-film problem. The energy release rate for the circular blister in biaxially compressed films was given by Evans and Hutchinson (1984) and

Yin (1985). The significance of the mixed mode character of the interface crack tip was apparently first appreciated by Whitcomb (1986), who showed that the crack tip becomes predominately mode 2 as a one-dimensional ply buckle spreads. His observation was essential to explain why the buckles do not keep spreading along their edges under constant overall load—that is, why the buckles have a characteristic width. Whitcomb was concerned with compressive failure modes in layered composites. Here, the concern will be with thin films under equi-biaxial compression, but a number of the results and conclusions carry over directly to ply delamination. Storakers (1988) and Rothschilds *et al.* (1988) deal with various aspects of buckling and delamination in composites, and these authors cite relevant literature in the composites arena.

This section starts with a one-dimensional analysis of the infintely long straight-sided blister, closely paralleling the analysis of Whitcomb (1986). Given the availability in Section III.B.4 of the relationships between the interface stress intensity factors and the moment and resultant force change at the edge of the buckle, the one-dimensional analysis can be carried out in closed form. The analysis of the circular blister, which requires some numerical work, is presented next. The two sets of results are then combined in an analysis of steady-state propagation of a straight-sided blister. The steady-state problem gives perhaps the sharpest insights into design constraints on compressed films.

A. The One-Dimensional Blister

Consider an x-independent segment of the straight-sided blister shown in Fig. 57. The film is taken to be elastic and isotropic with Young's modulus E_1, Poisson's ratio ν_1, and thickness h. The substrate is also assumed to be isotropic but with modulus E_2 and Poisson's ratio ν_2. The substrate is modeled as being infinitely deep. The film is assumed to be unattached to the substrate in the strip region $-b \le y \le b$. A plane strain interface crack of width $2b$ exists between the film and the substrate.

The unbuckled film is assumed to be subject to a uniform, equi-biaxial compressive in-plane stress, $\sigma_{xx} = \sigma_{yy} = -\sigma$. In the unbuckled state, the stress intensity factors at the crack tips vanish. Only when the film buckles away from the substrate are nonzero stress intensity factors induced. Under the assumption that $h \ll b$, the film is represented by a wide, clamped Euler column of width $2b$. The complex stress intensity factor K at the right-hand

tip is related to the moment M and to the *change* in resultant stress ΔN at the right-hand end of the column by the relationships given for the 2-layer problem in Section III.B.4. Use of the 2-layer solution to characterize the crack tip field is justified if $h/b \ll 1$, which is, in any case, the condition for the validity of the Euler theory. In what follows, the 2-layer solution is first specialized for the present applications. This solution is also used in the analysis of the blister test discussed in Section VII, and should have fairly wide applicability. Then, the Euler solution is presented and is coupled to the 2-layer solution.

1. General Loading of an Edge Crack on the Interface between a Thin Film and Substrate

Let M and ΔN be defined with the sign convention in Fig. 57. These quantities will be identified with the moment/unit length and the change in resultant stress at the right end of the wide Euler column. Specializing the solution of Section III.B.4 to the limit of the infinitely deep substrate, one finds for the interface crack:

$$G = 6(1 - \nu_1^2)E_1^{-1}h^{-3}(M^2 + h^2\,\Delta N^2/12), \qquad (6.1)$$

$$Kh^{i\varepsilon} = -\left[\frac{6(1-\alpha)}{1-\beta^2}\right]^{1/2}h^{-3/2}\left[\frac{h\,\Delta N}{\sqrt{12}} + iM\right]e^{i\omega}, \qquad (6.2)$$

$$\tan\psi \equiv \frac{\mathrm{Im}(Kh^{i\varepsilon})}{\mathrm{Re}(Kh^{i\varepsilon})} = \frac{\sqrt{12}\,M\cos\omega + h\,\Delta N\sin\omega}{-\sqrt{12}\,M\sin\omega + h\,\Delta N\cos\omega}. \qquad (6.3)$$
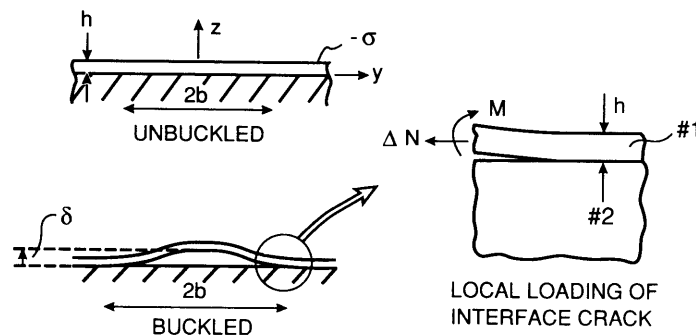

FIG. 57. Geometry of the one-dimensional blister, and conventions for the elasticity solution characterizing conditions near the tip of an interface crack between a thin film and an infinitely thick substrate. Top left: unbuckled; bottom left: buckled; right: local loading of interface crack.
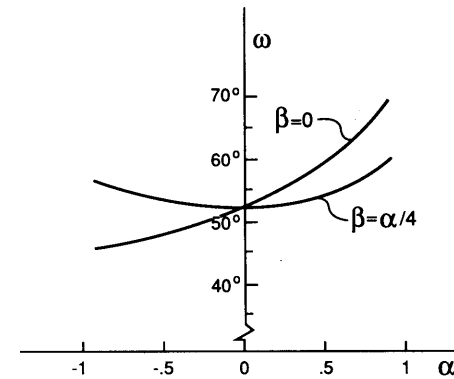
FIG. 58.   Phase factor $\omega(\alpha, \beta)$ in (6.2) and (6.3).

Here, $\omega \equiv \omega(\alpha, \beta, h/H = 0)$, which is plotted in Fig. 58 for $\beta = 0$ and $\beta = \alpha/4$. The mode mixity parameter ψ is defined using the film thickness h as the reference length l.

2. Euler Column Solution and Coupling to Interface Edge Crack Solution

The one-dimensional deformation of the wide column in Fig. 57 is characterized by the y- and z-displacements, $V(y)$ and $W(y)$. These are defined to be zero in the unbuckled state with pre-stress $\sigma_{xx} = \sigma_{yy} = -\sigma$. The wide column is taken to be characterized by von Karman nonlinear plate theory with fully clamped conditions at its edges, i.e.,

$$V = W = W, y = 0 \qquad \text{at } y = \pm b. \qquad (6.4)$$

The change in the y-component of the stretching strain measured from the unbuckled state is

$$\varepsilon_y = V, y + \tfrac{1}{2}W, y^2, \qquad (6.5)$$

while the bending strain is W, yy. With N_x and N_y as the resultant stresses and with $\Delta N_x = N_x + \sigma h$ and $\Delta N_y = N_y + \sigma h$ as the changes in the resultant stresses from the unbuckled state, the strain component ε_y is related to ΔN_y by

$$\varepsilon_y = (1 - \nu_1^2)\,\Delta N_y/(E_1 h). \qquad (6.6)$$

Since $\varepsilon_x = 0$, $\Delta N_x = \nu_1\,\Delta N_y$. The bending moment is related to the bending strain by $M_y = DW, yy$, where $D = E_1 h^3/[12(1 - \nu_1^2)]$ is the bending stiffness. In-plane equilibrium requires $\Delta N_y, y = 0$. Therefore, ΔN_y can be

taken to be the value at the end of the beam, ΔN. Moment equilibrium requires

$$DW,_{yyyy} - (\Delta N - \sigma h)W,_{yy} = 0. \tag{6.7}$$

The solution to the preceding system of equations is given in (6.8)–(6.12):

$$W = \tfrac{1}{2}\xi h[1 + \cos(\pi y/b)], \tag{6.8}$$

$$M \equiv M_y(b) = \frac{\pi^2}{2}\frac{Dh}{b^2}\xi, \tag{6.9}$$

$$\Delta N = \frac{3\pi^2}{4}\frac{D}{b^2}\xi^2. \tag{6.10}$$

The amplitude of the buckling deflection, ξ, has been defined such that $W(0) = \xi h$. It is related to the residual stress by

$$\xi = \left[\frac{4}{3}\left(\frac{\sigma}{\sigma_c} - 1\right)\right]^{1/2}, \tag{6.11}$$

where

$$\sigma_c = \frac{\pi^2 D}{b^2 h} = \frac{\pi^2}{12}\frac{E_1}{(1 - v_1^2)}\left(\frac{h}{b}\right)^2. \tag{6.12}$$

Here, σ_c is the classical buckling stress of a clamped–clamped wide plate. The residual compression in the film, σ, must exceed σ_c if the film is to buckle away from the substrate for a given interface crack length $2b$. The nondimensional "loading parameter" is σ/σ_c. Since σ_c decreases as b increases, σ/σ_c increases as b increases.

The energy release rate is determined by substituting the expressions for M and ΔN in (6.9) and (6.10) into (6.1), with the result

$$G = [(1 - v_1^2)h/(2E_1)](\sigma - \sigma_c)(\sigma + 3\sigma_c). \tag{6.13}$$

This result is in agreement with Chai *et al.* (1981), Evans and Hutchinson (1984), and Gille (1985). Substitution of the same expressions into (6.3) gives

$$\tan\psi = \frac{4\cos\omega + \sqrt{3}\,\xi\sin\omega}{-4\sin\omega + \sqrt{3}\,\xi\cos\omega}. \tag{6.14}$$

Recall that ψ is defined relative to the reference length $l = h$, and is given here for the crack tip at $y = +b$.

For large σ/σ_c, G asymptotically approaches

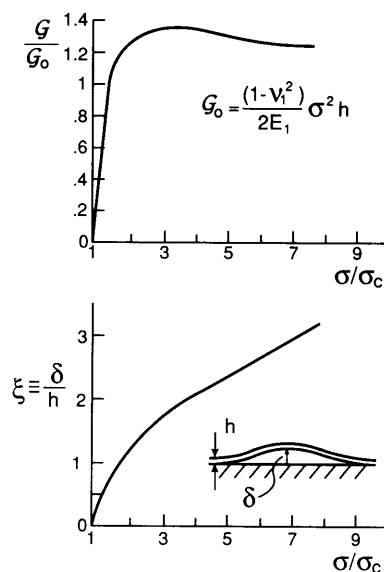$$G_0 \equiv [(1 - v_1^2)h/(2E_1)]\sigma^2. \tag{6.15}$$

FIG. 59.   Energy release rate and buckling deflection for one-dimensional blister.

This is just the strain energy per unit area in the film, which is available when released subject to the plane strain constraint $\varepsilon_x = 0$.[†] The normalized energy release rate is

$$\frac{G}{G_0} = \left(1 - \frac{\sigma_c}{\sigma}\right)\left(1 + 3\frac{\sigma_c}{\sigma}\right), \tag{6.16}$$

which is plotted in Fig. 59 together with the buckling deflection amplitude from (6.11). The interface crack length $2b$ enters the expression for G through σ_c in (6.12). For a given pre-stress σ, G approaches G_0 as $b \to \infty$; it vanishes when $\sigma_c = \sigma$; and it attains its peak value $4G_0/3$ at $\sigma/\sigma_c = 3$. The fact that G exceeds G_0 is not a violation of energy conservation. The total energy released per unit length of buckle (i.e., the integral of $2G$ with respect to b) is always less than $2G_0 b$, and only approaches $2G_0 b$ as $b \to \infty$. The explicit expression is given later in (6.35).

[†] The strain energy per unit area stored in the film is $[(1 - v_1)h/E_1]\sigma^2$. Reducing N_y to zero subject to $\varepsilon_x = 0$ releases (6.15) when negligible bending energy remains in the film. The results in (6.8)–(6.16) are valid for residual stresses for any σ_x as long as $\sigma_y = -\sigma$. They apply not only to the thin film problem but also to the x-independent mode of delamination for a surface ply on a thick composite plate.
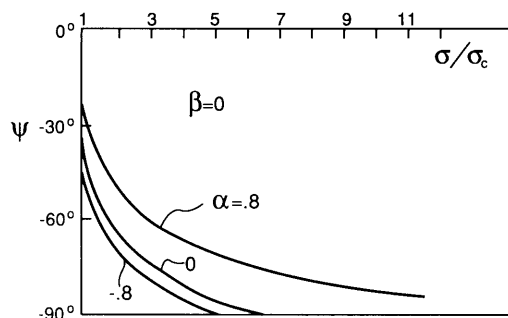
FIG. 60. Phase of loading ψ at the right-hand crack tip for the one-dimensional blister.

Curves of the mode mixity measure ψ at the right-hand crack tip are shown as a function of σ/σ_c in Fig. 60 for several values of α, all with $\beta = 0$. Elastic mismatch affects ψ only through ω in (6.14). Since ω is relatively insensitive to mismatch when $\beta = \alpha/4$ (see Fig. 58), plots of ψ versus σ/σ_c have not been displayed for this case. For σ/σ_c slightly above unity, and thus small ξ, (6.14) gives

$$\tan\psi \cong -\cot\omega, \quad \text{or} \quad \psi \cong -((\pi/2) - \omega). \quad (6.17)$$

In the absence of elastic mismatch, $\omega = 52.1°$ and ψ starts at $-37.9°$. As σ/σ_c increases and as ξ increases, the relative proportion of mode 2 to mode 1 increases. The value of σ/σ_c at which the crack tip loading becomes pure mode 2 (i.e., $\psi = -90°$) can be obtained from (6.11) and (6.14).

$$\sigma/\sigma_c = 1 + 4\tan^2\omega, \quad (6.18)$$

which is attained when $\xi = (4/\sqrt{3})\tan\omega$. Note that this point where all mode 1 is lost is a fairly strong function of elastic mismatch. For no mismatch, $\sigma/\sigma_c = 7.55$. The strong increase in mode mixity as the buckle spreads has important implications for buckle-driven decohesion, as will be discussed with the aid of several interface toughness functions in the next subsection.

Before applying the results of this section, we note in passing that the von Karman nonlinear plate equations accurately represent the buckling behavior as long as $h/b \ll 1$ and rotations satisfy $(W, y)^2 \ll 1$. Comparison of the predictions from von Karman theory with the more accurate elastica, for example, reveals that the present predictions retain reasonable accuracy for buckling deflections $W(0)$ that do not exceed $b/3$. Note from Fig. 59 or (6.11) that $W(0) = 3.46h$ when $\sigma/\sigma_c = 10$. Thus, for example, if h/b is less than about 1/10, the above predictions retain accuracy for σ/σ_c as large as 10.

3. Extent of Interface Decohesion:
The One-dimensional Blister as a Model

There is often some rate dependence associated with buckling-driven decohesion, due most likely to species in the air gaining access to the interface crack tip, a process akin to corrosion assisted crack growth. The discussion that follows will neglect any rate dependence. It will be assumed that interface crack advance occurs when the condition $G = \Gamma(\hat{\psi})$ is reached.

Consider first the consequences of assuming an ideally brittle interface where the critical energy release rate is mode-independent, i.e., $G = G_1^c$. To facilitate the discussion, assume an initial decohered region of width $2b_i$ exists on the interface, and imagine a scenario in which biaxial compressive stress in the film σ is increased, due, for instance, to temperature change when there exists a thermal expansion mismatch between the film and substrate. For a given set of parameters of the system, plot curves of G/G_1^c versus b at various levels of σ using the normalized curve in Fig. 59. Such curves are sketched in Fig. 61a, where the lowest curve corresponds to the value of σ at which the buckling starts with $b = b_i$. Denote by σ_* the value of σ associated with the curve that intersects the fracture criterion, $G/G_1^c = 1$, at $b = b_i$. In the scenario in which σ is increased, one would observe buckling without decohesion for σ between $(\sigma_c)_i$ and σ_*. At σ_*, crack advance would be initiated and would necessarily be unstable since G/G_1^c exceeds 1 as b increases. The blister would spread dynamically without arrest.

Alternatively, suppose a level of σ exists below σ_*, say $\sigma = \sigma_1$ in Fig. 61a, and suppose an external agent forces the decohered region to expand until b reaches the point where $G/G_1^c = 1$. As in the previous scenario, the crack would expand unstably from that point onward. In some previous work (e.g., Gille, 1985), it has been argued that the combination of G_1^c, b, and σ lies on the decreasing portion of the G versus b curve, thereby allowing stable crack growth. Although this is a possibility, this argument seems implausible as a general explanation because the drop from the peak to the asymptote for $b \to \infty$ is small. In fact, G increases monotonically with increasing blister radius in the case of the circular blister discussed in the next subsection; thus, there is no drop and there would be no arrest for that geometry.

The qualitative influence of the mode dependence of interface toughness on the arrest of blister spreading can be anticipated from the relation between ψ and σ/σ_c in Fig. 60. Neglect for the moment any consideration
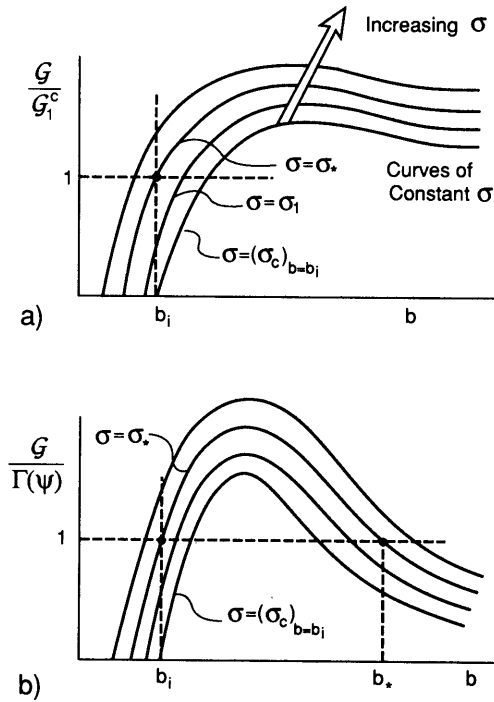
a)

b)

FIG. 61. Schematic of instability analysis of one-dimensional blister. a) based on an ideally brittle interface with propagation condition $G = G_1^c$. b) Based on $G = \Gamma(\psi)$, where Γ increases with increasing $|\psi|$.

of β-effects in the elastic mismatch, and suppose that the toughness function $\Gamma(\psi)$ increases with increasing $|\psi|$ as discussed in Section II. Then, curves of $G/\Gamma(\psi)$ versus b at various levels of σ would display the trends shown in Fig. 61b. Given an initially decohered region of width $2b_i$, the blister would spread dynamically when σ attains σ_*, and would arrest at $b = b_*$. With further increase of σ, the blister would spread stably with the condition $G = \Gamma(\omega)$ maintained. Whether it would spread beyond the point where (6.18) is attained depends on the condition governing pure mode 2 crack growth.

A quantitative prediction requires the specification of a specific functional form for $\Gamma(\psi)$. The discussion that follows will use the forms (2.40) and (2.44), which are plotted in Figs. 10 and 11, for the purpose of illustration. They will be used again in the analyses of the circular blister and the steady-state growth of the straight-sided blister. For either form, let

$$\Gamma(\psi) = G_1^c f(\psi), \qquad (6.19)$$
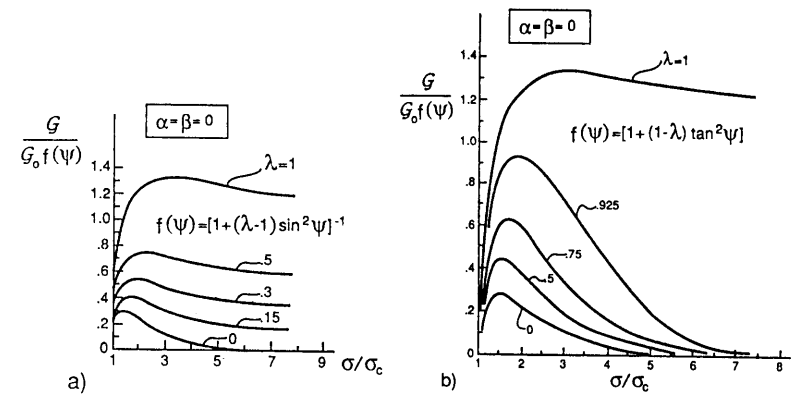
a)   b)

FIG. 62. Mode-adjusted crack driving force for the one-dimensional blister for two families of interface toughness functions. No elastic mismatch.

where

$$f(\psi) = [1 + (\lambda - 1)\sin^2\psi]^{-1} \qquad \text{for (2.40)}, \qquad (6.20)$$

$$f(\psi) = [1 + (1 - \lambda)\tan^2\psi] \qquad \text{for (2.44)}. \qquad (6.21)$$

Then, $G/f(\psi)$ can be regarded as a mode-adjusted crack driving force in the sense that the criterion for crack advance is $G/f(\psi) = G_1^c$. Curves of normalized crack driving force are plotted in Fig. 62 for various choices of λ for each of the two families of toughness functions. The curves are obtained directly using (6.16) and (6.14), and are shown for the case of no elastic mismatch ($\alpha = \beta = 0$). Recall that in each case the choice $\lambda = 1$ reduces to the ideally brittle criterion $G = G_1^c$, while $\lambda = 0$ coincides with the criterion $K_1 = K_1^c \equiv (E_* G_1^c)^{1/2}$.

The two families of interface toughness functions (6.20) and (6.21) probably bracket toughness trends for a class of material combinations, such as those discussed in Section II, in the sense that (6.20) most likely underestimates the rate of increase of $\Gamma(\psi)$ with respect to ψ near mode 2 while (6.21) probably overestimates that rate of increase. Depending on λ and the other parameters of the system, either arrest or unarrested spreading of the blister can occur according to (6.20). Arrest will always occur according to (6.21), assuming $\lambda < 1$.

The effect of elastic mismatch on the normalized driving force is shown in Fig. 63 for one choice of λ for each of the two toughness functions, in each case for various α with $\beta = 0$. A stiff film on a compliant substrate ($\alpha > 0$) enhances the peak crack driving force and accentuates its fall-off
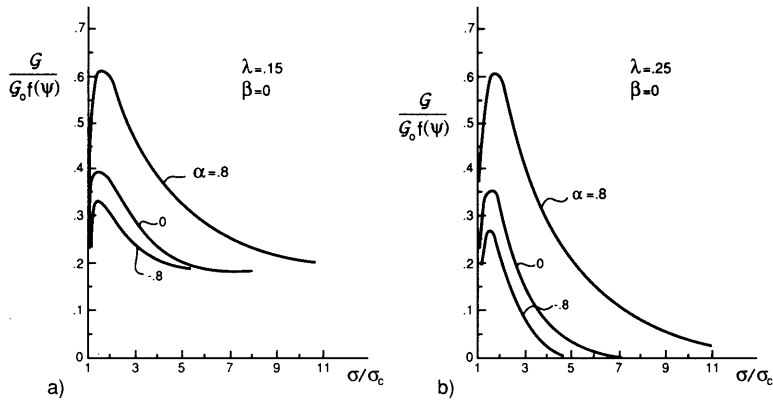
FIG. 63. Effect of elastic mismatch on the mode-adjusted crack driving force for the one-dimensional blister: (a) based on (6.20); and (b) based on (6.21).

with increasing b. When $\beta \neq 0$, the approach is similar to that just described except that now the criterion for advance is $G/f(\hat{\psi}) = G_1^c$, where $\hat{\psi}$ is associated with some material-based length $\hat{l}$ through (2.45). Since ψ in (6.14) is defined for the choice $l = h$, one must take into account the relation (2.49) between ψ and $\hat{\psi}$ in determining the crack driving force.

B. The Circular Blister

In this section, the axisymmetric counterpart to the one-dimensional blister is considered. An analysis along similar lines to that presented here was given by Chai (1990) for the special case where no elastic mismatch exists between the film and the substrate. The geometry for the circular blister is similar to that in Fig. 57 except that the radius of the buckled region is taken to be R. The analysis again couples a buckled plate representing the circular decohered region of the film with the elastic solution for a semi-infinite edge crack on an interface, as depicted in Fig. 57 and as presented in Section VI.A.1. For the axisymmetric geometry, the nonlinear von Karman plate equations cannot be solved in closed form, except asymptotically for sufficiently small buckling amplitudes. Numerical methods must be used to solve the equations for the buckled plate.

1. Governing Equations

The von Karman nonlinear plate equations for axisymmetric deformations of a completely clamped circular plate of radius R, thickness h, and

subject to an equi-biaxial compressive stress σ in the unbuckled state are as follows. Let r be the distance from the center of the plate normalized by R, $N_r(r)$ the resultant radial in-plane stress, $\Delta N_r(r) \equiv N_r(r) + \sigma h$ the change in this component from its value in the unbuckled state, and let $W(r)$ be the vertical displacement component. With

$$\phi(r) = [6(1 - v_1^2)]^{1/2} h^{-1} \frac{dW}{dr} \tag{6.22}$$

as a measure of the rotation, the two equations of equilibrium can be written in nondimensional form as

$$\frac{d}{dr}\left(r\frac{d\phi}{dr}\right) - r^{-1}\phi + r\phi(\bar{\sigma} - \Delta \bar{N}_r) = 0, \tag{6.23}$$

$$\frac{d}{dr}\left(r^3 \frac{d\Delta \bar{N}_r}{dr}\right) + r\phi^2 = 0, \tag{6.24}$$

where $\bar{\sigma} = \sigma h R^2/D$ and $\Delta \bar{N}_r = \Delta N_r R^2/D$. As before, $D = E_1 h^3/[12(1 - v_1^2)]$ is the bending stiffness. The conditions at $r = 0$ are $\phi = 0$ and $d\Delta \bar{N}_r/dr = 0$. The fully clamped conditions at $r = 1$ require

$$\phi = 0, \qquad \frac{d}{dr}(r\Delta \bar{N}_r) - v_1 \Delta \bar{N}_r = 0. \tag{6.25}$$

The energy release rate, interface stress intensity factors, and mode mixity parameter in (6.1)–(6.3) are evaluated using the bending moment and the change in resultant stress at the edge of the plate, which are given by

$$M = DhR^{-2}[6(1 - v_1^2)]^{-1/2}(d\phi/dr)_{r=1},$$
$$\Delta N = DR^{-2}(\Delta \bar{N}_r)_{r=1}. \tag{6.26}$$

2. Asymptotic Solution for Small Buckling Deflections

Evans and Hutchinson (1984) derived a formula for the energy release rate using an asymptotically valid solution to the preceding system of equations for small buckling deflections. That result will be reproduced here without derivation along with a new companion result for the mode mixity parameter ψ.

The classical buckling stress of a clamped circular plate is

$$\sigma_c^* = \frac{\mu^2 D}{R^2 h} = 1.2235 \frac{E_1}{1 - v_1^2}\left(\frac{h}{R}\right)^2, \tag{6.27}$$

Where $\mu = 3.8317$ is the first nontrivial zero of $J_1(x)$, the Bessel function of the first kind of order one. The associated axisymmetric mode is

$$W_1(r) = [0.2871 + 0.7129J_0(\mu r)]h, \qquad (6.28)$$

where $J_0(x)$ is the Bessel function of the first kind of order zero. The mode is normalized such that $W_1(0) = h$.

The asymptotic solution is obtained by developing an expansion of the buckling deflection (and other quantities) in the form

$$W(r) = \xi W_1 + \xi^2 W_2 + \cdots, \qquad (6.29)$$

where ξ is the buckling amplitude. To lowest order, $\xi = \delta/h$, where δ is the deflection at the center of the plate. The asymptotic relation between ξ and σ/σ_c^* is

$$\xi = \left[\frac{1}{c_1} \left(\frac{\sigma}{\sigma_c^*} - 1 \right) \right]^{1/2}, \qquad (6.30)$$

where $c_1 = 0.2473(1 + \nu_1) + 0.2231(1 - \nu_1^2)$. The asymptotic result for the energy release rate is

$$\frac{G}{G_0^*} = c_2 \left[1 - \left(\frac{\sigma_c^*}{\sigma} \right)^2 \right], \qquad (6.31)$$

where $c_2 = [1 + 0.9021(1 - \nu_1)]^{-1}$ and

$$G_0^* = (1 - \nu_1)h\sigma^2/E_1 \qquad (6.32)$$

is the strain energy per unit area stored in the unbuckled film.[†] The asymptotic relation between the mode mixity parameter for the interface crack and the buckling deflection is

$$\tan \psi = \frac{\cos \omega + 0.2486(1 + \nu_1)\xi \sin \omega}{-\sin \omega + 0.2486(1 + \nu_1)\xi \cos \omega}. \qquad (6.33)$$

For sufficiently small ξ, ψ approaches (6.17), just as in the case of the one-dimensional blister. The asymptotic results are shown in Figs. 64 and 65, where they are compared with the results of an accurate numerical analysis described next.

[†] The expression for c_2 given here corrects the coefficient given by Evans and Hutchinson (1984). Their derivation made use of a result for the initial post-buckling behavior of a clamped circular plate given in the text by Thompson and Hunt (1973), which does not correctly account for the Poisson's ratio dependence. The present result incorporates the corrected solution. The difference between c_2 and the earlier result of Evans and Hutchinson is less than 1% for $\nu_1 = 0.3$.
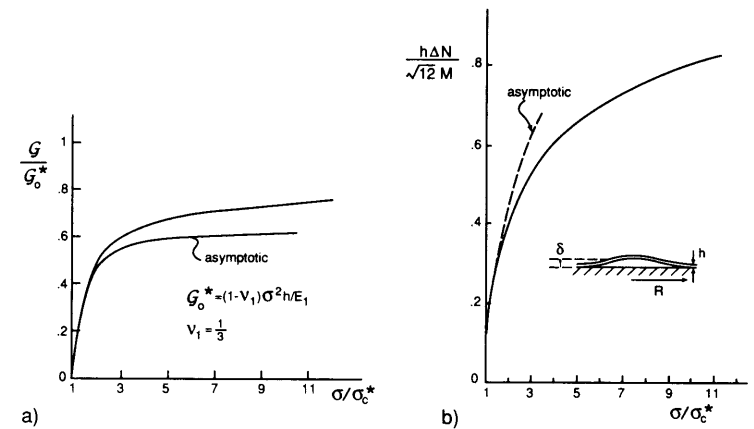
FIG. 64. Energy release rate and edge loading ratio for the circular blister.
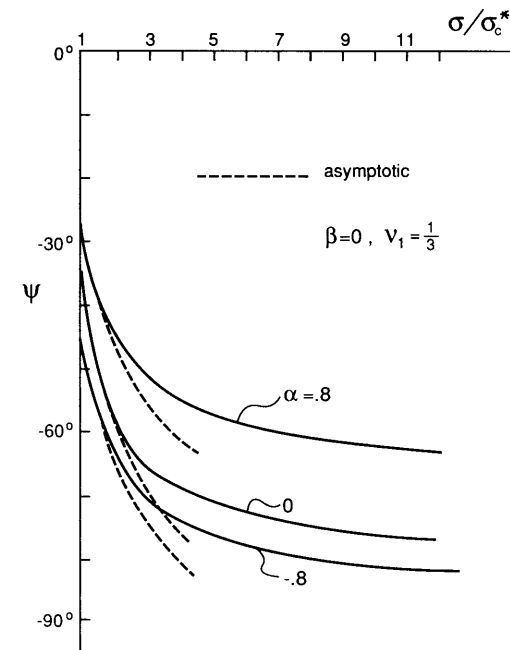

FIG. 65. Phase of loading ψ at interface crack tip for the circular blister for three levels of elastic mismatch.
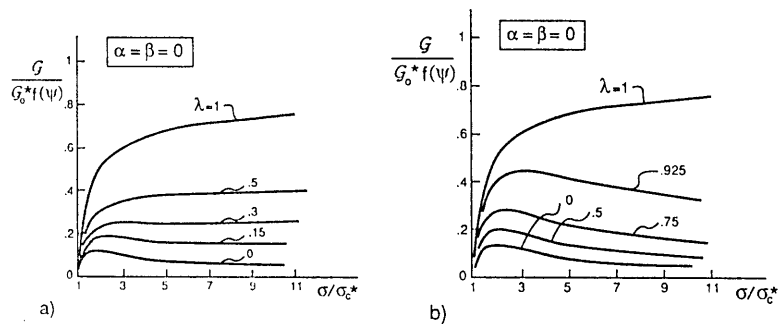
Fig. 66. Mode-adjusted crack driving force for the circular blister: a) based on (6.20); and b) based on (6.21).

3. *Numerical Solution for Arbitrarily Large Buckling Deflections*

An accurate finite difference method was used to solve the coupled ordinary differential equations (6.23) and (6.24), subject to the stated boundary conditions. Newton iteration was used to obtain a converged solution for each specified value of σ/σ_c^*. All calculations were carried out with $\nu_1 = 1/3$. The results for the quantities of interest are shown in Figs. 64–66. The results for G are in agreement with calculated results of Yin (1985) and Chai (1990), while the present results for ψ for the case of no elastic mismatch are in accord with the trends of G_1 and G_2 presented by Chai. Note that the curve for $h \Delta N/(\sqrt{12}M)$ in Fig. 64 permits ψ to be computed using (6.3) for any elastic mismatch.

The energy release rate of the interface crack increases monotonically with increasing R (decreasing σ_c^*) for the circular blister, as can be seen in Fig. 64. Its approach to G_0^* is very slow. At $\sigma/\sigma_c^* = 50$, $G/G_0^* \cong 0.85$ (not shown in plot). The asymptotic formula (6.31) is reasonably accurate for σ/σ_c^* up to about 3. The asymptotic formula (6.30) for δ/h retains its accuracy to surprisingly large values of σ/σ_c^*. A plot of δ/h is not shown, but, with $\xi \equiv \delta/h$, (6.30) overestimates the accurate numerical result at $\sigma/\sigma_c^* = 10$ by only 7%. As in the case of the one-dimensional blister, buckling deflections that are large compared to the film thickness imply residual stresses that are many times the classical buckling stress σ_c^* of the corresponding plate of film. The asymptotic formula (6.33) for ψ is also valid for values of σ/σ_c^* up to about 2 or 3, as can be seen in Fig. 65. However, ψ does not vary as strongly with σ/σ_c^* for the circular blister as for the one-dimensional blister (*cf.* Fig. 60), a feature also emphasized by Chai (1990). In particular, the interface crack of the circular blister does not

attain pure mode 2 in the range of σ/σ_c^* shown, as its one-dimensional counterpart does. Even for σ/σ_c^* as large as 50, some mode 1 persists with $\psi = -84°$ for $\alpha = \beta = 0$. This feature may be at the heart of why growth of the blisters is favored along a curved front rather than a straight one.

Plots of the normalized crack driving force $G/[G_0^* f(\psi)]$ are shown in Fig. 66 for the same two interface toughness functions, (6.20) and (6.21), used to construct the plots for the one-dimensional blister in Fig. 62. For reasons noted previously, the crack driving force does not fall off nearly as rapidly as the blister spreads as for the one-dimensional blister. The fact that circular blisters have been observed for some systems is indirect evidence for an interface toughness function that increases sharply with increasing mode 2, such as that used in constructing the curves in Fig. 66b.

4. *Tendency toward Spalling as the Blister Spreads*

Circular spalls are observed in some systems where the film is brittle. Evidently, the radius of the blister increases until it reaches a point where the crack kinks out of the interface into the film, spalling out a circular patch of film. The mixed mode conditions at the tip of the interface crack derived in the previous sections contribute to the likelihood of this type of spalling in two ways. First, with reference to the kinking solution in Section II.C.5, one notes that kinking upward into the film is favored energetically as ψ becomes more negative, with the largest value of G_{max}^t/G attained at $\psi \cong -60°$. Secondly, as the blister spreads and as $|\psi|$ increases, the G needed to advance the interface crack increases, assuming $\Gamma(\psi)$ increases with increasing $|\psi|$. Thus, as the blister spreads, the maximum energy release rate available for a crack kinking into the film, G_{max}^t, increases. Kinking, and spalling, is to be expected if G_{max}^t attains the fracture toughness of the film.

C. CONDITIONS FOR STEADY-STATE PROPAGATION OF A STRAIGHT-SIDED BLISTER

An example of the straight-sided blister is shown in Fig. 56 and is sketched in Fig. 67b. Under steady-state conditions, the width of the blister remains fixed and the growth occurs by interface crack advance along the more-or-less circular end of the blister. An approximate analysis of the conditions for steady-state blister propagation is given.
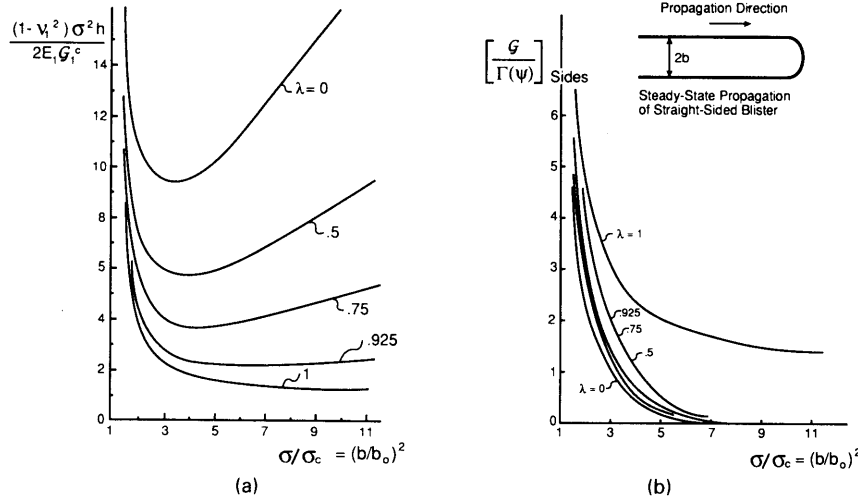
FIG. 67. a) Condition for steady-state propagation of straight-sided blister for the interface toughness function (6.21). b) Mode-adjusted crack driving force on the sides of the straight-sided blister. The condition that the sides are in an arrested state is $G/\Gamma(\psi) < 1$.

Under steady-state conditions, the total energy released per unit advance of the blister is precisely the energy released by a unit length of the one-dimensional blister of Section B.2 in spreading from the smallest width for which the buckle has nonzero amplitude, $2b_0 = 2\pi[D/(\sigma h)]^{1/2}$, to $2b$. Thus, the *average steady-state* energy release rate of the advancing end is

$$G_{ss} = b^{-1} \int_{b_0}^{b} G \, db, \qquad (6.34)$$

where G is given by (6.16). Noting that σ_c depends on b according to (6.12), one readily obtains

$$G_{ss} = \left(1 - \frac{\sigma_c}{\sigma}\right)^2 G_0. \qquad (6.35)$$

It is also useful to note that $b_0/b = (\sigma_c/\sigma)^{1/2}$.

An exact propagation condition would require that G_{ss} be equal to the average of the interface toughness $\Gamma(\psi)$ across the propagating end of the blister. This, in turn, would require knowledge of the precise distribution of ψ across the end of the blister. As an approximation, take

$$G_{ss} = \Gamma(\psi^*), \qquad (6.36)$$

where ψ^* is the mode mixity parameter for a full circular blister of radius b subject to the same biaxial stress σ. To see how this generates specific predictions, again represent the interface toughness function as

$$\Gamma(\psi) = G_1^c f(\psi), \qquad (6.37)$$

and rewrite the propagation condition (6.36), using (6.35) and (6.15), as

$$\frac{G_0}{G_1^c} \equiv \frac{(1 - \nu_1^2)\sigma^2 h}{2E_1 G_1^c} = \left(1 - \frac{\sigma_c}{\sigma}\right)^{-2} f(\psi^*). \qquad (6.38)$$

The right-hand side of this equation is a function of σ/σ_c since ψ^* is a function of σ/σ_c^* (cf. Fig. 65) and $\sigma_c^*/\sigma_c = 1.4876$.

The right-hand side of (6.38) is plotted in Fig. 67a for a choice of $f(\psi)$ used previously, (6.21), for several values of λ. These curves were computed using the solid line curve for ψ^* versus σ/σ_c^* in Fig. 6.10 for the case $\alpha = \beta = 0$ with $\nu_1 = 1/3$. Recall that $\lambda = 0$ corresponds to the interface fracture criterion $K_1 = K_1^c$, while $\lambda = 1$ corresponds to the Griffith criterion $G = G_1^c$. To interpret these curves, it is helpful to present results that display whether or not the parallel sides are in a state consistent with interface crack arrest. For this purpose, the ratio $G/\Gamma(\psi)$ holding on the sides is plotted as a function of σ/σ_c in Fig. 67b, where G is given by (6.16) and ψ is given by (6.14) for the straight-sided blister. The combination of (6.16) and (6.38) gives

$$\frac{G}{\Gamma(\psi)} = \left(1 - \frac{\sigma_c}{\sigma}\right)^{-1} \left(1 + 3\frac{\sigma_c}{\sigma}\right) \frac{f(\psi^*)}{f(\psi)}, \qquad (6.39)$$

which is the expression used in plotting the curves in Fig. 67b. The fact that $G/\Gamma(\psi) \to 0$ at $\sigma/\sigma_c = 7.55$ for all $\lambda < 1$ is a consequence of unbounded mode 2 toughness assumed in connection with the choice (6.21) for $f(\psi)$.

Consider the curves in Fig 67 for one of the λ-values such that $\lambda < 1$. Note that $[G/\Gamma(\psi)]_{sides} < 1$ for all values of σ/σ_c greater than or equal to its value at the minimum of $(1 - \nu_1^2)\sigma^2 h/(2E_1 G_1^c)$. Thus, the sides of the blister are in a state consistent with interface crack arrest everywhere to the right of the minimum in Fig. 67a. By contrast, $[G/\Gamma(\psi)]_{sides}$ exceeds unity for nearly all σ/σ_c to the left of the minimum, implying a lack of consistency with arrest of the sides. One concludes that the relevant branch of each of the curves for $\lambda < 1$ in Fig. 67a is that to the right of the minimum. (The transition $G/\Gamma(\psi)$ so near the minimum may be somewhat fortuitous since the solution is not exact.)

For a particular λ ($\lambda < 1$), the *smallest* value σ consistent with steady-state propagation is given by

$$\frac{(1 - v_1^2)\sigma^2 h}{2E_1 G_1^c} = c(\lambda),\qquad (6.40)$$

where $c(\lambda)$ denotes the value of the ordinate in Fig. 67a at the minimum. Equivalently, if σ is regarded as prescribed, (6.40) gives the smallest value of film thickness h consistent with steady-state propagation. The half-width of the blister associated with (6.40) is

$$\frac{b}{h} = \frac{\pi}{2\sqrt{3}} \left\{ \frac{d(\lambda)}{[2c(\lambda)]^{1/2}} \right\}^{1/2} \left[\frac{E_1 h}{(1 - v_1^2)G_1^c} \right]^{1/4},\qquad (6.41)$$

where $d(\lambda)$ is the value of σ/σ_c at the minimum.

For film stresses σ larger than the minimum in (6.40), or for film thicknesses h larger than the minimum, solutions exist on the branch to the right of the minimum of the curves in Fig. 67a. The associated width of the blister increases with increasing σ. Equation (6.41) continues to apply with (d, c) denoting a point on the curve in Fig. 67a. From a practical standpoint, the minimum is probably of the most interest. For a film stress less than the minimum (or a film thickness less than the minimum), extensive propagation of an initial blister can be avoided.

The behavior associated with the interface fracture criterion $G = G_1^c$ (i.e., $\lambda = 1$) must be discussed separately. From Fig. 67a, one notes that there exists a propagation solution for all values of $(1 - v_1^2)\sigma^2 h/(2E_1 G_1^c)$ greater than unity. But, from Fig. 67b, one sees that these solutions are inconsistent with arrest of the interface crack along the sides. Thus, it must be concluded that there exist no steady-state straight-sided blister solutions when the classical criterion $G = G_1^c$ is presumed to hold.

The particular interface toughness function, (6.37) with (6.21), was invoked to illustrate the calculation procedures for steady-state blister propagation and to bring out some of its qualitative features. The example reveals that steady-state blister propagation, as opposed to complete decohesion of the film, is innately tied to the property of the toughness function wherein it increases with increasing proportion of mode 2. Details of the propagation of the straight-sided blister do depend on the specifics of $f(\psi)$. For example, the previous calculations were repeated using (6.20) rather than (6.21). The function $f(\psi)$ in (6.20) levels off as

$|\psi|$ approaches $\pi/2$ as opposed to (6.21), which increases sharply as the mixity approaches pure mode 2. Only for a fairly small range of λ (i.e., $0 \le \lambda < 0.15$) does there exist a steady-state solution satisfying the conditions discussed in the preceding. For λ in the range $0.15 < \lambda \le 1$, no solutions exist consistent with interface crack arrest along the straight sides. Whether solutions exist in this range that are characteristic of the telephone cord morphology (*cf.* Fig. 56) is not known. The answer to this question would obviously shed light on the nature of the interface toughness function.

We end this section with some additional speculation on the possible origin of the telephone cord morphology of blister propagation. The approximate solution for the straight-sided blister does not address the issue of the stability of the configuration. For example, is the symmetric configuration (symmetric with respect to the line parallel to, and centered between, the straight sides) stable with respect to nonsymmetric perturbations of the interface crack front? One possibility is that, at sufficiently large values of $(1 - v_1^2)\sigma^2 h/(2E_1 G_1^c)$, the steady-state straight-sided configuration becomes unstable. Partial support for this speculation comes from stability results for the circular blister (unpublished work in progress). The circular blister becomes unstable to nonaxisymmetric perturbations of the interface crack front at sufficiently large σ. The value of σ/σ_c^* at which this instability occurs depends on the choice of $\Gamma(\psi)$, but is typically at or above the value associated with the minimum of $(1 - v_1^2)\sigma^2 h/(2E_1 G_1^c)$ in the steady-state problem.

VII. Blister Tests

The blister test is used to measure interface toughness for a crack on the interface between a film and a substrate. The test avoids edge effects of various kinds and is highly stable. Although mixed mode conditions prevail at the tip of the interface crack, most approaches to the subject have concentrated on the relation between the energy release rate and the various parameters of the test (Liechti, 1985; and Storakers, 1988). Recent work by Chai (1990) and Jensen (1990) has elucidated the mixed mode character of the test using an approach similar to that described in the previous section. The separated blister is treated by plate theory and is coupled to the 2-layer edge crack solution of Section VI.A.1 to give G and ψ. The results that follow are taken from Jensen (1990).

A. PRESSURE LOADING

A circular blister loaded by a pressure p acting between the film and substrate is depicted in cross-section in the insert in Fig. 68. The film is modeled as a clamped plate of radius R subject to lateral pressure p. At small deflections, within the linear range, the moment at the edge of the plate is

$$M = \tfrac{1}{8}pR^2, \qquad (7.1)$$

and the deflection δ at the center of the plate is

$$\delta = \tfrac{1}{64}pR^4/D. \qquad (7.2)$$

The resultant in-plane stress N is of order p^2. Thus, for sufficiently small p, by (6.1) and (7.1),

$$G = \frac{3}{32}\frac{(1 - \nu_1^2)}{E_1 h^3}p^2R^4 = \frac{8}{3}\frac{E_1 h^3 \delta^2}{(1 - \nu_1^2)R^4} \qquad (7.3)$$

and, by (6.3),

$$\tan\psi = -\cot\omega \quad \Rightarrow \quad \psi = -((\pi/2) - \omega). \qquad (7.4)$$

This is the same combination of mode 1 and 2 that exists for the buckled blisters at small buckling deflections. As in those problems, ψ is defined here with $l = h$. Equation (7.4) is valid for sufficiently small p even in the presence of an initial pre-stress in the film since the change in membrane stress, ΔN, at the edge of the plate is of order p^2. However, the range of applicability of the formula will depend on the residual stress level.
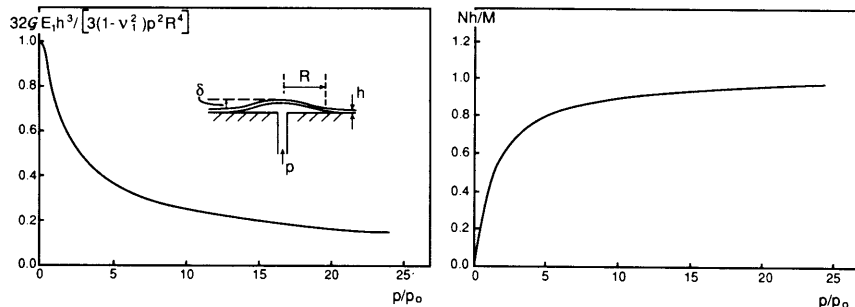

FIG. 68.   Energy release rate and ratio of edge loads for a blister under uniform pressure.

There are only a few results in the literature based on rigorous 3-D elasticity solutions that permit a direct assessment of the approximate procedure that couples the plate solution to the 2-layer edge crack solution. Kamada and Higashida (1979) present results for K_1 and K_2 for the case of no elastic mismatch, based on a full elasticity solution to the circular blister loaded by uniform pressure. They find that $\psi = -30°$ for $R/h = 5$ and $\psi = -37°$ for $R/h = 10$. This can be compared with $\psi = -37.9°$ from (7.4) when $\alpha = \beta = 0$. Thus, their results suggest that the approximate procedure is accurate for R/h as small as 10. Erdögan and Arin (1972) have presented results for a penny-shaped blister crack on an interface between materials with the mismatch characteristic of epoxy and aluminum, but a numerical comparison with the present results is not meaningful since the largest value of R/h for which they have reported results is 2.5.

Calculations for G and ψ at large deflections have been carried out by Chai (1990) and Jensen (1990) using the nonlinear von Karman plate equations for the case of no residual pre-stress. Results from Jensen are given in Fig. 68 as plots of a nondimensional G and Nh/M versus p/p_0, where N is the resultant in-plane radial stress at the edge of the plate and

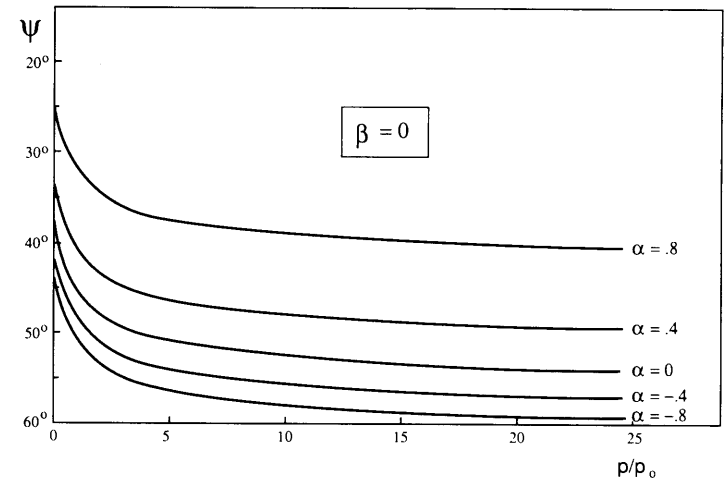$$p_0 = \frac{16}{3}\frac{E_1}{(1 - \nu_1^2)}\left(\frac{h}{R}\right)^4. \qquad (7.5)$$

FIG. 69.   Phase of loading of interface crack tip for several levels of elastic mismatch for a blister under uniform pressure.
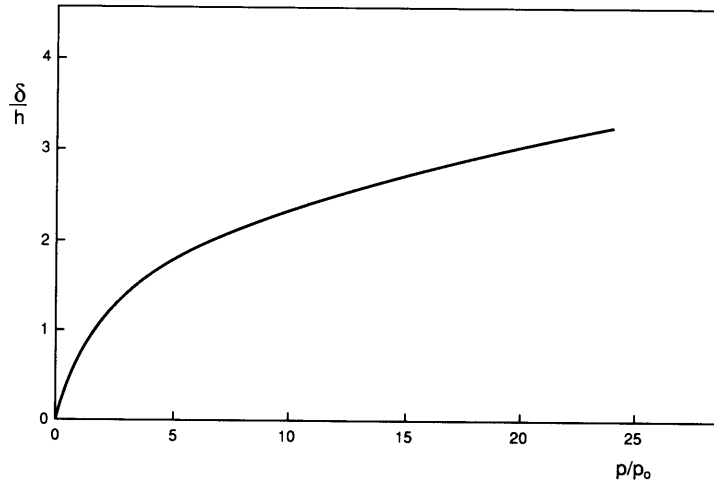
FIG. 70.   Deflection-pressure relation for a blister under uniform pressure.

The ratio Nh/M is the basic information needed in (6.3) (with $\Delta N \equiv N$) to generate ψ for any elastic mismatch between the film and substrate. The curves of ψ versus p/p_0 are plotted in Fig. 69 for various α with $\beta = 0$. As p increases, the ratio Nh/M increases giving rise to an increasing proportion of mode 2 to mode 1. The increase only entails a change of ψ of about 15°. For completeness, curves of δ/h versus p/p_0 are shown in Fig. 70. The curves in these figures were computed with $v_1 = 1/3$, but they are only weakly dependent on v_1.
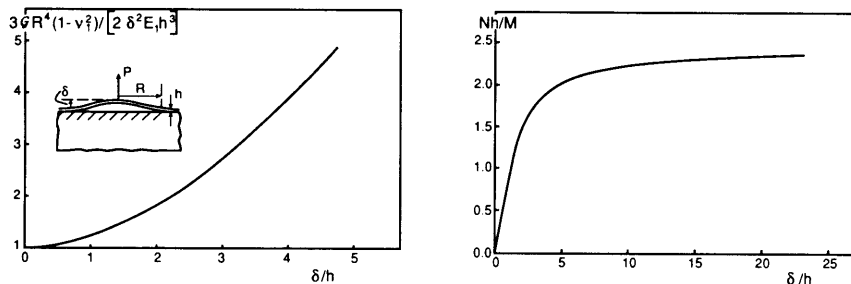

FIG. 71.   Energy release rate and ratio of edge loads for a blister under point load.

B. Point Loading

The theoretical predictions for a circular blister loaded by a concentrated load P at its center (see insert in Fig. 71) have also been computed by Jensen (1990). In the linear range, the moment at the edge of the clamped plate is

$$M = \frac{1}{4\pi}P, \tag{7.6}$$

and the center deflection is

$$\delta = \frac{3(1 - v_1^2)PR^2}{4\pi E_1 h^3}. \tag{7.7}$$

Then, by (6.1),

$$G = \frac{2E_1 h^3 \delta^2}{3(1 - v_1^2)R^4}, \tag{7.8}$$

and ψ is again given by (7.4). Curves of a nondimensional G and Nh/M versus δ/h for arbitrarily large δ/h are shown in Fig. 71. Curves of ψ versus δ/h are given in Fig. 72 for various α with $\beta = 0$. The mode dependence is similar to that for the pressurized blister, except with a somewhat larger change in ψ as the deformation becomes nonlinear. The dependence of δ/h on P is plotted in Fig. 73. All these results were computed with $v_1 = 1/3$, and initial residual stress is not included.
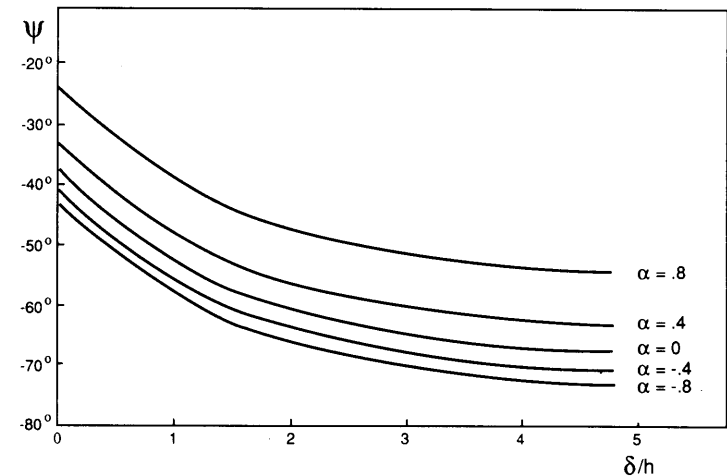

FIG. 72.   Phase of loading of interface crack tip for several levels of elastic mismatch for a blister under point load.
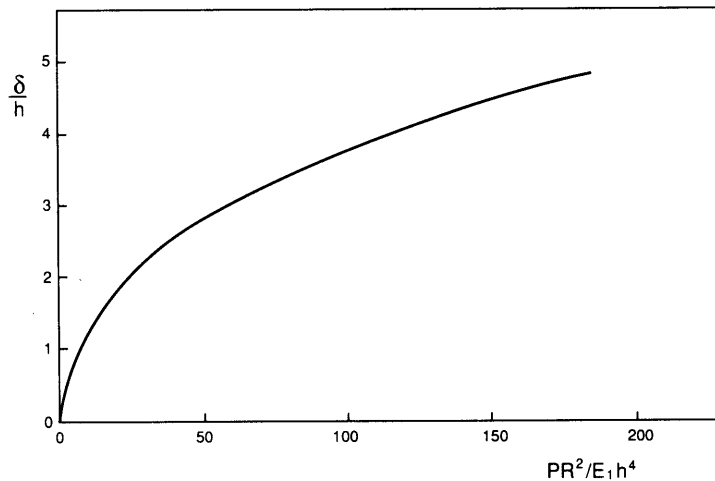
FIG. 73.   Deflection–load relation for a blister under point load.

VIII. Failure Modes of Brittle Adhesive Joints and Sandwich Layers

This final section focuses down to a finer scale than has hitherto been addressed in most of this chapter. Attention is directed to modes of cracking of a thin, brittle adhesive layer joining two identical bulk solids. The discussion also has bearing on sandwich specimens, such as those discussed in Section IV.C, which are designed to measure toughness of the interface between the thin layer material and the adjoining material comprising the bulk of the specimen. Figure 74 shows one such sandwich specimen. Below it, at higher magnification, are depicted some of the multitude of cracking morphologies that have been observed in brittle systems. A test series carried out using any such sandwich specimen provides the macroscopic, or effective, interface toughness function $\bar{\Gamma}(\psi)$ characterizing the joint. In assessing the effectiveness of a joint or in making engineering applications, one need not necessarily be concerned with the local cracking morphology. On the other hand, $\bar{\Gamma}(\psi)$ itself may be a strong function of the cracking morphology, and, if so, it is essential to understand what controls the local cracking morphology in any attempt to improve the quality of the joint. Similarly, attempts to measure the interface toughness $\Gamma(\psi)$ between two materials using a sandwich specimen can be defeated by tendencies for an interface crack to misbehave in one of the other modes of cracking.
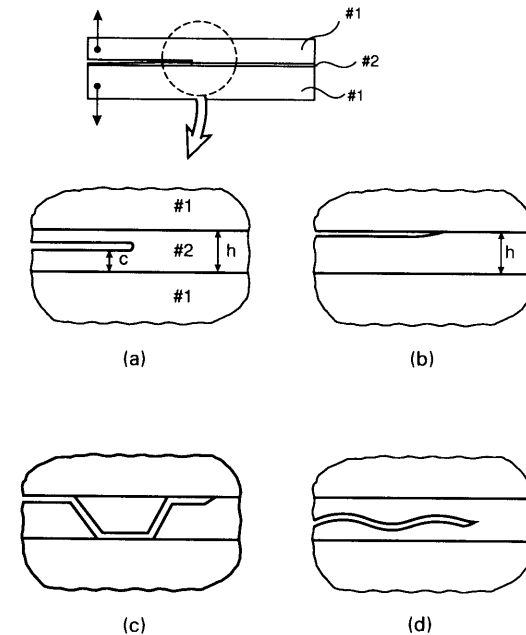
FIG. 74.   Modes of cracking in a thin, brittle adhesive layer: (a) straight crack within layer; (b) interface crack; (c) alternating crack; (d) wavy crack.

This section addresses some of the many issues surrounding local cracking morphology. The discussion is restricted to brittle systems for which any inelastic behavior occurs on a scale that is small compared with the layer thickness h. The layer thickness is assumed to be very small compared with the in-plane dimensions of the joint or of the sandwich specimen. At the macroscopic level, the tip of a crack along the joint or layer is characterized by macroscopic, or applied, stress intensity factors K_I^∞ and K_{II}^∞. As discussed in Section IV, these are determined from a standard analysis that ignores the existence of the thin layer. The macroscopic energy release rate is

$$G^\infty = \bar{E}_1^{-1}(K_I^{\infty 2} + K_{II}^{\infty 2}), \qquad (8.1)$$

where the numbering for the materials is shown in Fig. 74. The effective toughness function of the joint as determined in a test is identified with the critical value of the overall energy release rate at crack advance according to

$$\bar{\Gamma}(\psi^\infty) = G_c^\infty, \qquad (8.2)$$

where $\psi^\infty = \tan^{-1}(K_{II}^\infty/K_I^\infty)$.

A. Basic Results for Straight Cracks

1. Straight Crack within the Layer (Fig. 74a)

A simple energy argument or application of the J-integral establishes the equality of G^∞ and the local energy release rate at the tip, G. With K_I and K_{II} as the local stress intensity factors, $G = \bar{E}_2^{-1}(K_I^2 + K_{II}^2)$. The condition $G = G^\infty$, together with (8.1) and linearity in the relation between stresses, allows one to write the connection between the local and applied stress intensity factors such as

$$(K_I + iK_{II}) = \left(\frac{1 - \alpha}{1 + \alpha}\right)^{1/2}(K_I^\infty + iK_{II}^\infty)e^{i\phi(c/h, \alpha, \beta)}. \qquad (8.3)$$

Here, $\phi = \psi - \psi^\infty$ is the shift in the phase angle between the local and applied intensities. Fleck $et\ al.$ (1991) have carried out calculations for ϕ; they give the approximation

$$\phi = \varepsilon \ln\left(\frac{h}{c} - 1\right) + 2\left(\frac{c}{h} - \frac{1}{2}\right)\tilde{\phi}(\alpha, \beta), \qquad (8.4)$$

where $\tilde{\phi}$ is plotted in Fig. 75. This result is unaffected by the presence of a residual stress $\sigma_{11} \equiv \sigma_R$ in the layer.

If the macroscopic specimen is loaded in mode I ($K_{II}^\infty = 0$) and if the crack does propagate down the centerline of the layer ($cf.$ discussion in next subsection), then (8.3) gives $K_{II} = 0$ and

$$K_I = \left(\frac{1 - \alpha}{1 + \alpha}\right)^{1/2}K_I^\infty. \qquad (8.5)$$
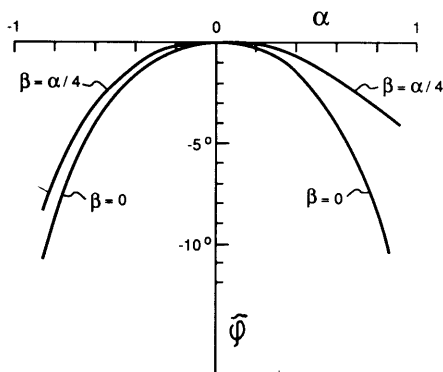

FIG. 75.   Phase factor $\tilde{\phi}(\alpha, \beta)$ in (8.4).

This result, which was obtained originally by Wang $et\ al.$ (1978), reveals that a crack within a compliant layer ($\alpha > 0$) is shielded. With K_{Ic} as the intensity toughness of the layer material, the $apparent\ toughness$ measured using the sandwich specimen is

$$K_{Ic}^\infty = \left(\frac{1 + \alpha}{1 - \alpha}\right)^{1/2}K_{Ic}. \qquad (8.6)$$

An equivalent statement concerning the elastic shielding is that the load needed to fracture the sandwich specimen differs from that needed to fracture a geometrically similar specimen made entirely from the layer material by the factor $[(1 + \alpha)/(1 - \alpha)]^{1/2}$. This factor can be quite large when a stiff material is joined by a compliant adhesive, as is the case when, for example, metal of ceramic parts are joined by a polymer adhesive. If the strength of a joint is controlled by crack-like flaws that are on the order of the adhesive thickness or somewhat larger, then this same magnification factor will apply to the strength of the joint compared to the strength of the bulk adhesive with flaws of similar size. If the controlling flaws are much smaller than the layer thickness, the magnification effect is lost.

3. Crack along the Interface (Fig. 74b)

The relation $G^\infty = G$ also holds for this case, where G is related to the interfacial stress intensity factors K_1 and K_2 by (2.29). The equation relating K_1 and K_2 to K_I^∞ and K_{II}^∞ is (3.38) with $K_1 \equiv K_I^\infty$ and $K_{II} \equiv K_{II}^\infty$. With ψ for the tip on the interface defined by (2.45) with $l = h$, the ω-quantity in (3.38) is $\psi - \psi^\infty$. This shift in phase is generally small and even for the largest elastic mismatches never more than about $15°$.

As discussed in Section IV.C, sandwich specimens are attractive for measuring interface toughness. Assuming the crack does advance in the interface, the equation for the interfaces toughness function is simply

$$\Gamma(\psi, l = h) = \bar{\Gamma}(\psi^\infty), \qquad (8.7)$$

where $\psi = \psi^\infty + \omega$. Conversion of $\Gamma(\psi, h)$ to $\Gamma(\hat{\psi}, \hat{l})$ where $\hat{\psi}$ is defined using a material-based length $\hat{l}$ is readily carried out as specified by (2.51).

B. Crack Trapping in a Compliant Layer under Nonzero K_{II}^∞

Equation (8.3) predicts a strong trapping effect due to elastic mismatch between the layer and the adjoining blocks. When K_{II}^∞ is not too large
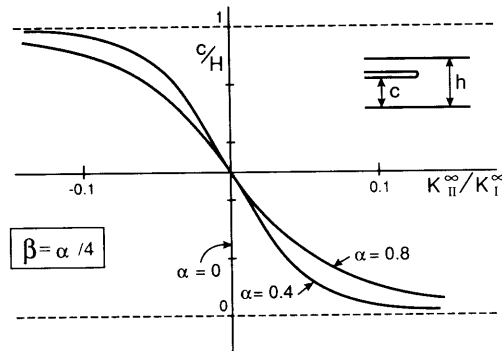
FIG. 76.   Location of trapped crack in a compliant sandwich layer.

compared to K_I^∞, (8.3) reveals the existence of a straight, mode I crack path within the layer. The condition for $K_{II} = 0$ from (8.3) gives the relation between the location of the crack, c/h, and ψ^∞ as

$$\phi(c/h, \alpha, \beta) = -\psi^\infty. \qquad (8.8)$$

Since ϕ vanishes when the elastic mismatch vanishes, there can be no straight crack paths within the layer unless $\psi^\infty = 0$ under this circumstance. A plot of the solution to (8.8) is shown in Fig. 76 for several levels of mismatch, all with $\beta = \alpha/4$. When there is significant mismatch, a mode I path well within the layer can exist for $|K_{II}^\infty|$ as large as 10% of K_I^∞. Such paths exist whether the layer is compliant or stiff, but generally a straight crack in a stiff layer will be configurationally unstable, as will now be discussed.

C. CONFIGURATIONAL STABILITY OF A STRAIGHT CRACK WITHIN THE LAYER

Given the existence of a straight mode I path within the layer, the issue now addressed is whether the path will be insensitive to small perturbations, returning to the straight trajectory, or will be deflected into the interface or possibly into a wavy morphology. Consider a loading with $K_{II}^\infty = 0$ such that the center line through the layer is a mode I crack trajectory. Two results are presented that indicate whether or not the centerline path is configurationally stable.

First, suppose at the start of propagation the crack lies off the centerline (i.e., $c/h \neq 1/2$ in Fig. 74a). From (8.3), with $K_{II}^\infty = 0$,

$$K_{II} = [(1 - \alpha)/(1 - \alpha)]^{1/2} \sin \phi \, K_I^\infty. \qquad (8.9)$$

The offset crack will kink *toward* the centerline if $K_{II} > 0$ when $c/h > 1/2$, and if $K_{II} < 0$ when $c/h < 1/2$. The function ϕ given by (8.4) is odd with respect to the centerline at $c/h = 1/2$. For a compliant layer ($\alpha > 0$) with $\beta = \alpha/4$, ϕ is positive when $c/h > 1/2$, implying by (8.9) that the crack will kink toward the centerline. By contrast, when the layer is stiff ($\alpha < 0$), ϕ is negative when $c/h > 1/2$ and the crack will kink *away* from the centerline. A compliant layer with $\beta = 0$ has a small negative ϕ when $c/h > 1/2$ and would also cause the offset crack to kink away from the centerline. This particular test of configurational stability requires *both* α and β be positive. This same test has been used in Section III.B.1.b for the double cantilever beam, and in Section V.C.2.a for substrate spalling driven by residual tension in the film.

Another insight is provided by the condition for stability of a straight, mode I crack path to small perturbations derived by Cotterell and Rice (1980). Their necessary condition for straight cracking is $T < 0$, where T is the second-order term in the crack tip expansion (2.1). Fleck *et al.* (1991) have solved for T for the crack problem of Fig. 74a. For the centerline crack ($c/h = 1/2$) under $K_{II}^\infty = 0$, they give

$$T = [(1 - \alpha)/(1 + \alpha)]T^\infty + \sigma_R + c_I(\alpha, \beta)K_I^\infty h^{-1/2}. \qquad (8.10)$$

Here, T^∞ is the T-stress for the homogeneous specimen in the absence of the layer, σ_R is the residual stress in the layer acting parallel to the centerline, and c_I is tabulated by Fleck *et al.* and presented here in Fig. 77. Residual compression parallel to the crack plane contributes to stability, as does a compliant mismatch of the layer relative to the rest of the specimen through the last term in (8.10). The last term in (8.10) is destablizing when the film is stiff. Note that the residual stress σ_R has no effect on the existence of a mode I path in the layer, just on its stability.

When there is significant elastic mismatch, the first term in (8.10) will usually be insignificant compared to the third term, since T^∞ is typically on the order of $K_I^\infty L^{-1/2}$, where L is a length characterizing an overall dimension of the specimen, which is assumed to be large compared to h. When this is the case, the T-stress at fracture is

$$T \cong \sigma_R + [(1 + \alpha)/(1 - \alpha)]^{1/2}c_I K_{Ic} h^{-1/2}, \qquad (8.11)$$

where, by (8.6), K_{Ic} is the intensity toughness of the layer material. The requirement $T < 0$ will always be met for a compliant layer supporting a compressive (or zero) residual stress. When the residual stress is tensile, the sign of T depends on which of the preceding terms is larger. Note that the
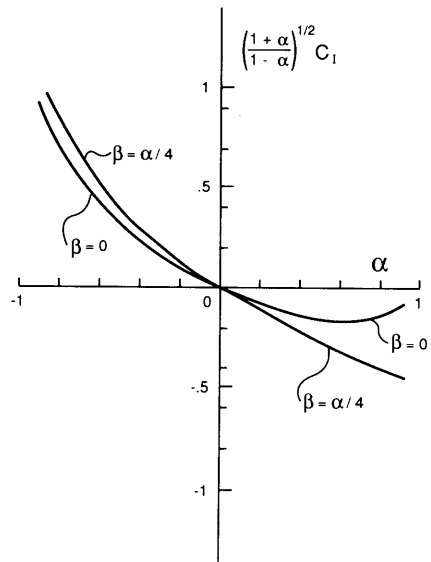
FIG. 77.   Coefficient c_I in (8.10).

second term in (8.11), which is always negative for a compliant layer, increases in magnitude as the layer thickness diminishes.

A number of examples of sandwich systems that have been reported to exhibit straight in-layer cracking are discussed by Fleck *et al.* (1991), and two of these will be remarked on in what follows. To emphasize the significance of this effect, one can point to the symmetrically loaded, double cantilever beam specimen, which is notoriously unstable in the absence of a layer due to the fact that $T^\infty > 0$. Because of the stabilizing influence of a thin compliant layer, the specimen can be used successfully to measure the toughness of a material in a sandwich layer.

D. INTERFACE OR IN-LAYER CRACKING?

Two sets of toughness data taken using sandwich specimens are shown in Fig. 78. Indicated for each data point is whether the crack propagated along the interface or within the interior of the layer. Thouless's (1990b) data, for a brittle wax layer joining silica glass, is presented as a function of the applied phase angle of loading ψ^∞. Only for $\psi^\infty = 0$ did the crack propagate within the brittle wax layer. The toughness of the wax was about one half
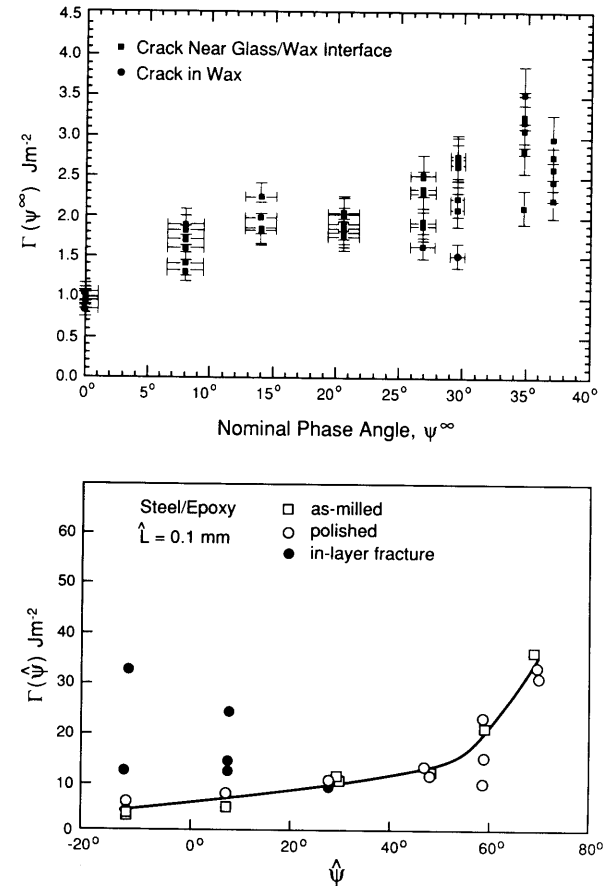
FIG. 78.   a) Data of Thouless (1990b) for brittle wax layer sandwiched between glass substrates. b) Data of Wang and Suo (1990) for an epoxy layer between steel substrates.

that of the interface for near-mode-1 fracture. The data of Wang and Suo (1990) for an epoxy adhesive layer joining two halves of a steel Brazil nut shows instances of in-layer propagation for $|\hat{\psi}|$-values as large as about 10°. Moreover, the epoxy is significantly tougher than the interface at low values of $\hat{\psi}$, and the in-layer path involves substantially higher energy dissipation and applied load than the interface path. Nevertheless, a number of specimens did exhibit in-layer propagation. This preference for a high energy path over a low energy path in close proximity highlights the importance of understanding the mechanics of crack path selection. It remains an open question as to why a path down the interface was not selected, especially

since Wang and Suo started their cracks on the interface and observed a small amount of interface crack growth prior to the crack kinking into the interior of the layer. Condition (2.65) for kinking out of the interface, including the influence of the η-contribution, does not appear to be satisfied. This is the feature of the behavior that remains to be explained.

Both sandwich systems in Fig. 78 have a highly compliant layer, and both systems have a tensile residual stress σ_R in the layer. But in each case the second term in (8.11) is at least twice as large in magnitude as σ_R (cf. Fleck et al., 1991, for complete details). Thus, the mode I specimens have a distinctly negative T-stress, and straight cracking within the layer is consistent with the stability theory. By contrast, the plexiglass/epoxy sandwich system of Fig. 9 has relatively small elastic mismatch and a positive T-stress under mode I loading. For this system, the crack always followed one of the two interfaces.

For values of $|\psi^\infty|$ outside the range of possible trapping of the crack within the layer (e.g., $|\psi^\infty|$ greater than $0°$ to $10°$, depending on the mismatch), the crack will be driven toward one interface or the other— toward the lower interface if $\psi^\infty > 0$ and toward the upper if $\psi^\infty < 0$. If material #1 is sufficiently tough to resist any attempts for the interface crack to kink into it, the crack will follow the interface and the test will generate the interface toughness according to (8.7). This is the case for both sets of test data presented in Fig. 78, other than those data points mentioned in the preceding. Various micro-morphologies of interface fracture have been observed, some of which have been discussed by Evans et al. (1989). If the interface toughness is low compared with that of both materials #1 and #2, then the crack will tend to follow the interface fairly cleanly. If, however, the interface toughness is comparable to that of the layer material, then the interface crack will interact with flaws in the layer adjacent to the interface, and nucleate microcracks. The effect of the mixed mode loading is to grow these microcracks back towards the interface. The resulting fracture surface will be covered with tiny chunks of the layer material. Additional discussion of the micro-morphology of interface fracture is given by Chai (1988), Wang and Suo (1990), and by several authors in the volume on metal–ceramic interfaces (Rühle et al., 1990).

E. Alternating Morphology (Fig. 74c)

In the alternating mode of cracking of Fig. 74c, the crack switches back and forth between interfaces with a fairly regular interval, which is typically

several times the layer thickness. The mode has been reported in matrix layers between plies of a composite when the loading is nominally mode I, and it has been fully documented for mode I loading of an aluminum/ epoxy/aluminum sandwich specimen by Chai (1987). Chai used a heat setting epoxy, which gives rise to a relatively high residual tensile stress in the layer ($\sigma_R \approx 60$ MPa), which is more than twice the magnitude of the second term in the T-stress in (8.11) (cf. Fleck et al., 1991). Thus, Chai's system has a strongly positive T-stress and is not expected to display straight cracking within the layer.

Akisanya and Fleck (1990) have carried out a quantitative analysis of the alternating mode of cracking with specific attention to the aluminum/ epoxy system. Central to the phenomenon is the variation in the proportion of mode 2 to mode 1 of the interface crack as it propagates from the point where it first joins the interface in any given cycle, i.e., at $c = 0$ in Fig. 79. The trends of the variation in ψ found by Akisanya and Fleck are sketched in Fig. 79, where ψ is defined by (2.45) with $l = h$. When $\sigma_R = 0$, ψ rapidly approaches the limiting value given by (3.38) with $K_{II} \equiv K_{II}^\infty = 0$, i.e., $\psi = \omega$. (For the aluminum/epoxy sandwich, $\alpha = 0.93$, $\beta = 0.22$, $\varepsilon = -0.07$ and $\omega \cong -15°$.) However, when $\sigma_R \sqrt{h}/K_I^\infty$ is on the order of unity,
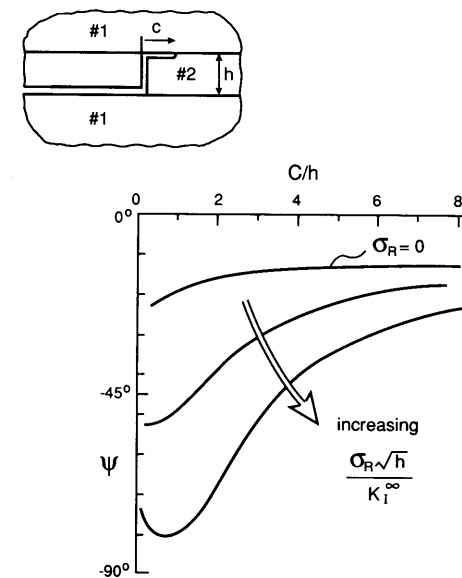

FIG. 79.   Sketch of trends of phase of loading at interface crack tip for various levels of residual tension σ_R in the layer. The remote loading is mode I.

which is the case for the Chai specimen, the interface crack starts with a large component of mode 2, which then diminishes to the value $\psi = \omega$ as c/h increases. The large negative mode 2 component forces the crack to remain in the interface, since it cannot penetrate the aluminum. Only when c/h has increased to the point where the magnitude of ψ is sufficiently low does kinking down into the layer become possible. With the aid of the kinking analysis of Section II.C.5, the value of c/h was determined at which a mode I kink crack is possible. For the aluminum/epoxy system of Chai, Akisanya and Fleck found that the kinking condition is met when c/h reaches a value of about 2, in agreement with the intervals observed by Chai.

F. Tunneling Cracks

An example illustrating the ability of a crack in a brittle adhesive layer to tunnel through the layer was given in Section III.A.1. If the layer material is sufficiently less tough that the interface and the adjoining material, cracking will be confined to the layer as depicted in Fig. 16. Steady-state tunneling results are useful because they provide fail-safe limits on stress levels (or on layer thicknesses) such that extensive cracking can be avoided. The particular example of Section III.A.1 reveals that an initial crack-like flaw whose greatest dimension is equal to the layer thickness (e.g., a penny-shaped crack) will initiate growth at a stress that is only about 10% higher than the steady-state tunneling stress. For many systems where the flaw size is on the order of the layer thickness, the tunneling results should provide realistic upper limits. When the flaw size is much smaller, the stress to initiate crack growth is much higher than that predicted by the steady-state tunneling limit, and the transient tunneling process is then highly unstable.

Several steady-state tunneling results for layers are presented in this section. The results and their potential applications have a close resemblance to the results for thin-film cracking in Section V.B.

1. *Isolated Tunneling Crack*

As previously emphasized, the energy released, hG_{ss}, per unit length of steady-state propagation of a tunneling crack is precisely the energy released by a plane strain crack extended across the layer. Calculations have been performed for G_{ss} by Ho and Suo (1990) for finite thickness sandwiches, as specified in the insert in Fig. 80. In Fig. 80, σ denotes the uniform tensile
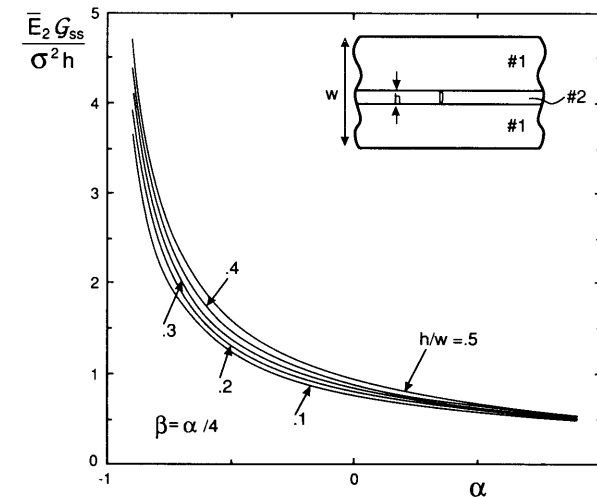
Fig. 80. Steady-state energy release rate for isolated tunneling crack. The crack extends from interface to interface, and is propagating in the direction perpendicular to the cross-section shown.

stress within the central layer prior to introduction of the crack. That stress may be due to a load applied to the sandwich or it may be a self-equilibrated residual stress. Curves of the nondimensional G_{ss} are shown as a function of the elastic mismatch parameter α with $\beta = \alpha/4$ for various values of layer thickness to total thickness, h/w. As long as the central layer is not too stiff compared to the adjoining layers, the results for $h/w = 0.1$ are close to the limiting case $h/w = 0$. For example, for $\alpha = 0$, the normalized G_{ss} is 0.788 for $h/w = 0.1$ and 0.785 for $h/w = 0$. Observe that a relatively compliant substrate (i.e., small E_1 and/or w/h) provides less constraint, inducing higher driving force. It is likely, for the same reason, that higher driving force will be induced by crack-induced plasticity in the substrates, by interface debonding, or by any other source of constraint loss. These effects have been noted in thin film channeling by Hu and Evans (1989).

2. *Multiple Tunneling Cracks*

The approach to multiple cracking pursued here is identical to that presented in Section V.B.3 for thin films under residual tension. The reader is referred to that section for a more complete discussion of the derivations underlying the results. Here, consideration will be limited to a layer of thickness h sandwiched between two infinitely thick blocks. Elastic mismatch
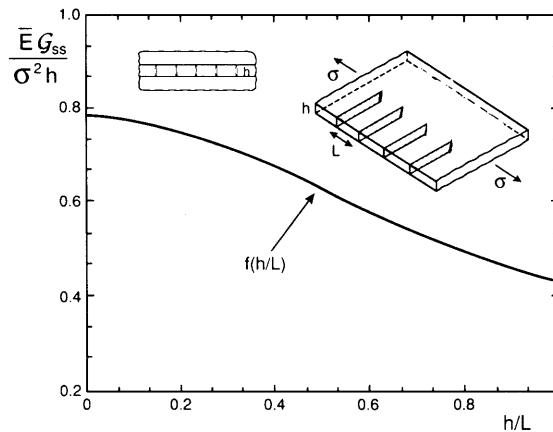
FIG. 81.   Steady-state tunneling cracks with uniform spacing, in the absence of elastic mismatch. The cracks extend from interface to interface.
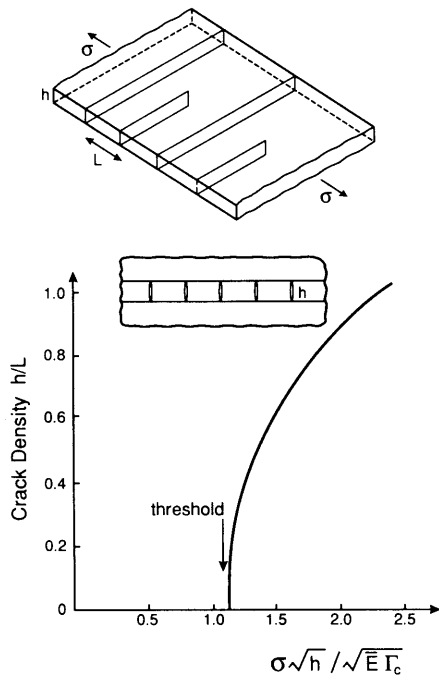

FIG. 82.   Relation between tunnel crack density and residual stress in the layer in the absence of elastic mismatch. The curve is obtained from (8.14) with $G_{ss} = \Gamma_c$.

between the layer and the adjoining blocks is neglected ($\alpha = \beta = 0$). The stress in the layer in the absence of the cracks is σ, which may be due to applied load or a residual stress.

First, consider an infinite set of cracks periodically spaced a distance L apart as in Fig. 81. If these cracks are equally extended in the tunneling direction,

$$\frac{\bar{E}G_{ss}}{\sigma^2 h} = f(h/L). \qquad (8.12)$$

The function $f(x)$, which can be evaluated using results from Tada *et al.* (1985), is plotted in Fig. 81. For $h/L \rightarrow 0$, $f = 0.785$ and (8.12) reduces to (3.1).

Next, consider the situation in Fig. 82 where one set of cracks spaced a distance $2L$ apart has already tunneled across the layer, and where a second set bisecting the first set is in the process of tunneling across the layer. The steady-state energy release rate for the cracks in the process of tunneling is

$$\frac{\bar{E}G_{ss}}{\sigma^2 h} = 2f(h/L) - f(\tfrac{1}{2}h/L). \qquad (8.13)$$

Imagine a process in which σ is monotonically increased, as in application of an overall load or stressing due to temperature change with thermal expansion mismatch. Under the assumption that new cracks will be nucleated half-way between cracks that have already formed and tunneled, the preceding equation gives the relation between σ and the crack spacing h/L. With G_{ss} identified with the mode I toughness of the layer material Γ_c, (8.13) provides the desired relationship, which is plotted in Fig. 82. The threshold corresponds to the lowest stress at which steady-state tunneling can occur, i.e., for $h/L \rightarrow 0$,

$$\sigma[h/(\bar{E}\Gamma_c)]^{1/2} = 1.128. \qquad (8.14)$$

The effect of elastic mismatch on this threshold level can be determined using the results for the isolated tunneling crack.

3. *Lateral Tunneling of a Kinked Crack*

Tunneling appears to be a prevalent mode of cracking in layered materials. When the brittle layer is thin and the flaw size is comparable to the layer thickness, the cracks can be readily nucleated. A variety of applications of these ideas can be found in Ho and Suo (1990) and Ye and Suo (1990). Here, we give one more example to show the versatility.

3D local kink crack   lateral spreading of kink
                           crack by tunneling
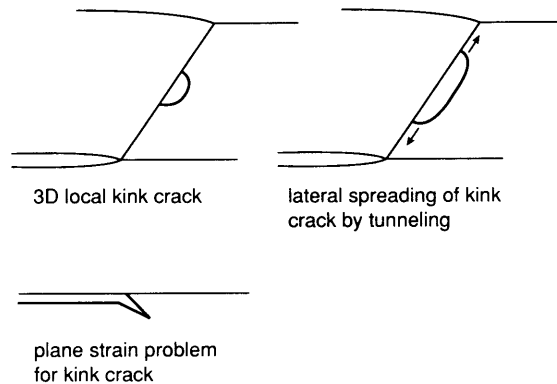
plane strain problem
for kink crack

FIG. 83.   Spread of a local kink by tunneling. Top left: 3-D local kink crack; top right: lateral spreading of kink crack by tunneling; bottom: plane strain problem for kink crack.

Because it has relevance to the ability of an interface crack to nucleate a kink into the adjoining layer, we mention in passing application of the tunneling concept to crack kinking. Suppose the parent interface crack depicted in Fig. 83 encounters a local, three-dimensional flaw that is capable of nucleating kinking. Consider the process in which the kinked segment of crack "tunnels" laterally along the interface crack front. Formally, this tunneling process can be treated as a steady-state process. The average energy release rate at the laterally spreading crack front can be evaluated using the energy released in the plane strain problem, just as in the previous examples. To simplify the discussion, assume $\beta = 0$ and $\eta = 0$, where η is given by (2.63). Since the energy release rate for the plane strain problem for a small kink is independent of kink crack length (*cf.* Section II.C.5), it follows that the average energy release rate for lateral tunneling along the interface crack front is *equal* to the plane strain energy release rate. Consequently, there is no barrier to the lateral spread of a locally nucleated kink. This observation may help to explain why crack kinking often appears to occur simultaneously along a more-or-less straight segment of crack front.

Acknowledgments

References

Akisanya, A. R., and Fleck, N. A. (1990). Analysis of a wavy crack in sandwich specimens. To be published in *Int. J. Fracture*.

Anderson, G. P., DeVries, K. L., and Williams, M. L. (1974). Mixed mode stress field effect in adhesive fracture. *Int. J. Fracture* **10**, 565–583.

Argon, A. S., Gupta, V., Landis, H. S., and Cornie, J. A. (1989). Intrinsic toughness of interfaces between SiC coatings and substrates of Si or C fibers. *J. Mater. Sci.* **24**, 1406–1412.

Atkinson, C., Smelser, R. E., and Sanchez J. (1982). Combined mode fracture via the cracked Brazilian disk test. *Int. J. Fracture*. **18**, 279–291.

Bao, G., Ho, S., Fan, B., and Suo, Z. (1990). The role of material orthotropy in fracture specimens for composites. *Int. J. Solids Structures* (in press).

Beuth, J. (1990). Cracking of thin bonded films in residual tension. To be published.

Beuth, J. (1991). Ph.D. thesis research in progress, Harvard University.

Cannon, R. M., Fisher, R., and Evans, A. G. (1986). Decohesion of thin films from ceramics. *In* Proc. Symp. on Thin Films—Interfaces and Phenomena, Boston, Mass. Mater. Res. Soc. 1986, pp. 799–804.

Cao, H. C., and Evans, A. G. (1989). An experimental study of the fracture resistance of bimaterial interface, *Mechanics of Materials* **7**, 295–305.

Chai, H. (1987). A note on crack trajectory in an elastic strip bounded by rigid substrates. *Int. J. Fracture* **32**, 211–213.

Chai, H. (1988). Shear fracture. *Int. J. Fracture* **37**, 137–159.

Chai, H. (1990). Three-dimensional fracture analysis of thin film debonding. *Int. J. Fracture*. **46**, 237–256.

Chai, H., Babcock, C. D., and Knauss, W. G. (1981). One dimensional modelling of failure in laminated plates by delamination buckling. *Int. J. Solids Structures* **17**, 1069–1083.

Charalambides, P. G., Cao, H. C., Lund, J., and Evans, A. G. (1990). Development of test method for measuring the mixed mode fracture resistance of bimaterial interfaces. *Mechanics of Materials* **8**, 269–283.

Charalambides, P. G., Lund, J., Evans, A. G., and McMeeking, R. M. (1989). A test specimen for determining the fracture resistance of bimaterial interfaces. *J. Appl. Mech.* **56**, 77–82.

Cherepanov, G. P. (1962). The stress state in a heterogeneous plate with slits (in Russian). *Izvestia AN SSSR, OTN, Mekhan. i Mashin* **1**, 131–137.

Cherepanov, G. P. (1979). "Mechanics of Brittle Materials." McGraw-Hill, New York.

Chiao, Y.-H., and Clarke, D. R. (1990). Residual stress induced fracture in glass–sapphire composites: Planar geometry. *Acta Met.* **38**, 251–258.

Comninou, M. (1977). The interface crack. *J. Appl. Mech.* **44**, 631–636.

Comninou, M., and Schmueser, D. (1979). The interface crack in a combined tension-compression and shear field. *J. Appl. Mech.* **46**, 345–348.

Cotterell, B., and Rice, J. R. (1980). Slightly curved or kinked cracks. *Int. J. Fract.* **16**, 155–169.

Delannay, F., and Warren, P. (1991). On crack interaction and crack density in strain-induced cracking of brittle films on ductile substrates. *Acta Metall. Mater.* **39**, 1061–1072.

Drory, M. D., Thouless, M. D., and Evans, A. G. (1988). On the decohesion of residually stressed thin films. *Acta Met.* **36**, 2019–2028.

Dugdale, D. (1960). Yielding of steel sheets containing slits. *J. Mech. Phys. Solids.* **8**, 100–108.

Dundurs, J. (1969). Edge-bonded dissimilar orthogonal elastic wedges. *J. Appl. Mech.* **36**, 650–652.

England, A. H. (1965). A crack between dissimilar media. *J. Appl. Mech.* **32**, 400–402.

Erdogan, F. (1965). Stress distribution in bonded dissimilar materials with cracks. *J. Appl. Mech.* **32**, 403–410.

Erdogan, F., and Arin, K. (1972). Penny-shaped interface crack between an elastic layer and a half space. *Int. J. Engng. Sci.* **10**, 115–125.

Evans, A. G., Dalgleish, B. J., He, M., and Hutchinson, J. W. (1989). On crack path selection and the interface fracture energy in bimaterial systems. *Acta Metall.* **37**, 3249–3254.

Evans, A. G., Drory, M. D., and Hu, M. S. (1988). The cracking and decohesion of thin films. *J. Mater. Res.* **3**, 1043–1049.

Evans A. G., and Hutchinson, J. W. (1984). On the mechanics of delamination and spalling in compressed films. *Int. J. Solids Structures* **20**, 455–466.

Evans, A. G., and Hutchinson, J. W. (1989). Effects of non-planarity on the mixed mode fracture resistance of bimaterial interfaces. *Acta Metall. Mater.* **37**, 909–916.

Evans, A. G., Rühle, M., Dalgleish, B. J., and Charalambides, P. G. (1990). The fracture energy of bimaterial interfaces. *Mater. Sci. Engng. A* **126**, 53–64.

Farris, R. J., and Bauer, C. L. (1988). A self-determination method of measuring the surface energy of adhesion of coatings. *J. Adhesion* **26**, 293–300.

Fleck, N. A., Hutchinson, J. W., and Suo, Z. (1991). Crack path selection in a brittle adhesive layer. *Int. J. Solids and Structures.* **27**, 1683–1703.

Friedrich, K., ed. (1989). "Application of Fracture Mechanics to Composite Materials." Elsevier, New York.

Gecit, M. R. (1979). Fracture of a surface layer bonded to a half space. *Int. J. Engng. Sci.* **17**, 287–295.

Gille, G. (1985). Strength of thin films and coatings. *In* "Current Topics in Materials Science." Vol. 12 (E. Kaldis, ed.), North-Holland, Chap. 7.

Hayashi, K. and Nemat-Nasser, S. (1981). Energy-release rate and crack kinking under combined loading. *J. Appl. Mech.* **48**, 520–524.

He, M.-Y., Bartlett, A., Evans, A. G., and Hutchinson, J. W. (1991). Kinking of a crack out of an interface: role of in-plane stress. *J. Am. Ceram. Soc.* **74**, 767–771.

He, M.-Y., and Evans, A. G. (1990a). Initial cracking of thin films. Manuscript in preparation.

He, M.-Y., and Evans, A. G. (1990b). Finite element analysis of beam specimens used to measure delamination resistance of composites. *J. Composites Tech. Res.* (in press).

He, M.-Y., and Hutchinson, J. W. (1989a). Kinking of crack out of an interface. *J. Appl. Mech.* **56**, 270–278.

He, M.-Y., and Hutchinson, J. W. (1989b). Kinking of a crack out of an interface: Tabulated solution coefficients. Available for a limited period from Marion Remillard, Pierce Hall 314, Division of Applied Sciences, Harvard University, Cambridge, Massachusetts 02138.

Ho, S., and Suo, Z. (1990). Tunneling cracks in constrained layers. Manuscript in preparation.

Hu, M. S., and Evans, A. G. (1989). The cracking and decohesion of thin films on ductile substrate. *Acta Met.* **37**, 917–925.

Hu, M. S., Thouless, M. D., and Evans, A. G. (1988). The decohesion of thin films from brittle substrates. *Acta Met.* **36**, 1301–1307.

Hutchinson, J. W. (1990). Mixed mode fracture mechanics of interfaces. *In* "Metal–Ceramic Interfaces," (M. Rühle, A. G. Evans, M. F. Ashby, and J. P. Hirth, eds.), Pergamon Press, New York, pp. 295–306.

Hutchinson, J. W., Mear, M. E., and Rice, J. R. (1987). Crack paralleling an interface between dissimilar materials. *J. Appl. Mech.* **54**, 828–832.

Jensen, H. M. (1990). Mixed mode fracture analysis of the blister test. *Engin. J. Fracture Mech.* (in press).

Jensen, H. M., Hutchinson, J. W., and Kim, K.-S. (1990). Decohesion of a cut prestressed film on a substrate. *Int. J. Solids Structures* **26**, 1099–1114.

Kamada, K., and Higashida, Y. (1979). A fracture model of radiation blistering. *J. Appl. Physics* **50**, 4131–4138.

Kinloch, A. J. (1987). "Adhesion and Adhesives," Chapman and Hall, London.

Lekhnitskii, S. G. (1981). "Theory of Elasticity of an Anisotropic Body," Mir Publishers, Moscow.

Liechti, K. M. (1985). Moire of crack-opening interferometry in adhesive fracture mechanics. *Experimental Mechanics* **25**, 255–261.

Liechti, K. M., and Chai, Y.-S. (1990a). Asymmetric shielding in interfacial fracture under inplane shear. *J. Appl. Mech*, in press.

Liechti, K. M., and Chai, Y.-S. (1990b). Biaxial loading experiments for determining interfacial toughness. *J. Appl. Mech*, in press.

Liechti, K. M. and Hanson, E. C. (1988). Nonlinear effects in mixed-mode interfacial delaminations. *Int. J. Fracture* **36**, 199–217.

Malyshev, B. M., and Salganik, R. L. (1965). The strength of adhesive joints using the theory of cracks. *Int. J. fracture. Mech.* **5**, 114–128.

O'Brien, T. K. (1984). Mixed-mode strain-energy-release rate effects on edge delamination of composites. *In* "Effects of Defects in Composite Materials," ASTM STP 836, American Society for Testing and Materials, pp. 125–142.

O'Dowd, N. P., Shih, C. F., and Stout, M. G. (1990). Test geometries for measuring interfacial toughness. Submitted for publication.

Reimanis, I. E., and Evans, A. G. (1990). The fracture resistance of a model metal/ceramic interface. *Acta Metall. Mater.* (in press).

Rice, J. R. (1968). A path independent integral and approximation analysis of strain concentration by notches and cracks. *J. Appl. Mech.* **35**, 379–386.

Rice, J. R. (1988). Elastic fracture concepts for interfacial cracks. *J. Appl. Mech.* **55**, 98–103.

Rice, J. R., and Sih, G. C. (1965). Plane problems of cracks in dissimilar media. *J. Appl. Mech.* **32**, 418–423.

Rice, J. R., Suo Z., and Wang, J.-S. (1990). Mechanics and thermodynamics of brittle interfacial failure in bimaterial systems. *In* "Metal–Ceramic Interfaces". (M. Rühle, A. G. Evans, M. F. Ashby, and J. P. Hirth, eds.), Pergamon Press, New York, pp. 269–294.

Rothschilds, R. J., Gillespie, J. W., and Carlsson, L. A. (1988). Instability-related delamination growth in thermoset and thermo-plastic composites. *In* "Composite Materials: Testing and Design," ASTM STP 972 (J. D. Whitcomb, ed.), pp. 161–179.

Rühle, M., Evans, A. G. Ashby, M. F., and Hirth, J. P., eds. (1990). "Metal–Ceramic Interfaces," Acta-Scripta Metallurgica Proc. Series 4, Pergamon Press, New York.

Sbaizero, O., Charalambides, P. G., and Evans, A. G. (1990). Delamination cracking in a laminated ceramic matrix composite. *J. Am. Ceram. Soc.* **73**, 1936–1940.

Shapery, R. A., and Davidson, B. D. (1990). Prediction of energy release rate for mixed-mode delamination using classical plate theory. *Appl. Mech. Rev.* **43**, S281–S287.

Shih, C. F., and Asaro, R. J. (1988). Elastic–plastic analysis of cracks on bimaterial interfaces: Part I. Small scale yielding. *J. Appl. Mech.* **55**, 299–316.

Sih, G. C., Paris, P. C., and Irwin, G. R. (1965). On cracks in rectilinearly anisotropic bodies. *Int. J. Fracture Mech.* **1**, 189–203.

Spearing, S. M., and Evans, A. G. (1990). The role of fiber bridging in the delamination resistance of fiber-reinforced composites. *Acta Metall. Mater.* (in press).

Storakers, B. (1988). Nonlinear aspects of delamination in structural members. *In* "Proc. XVIIth Int. Cong. Theor. Appl. Mech," (P. Germain, *et al.*, eds.), Grenoble, France, Elsevier, 315–336.

Suga, T., Elssner, E., and Schmander, S. (1988). Composite parameters and mechanical compatibility of material joints. *J. Composite Materials* **22**, 917–934.

Suo, Z. (1989). Singularities interacting with interfaces and cracks. *Int. J. Solids Structure* **25**, 1133–1142.

Suo, Z. (1990a). Singularities, interfaces and cracks in dissimilar anisotropic media. *Proc. R. Soc. Lond.* A **427**, 331–358.

Suo, Z. (1990b). Failure of brittle adhesive joints. *Appl. Mech. Rev.* **43**, S276–S279.

Suo, Z. (1990c). Delamination specimens for orthotropic materials, *J. Appl. Mech.* **57**, 627–634.

Suo, Z., Bao, G., and Fan, B. (1990a). Delamination *R*-curves phenomena due to damage. *J. Mech. Phys. Solids* (in press).

Suo, Z., Bao, G., Fan, B., and Wang, T. C. (1990b). Orthotropy rescaling and implications for fracture in composites. *Int. J. Solids and Structures*, in press.

Suo, Z., and Hutchinson, J. W. (1989a). On sandwich test specimen for measuring interface crack toughness. *Mater. Sci. Engng.* A **107**, 135–143.

Suo, Z., and Hutchinson, J. W. (1989b). Steady-state cracking in brittle substrate beneath adherent films. *Int. J. Solids Structure* **25**, 1337–1353.

Suo, Z., and Hutchinson, J. W. (1990). Interface crack between two elastic layers. *Int. J. Fracture* **43**, 1–18.

Tada, H., Paris, P. C., and Irwin, G. R. (1985). "The Stress Analysis of Cracks Handbook," Del Research, St. Louis, Missouri.

Thompson, J. M. T., and Hunt, G. W. (1973). "A General Theory of Elastic Stability," Wiley, New York.

Thouless, M. D. (1990a). Crack spacing in brittle films on elastic substrates. *J. Am. Ceram. Soc.* **73**, 2144–2146.

Thouless, M. D. (1990b). Fracture of a model interface under mixed-mode loading. *Acta Met.* **38**, 1135–1140.

Thouless, M. D., Cao, H. C., and Mataga, P. A. (1989). Delamination from surface cracks in composite materials. *J. Mater. Sci.* **24**, 1406–1412.

Thouless, M. D., Evans, A. G., Ashby, M. F., and Hutchinson, J. W. (1987). The edge cracking and spalling of brittle plates. *Acta Met.* **35**, 1333–1341.

Thouless, M. D., and Evans, A. G. (1990). Comment on the spalling and edge-cracking of plates. *Scripta Met. and Mater.* **24**, 1507–1510.

Trantina, G. C. (1972). Combined mode crack extension in adhesive joints. *J. Composite Materials* **6**, 271–285.

Wang, J. S., and Suo, Z. (1990). Experimental determination of interfacial toughness using Brazil-nut-sandwich. *Aca Met.* **38**, 1279–1290.

Wang, S. S., Mandell, J. F., and McGarry, F. J. (1978). An analysis of the crack tip stress field in DCB adhesive fracture specimens. *Int. J. Fracture* **14**, 39–58.

Wang, T. C., Shih, C. F., and Suo, Z. (1990). Crack extension and kinking in laminates and bicrystals. *Int. J. Solids Structures* (in press).

Whitcomb, J. D. (1986). Parametric analytical study of instability-related delamination growth. *Compos. Sci. Technol.* **25**, 19–48.

Williams, J. G. (1988). On the calculation of energy release rates for cracked laminates. *Int. J. Fracture* **36**, 101–119.

Williams, M. L. (1959). The stress around a fault or crack in dissimilar media. *Bull. Seismol. Soc. Am.* **49**, 199–204.

Ye, T., Suo, Z., and Evans, A. G. (1990). Thin film cracking and the roles of substrate and interface. Submitted for publication.

Yin, W.-L. (1985). Axisymmetric buckling and growth of a circular delamination in a compressed laminate. *Int. J. Solids Structures* **21**, 503–514.

Zak, A. R., and Williams, M. L. (1963). Crack point singularities at a bi-material interface. *J. Appl. Mech.* **30**, 142–143.

Zdaniewski, W. A., Conway, J. C., and Kirchner, H. P. (1987). Effect of joint thickness and residual stress on the properties of ceramic adhesive joints: II. Experimental results. *J. Am. Ceram. Soc.* **70**, 104–109.

Whitcomb, J. D. (1986). Parametric analytical study of instability-related delamination growth. *Compos. Sci. Technol.* **25,** 19–48.

Williams, J. G. (1988). On the calculation of energy release rates for cracked laminates. *Int. J. Fracture* **36,** 101–119.

Williams, M. L. (1959). The stress around a fault or crack in dissimilar media. *Bull. Seismol. Soc. Am.* **49,** 199–204.

Ye, T., Suo, Z., and Evans, A. G. (1990). Thin film cracking and the roles of substrate and interface. Submitted for publication.

Yin, W.-L. (1985). Axisymmetric buckling and growth of a circular delamination in a compressed laminate. *Int. J. Solids Structures* **21,** 503–514.

Zak, A. R., and Williams, M. L. (1963). Crack point singularities at a bi-material interface. *J. Appl. Mech.* **30,** 142–143.

Zdaniewski, W. A., Conway, J. C., and Kirchner, H. P. (1987). Effect of joint thickness and residual stress on the properties of ceramic adhesive joints: II. Experimental results. *J. Am. Ceram. Soc.* **70,** 104–109.